

Novel Multiscale Modeling Schemes for Damage Evolution in Composite Laminates

Thesis submitted in partial fulfillment of the requirements
for the degree of Doctor of Philosophy

of the
Indian Institute of Technology, Bombay, India
and
Monash University, Australia

by

Mr. Ganesh Soni

Supervisors:

Supervisor-1 Prof. Ramesh Singh (IIT Bombay)

Supervisor-2 Prof. Mira Mitra (IIT Bombay)

Supervisor-1 Prof. Wenyi Yan (Monash University)

Supervisor-2 Prof. Brian Falzon (External)



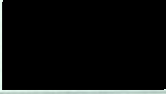
*The course of study for this award was developed jointly by
the Indian Institute of Technology, Bombay and Monash University, Australia
and given academic recognition by each of them.*

The programme was administered by The IITB-Monash Research Academy

(5/12/2014)

Approval sheet

The thesis entitled 'Novel Multiscale Modeling Schemes for Damage Evolution in Composite Laminates' submitted by **Ganesh Soni** is approved for the degree of **Doctor of Philosophy**.



(Prof. Ramesh Singh)
IITB Supervisor



(Prof. Mira Mitra)
IITB Co-supervisor



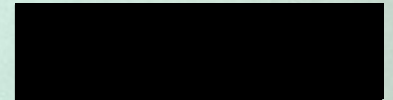
(Prof. Wenyi Yan)
Monash Supervisor



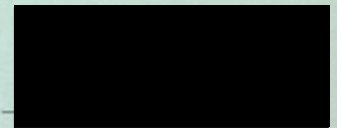
(Prof. Brian Falzon)
External Supervisor



(Prof. Salil Kulkarni)
Internal Examiner



(Prof. S. Gopalkrishnan)
External Examiner



(Prof. K. Narasimhan)
Chairman

Date : 5/12/2014

Place : IIT Bombay

Declaration

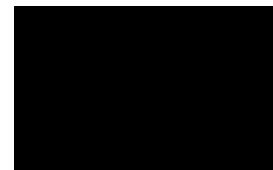
I declare that this written submission represents my ideas in my own words and where others' ideas or words have been included, I have adequately cited and referenced the original sources. I also declare that I have adhered to all principles of academic honesty and integrity and have not misrepresented or fabricated or falsified any idea/data/fact/source in my submission. I understand that any violation of the above will be cause for disciplinary action by the Institute and can also evoke penal action from the sources which have thus not been properly cited or from whom proper permission has not been taken when needed.

Notice 1

Under the Copyright Act 1968, this thesis must be used under the normal conditions of scholarly fair dealing. In particular no results or conclusions should be extracted from it, nor should it be copied or closely paraphrased in whole or in part without the written consent of the author. Proper written acknowledgement should be made for any assistance obtained from this thesis.

Notice 2

I certify that I have made all reasonable efforts to secure copyright permissions for third-party content included in this thesis and have not knowingly added copyright content to my work without the owner's permission.



Ganesh S. Soni

Date:

Place: IIT Bombay

Acknowledgement

It would be not possible to write this doctoral thesis without the help and support of the kind people around me; to only some of them it is possible to give particular mention here.

Sincere thanks to my guides Prof. Ramesh Singh, Prof. Mira Mitra, Prof. Wenyi Yan and Prof. Brian Falzon for their invaluable support and guidance throughout my project. Without their help and support, this project and the report would not have taken the present shape. They had played multiple roles throughout completion of this thesis-as a teacher, a researcher, a guide, a critic and a supportive friend.

I am grateful to my research progress committee members, Prof. Salil Kulkarni, and Prof. R.P.Shimpi for their valuable comments and suggestions. I would also like to thank Prof. S. Gopalkrishan (IISC Bangalore), Prof. Chiara Bisagni (University of California, San Diego) and Prof. H.S.N. Moorthy (IIT Chennai) for reviewing this thesis.

I also recognize the support and help from my colleagues, Dr. Vivek Bajpai, Dr. Nilesh Rayker, Dr. Niraj Dayama, Mr. Saurabh Gupta, Dr. Ganesh Dongre, Dr. Deepak Marla, Dr. Sachin Mastud, and Mr. Santanu Paul for their constant support. I am thanking to Mr. KNV Nair and Sandip for their great help in the machine shop. I would like to thank Mr. Shani Jadhav and Mr. K.T. Benny from materials testing lab for their help in testing of composite material. I would also like to thank Mr. Riyaz Ahmed Shaikh and Mrs. Priya Bansode from BTRA for their help in glass fibers testing.

Finally, I would like to acknowledge my family members and friends who supported me during my time here. First and foremost I would like to thank father Shri Shiniwas Soni, mother Shrimati Kamala Soni, younger brother Govind for their constant love and support. I would like to thank my aunty Shrimati Neelima Kalantri and my uncle Shri Arun Kalantri for their support throughout the endeavor. I would like to extend special thanks to my wife Sneha for her constant support, encouragement, quiet patience during this work. I would like to thank my friends Rahul Ade, Pratham, Prashant, Sushrut, Yogita Ahuja, Neha, Dr. Monoj Soni, Dr. Diploy Datta and Dipesh Patle for their constant support during the entire work.

Ganesh S. Soni

(Roll No. 09410407)

Abstract

Microscale damage mechanism of the multi-layer composite laminates is one of the active areas of research. Micromechanics theory is extensively used for the prediction of elastic response and to perform damage analysis of unidirectional laminae via representative volume element (RVE). The present state of the art in the micromechanics theory is extended in this study for the damage analysis of the multi-fiber multi-layer laminates to capture the local damage mechanisms which include matrix failure, fiber-matrix debonding, fiber failure, and delamination. A multi-fiber multi-layer representative volume element (M^2RVE) representing a multi-layer cross-ply laminate is developed. Each layer in the M^2RVE is represented by a unit cube with multiple randomly distributed fibers of same diameter at specified angle ensuring specified volume fiber fraction. Periodic boundary conditions are applied to the all six M^2RVE surfaces to model the directional periodicity. All the simulations are performed by using FE analysis code ABAQUS[®]. A maximum principal stress criterion is used for modeling fiber failure. Mohr-coulomb failure criterion is used for matrix failure and standard traction-separation law is used for fiber-matrix debonding and for modeling delamination between plies. Numerical results from the FE analysis are found to be in good agreement with the experimental data obtained. Note that this technique is valid for periodic structures.

The periodic boundary condition is not a suitable assumption, especially in the regions of high gradients like free edges, interfaces, material discontinuities. The periodicity of simple unit cells is also unrealistic for non-uniform microstructures, due the presence of randomness, clustering or evolving micro-structural behavior. Consequently, this approach has limited utility in identifying local damage in real structural members. To address the limitations of the M^2RVE , a micro-macro multiscale scale multilevel model is proposed. The multilevel model is comprised of two levels, namely, microscale, and macroscale. The micro-macro model is an effective and computationally efficient technique for modeling the deformation and local damage in real composite structures.

Keywords: Multiscale modeling, Multi-layer multi-fiber representative volume element (M^2RVE), Damage mechanism, Micro-macro method

Table of Contents

Chapter 1: Introduction	1
1.1 Micro-mechanical modeling.....	1
1.2 Problem definition.....	4
1.3 Aim of the present work.....	5
1.4 Organization of thesis.....	6
Chapter 2: Literature Review	7
2.1 Introduction.....	7
2.2 RVE based multiscale modeling for damage prediction in periodic media.....	8
2.2.1 Representative volume element (RVE).....	10
2.2.2 Implementation of RVE for damage prediction.....	13
2.2.3 Multi-layer representative volume element.....	26
2.3 Multilevel methods for non-periodic media.....	30
2.4 Summary.....	34
Chapter 3: Damage analysis in in-plane shear via multi-fiber multi-layer representative volume element (M²RVE)	35
3.1 Introduction.....	35
3.2 Finite element modeling of M ² RVE for cross-ply laminate.....	36
3.2.1 Generation of the geometrical and FE model.....	36
3.2.2 Boundary and loading conditions.....	38
3.2.3 Material Properties.....	40
3.2.4 Failure criteria.....	40
3.3 Sensitivity analysis for the size of M ² RVE.....	43
3.4 Model validation.....	45
3.4.1 Experimental work.....	45
3.4.2 Experimental Results.....	46
3.4.3 Failure mode of the V-notch shear specimens.....	49
3.4.4 Global stress-strain response.....	50
3.5 Results and Discussion.....	52
3.5.1 Stress and strain evolution at microscale.....	52

3.5.2	Effect of fiber orientation on micro stress evolution.....	53
3.5.3	Effect of Mohr-Coulomb matrix friction angle on stress-strain response	54
3.5.4	Effect of interface strength on global stress-strain response	56
3.5.5	Effect of fiber orientation on debonding initiation and progression between the fiber and the matrix.....	58
3.5.6	Effect of fiber orientation on evolution of interface damage area	60
3.5.7	Shear stress-slip behaviour at the interface	62
3.6	Summary.....	63
Chapter 4: Comprehensive damage analysis for complex multi-axial loading via M²RVE.....		65
4.1	Introduction.....	65
4.2	Finite element modeling of M ² RVE	65
4.2.1	Generation of the geometrical and FE model.....	65
4.2.2	Boundary conditions.....	66
4.2.3	Loading conditions	67
4.2.4	Material Properties	68
4.3	Failure criteria	68
4.3.1	Fiber failure.....	69
4.3.2	Matrix failure	72
4.3.3	Fiber-matrix interface failure	72
4.3.4	Delamination between plies failure	72
4.4	Model validation.....	73
4.4.1	Specimen manufacture for experiments.....	74
4.4.2	Experimental Results.....	74
4.4.3	Global stress-strain response.....	74
4.5	Study of damage evolution mechanisms	76
4.5.1	Tensile failure dominated damage mechanism.....	76
4.5.2	Matrix and interface dominated failure mechanism.....	79
4.5.3	Interfacial and interlaminardecohesion driven failure mechanism	80
4.5.4	Combined failure driven by fiber damage, fiber-matrix debonding and interlaminardecohesion.....	83
4.6	Summary.....	88
Chapter 5: Micro-macro approach for damage prediction in non-periodic structures.....		89
5.1	Introduction.....	89
5.2	Formulation of the micro-macro approach based on the locality principle	90

5.3	Finite element modeling.....	94
5.3.1	Model geometry	94
5.3.2	Material and damage models.....	96
5.3.3	Boundary and contact conditions.....	97
5.4	Mesh sensitivity analysis.....	98
5.5	Model validation.....	100
5.6	Effect of the phase and interface properties of the micro-domain	101
5.6.1	Effect of interface fracture energy	101
5.6.2	Effect of matrix friction angle	104
5.7	Application of micro-macro analysis for characterization of stress raisers	105
5.7.1	Evolution of stresses and strains in microdomain.....	107
5.7.2	Damage evolution at the microdomain	108
5.8	Summary.....	110
Chapter 6: Conclusions and future scope		111
6.1	Key conclusions	111
6.1.1	Damage analysis in in-plane shear via multi-fiber multi-layer representative volume element (M ² RVE)	111
6.1.2	Comprehensive damage analysis for complex multi-axial loading via M ² RVE	112
6.1.3	Micro-macro approach for damage prediction in non-periodic structures	112
6.2	Contributions.....	113
6.3	Future scope	113
Appendix-I.....		114
Appendix-II		117
Appendix-III.....		119
References.....		120
Publications		128
	Journal publication.....	128
	Conference proceedings	128

List of Tables

Table 3.1 Elastic properties of matrix and fibers.....	40
Table3.2 Effect of edge of the cube on normal stresses.....	45
Table 5.1 Elastic properties of the lamina.....	96

List of Figures

Figure 1.1 Damage mechanisms in composite laminates.....	2
Figure 1.2 Schematic diagram of M^2 RVE for cross-ply [0/90] laminate	3
Figure 1.3 Local damage in composite	3
Figure 1.4 Schematic of representative problem using macro-micro approach.....	5
Figure 2.1 Flow chart of literature survey.....	7
Figure 2.2 General methodology used in multiscale modeling of composite laminates	9
Figure 2.3 Typical representative volume element (RVE).....	10
Figure 2.4 The size requirement of a representative volume element.....	11
Figure 2.5 Homogenized material properties vs volume fractions of inclusions: (a) in two-norm of homogenized elasticity matrix; (b) in homogenized shear modulus G_{12} (Teradaa, 2000)	12
Figure 2.6 FE model of RVE; (a) Square array, (b) Hexagonal array, (c) Diamond array (Jones, 1999)	12
Figure 2.7 Fiber distribution and finite element discretization of a representative volume element of the composite (Gonzalez and Llorca, 2007).....	13
Figure 2.8 Contour plot of the accumulated plastic strain in the matrix in the composite with low interfacial strength (a) = 1.7% corresponding to the maximum strength. (b) = 4% (Gonzalez and Llorca., 2007).....	14
Figure 2.9 (a) Schematic of the simulation strategy to model the in-plane shear behavior of the cross-ply composite through the combination of loading parallel and perpendicular to the fibers. (b) Representative volume element of the lamina microstructure (Totry et al., 2009).....	16
Figure 2.10 (a) Contour plot of the accumulated plastic strain in the matrix for the lamina deformed under in-plane shear perpendicular to the fibers. (b) Contour plot of the shear stress, τ_{12} for the lamina deformed under in-plane shear perpendicular to the fibers. The far-field applied shear strain was $\tau_{12}=4\%$ (Totry et al. 2009).....	17
Figure 2.11 Schematic of the representative volume element of the lamina microstructure subjected to transverse compression and longitudinal shear (Totry et al., 2008).....	18
Figure 2.12 Failure locus under transverse compression and longitudinal shear (Totry et al., 2008).....	19
Figure 2.13 (a) The bidirectional fibers at cross angles embedded in matrix, (b) the cross-sectional view of a unit cell, (c) the periodic 3-D unit cell volume, and (d) the FEM discretized of the RUC (Abolfathi et al., 2008).....	20
Figure 2.14 Constituents and final assembly of FE model of 1 RC (Ng el al.2010).....	22
Figure 2.15 Formation of matrix shear cracks between adjacent fibers (b) Indirect loading of fibers in case of [45] composite (Ng el al., 2010).....	23
Figure 2.16 Multi-fiber FE model with one damageable layer in ever fiber: (a) cell model, (b) fibers in the model with removed damageable layers (Wang et al., 2011)	23
Figure 2.17 Schematic of FE ² method (Feyel et al., 2000)	24
Figure 2.18 Schematic of multi-level method (Ghosh et al., 1995).....	25
Figure 2.19 Multi-layer representative volume element (Ellyin et al., 2003).....	27
Figure 2.20 A representative volume element for an [\pm 45] angle-ply laminate (Xia et al., 2003).....	27

Figure 2.21 Comparison of results predicted by classic laminate theory and numerical simulations (Xia et al., 2003)	28
Figure 2.22 Representative volume element for $[0/90_3/0]_T$ laminate (Xia et al., 2000)	29
Figure 2.23 Multi-fiber multi-layer unit cell with orderly arranged fibers (Matsuda et al., 2007)	29
Figure 2.24 Schematic of macro-micro analysis (Wang and Yan, 2001)	31
Figure 2.25 (a) A body of homogenized UD composite under load; (b) isolated critical element; (c) critical element with microstructure restored; (d) the isolated interior element (Wang and Yan, 2004)	32
Figure 2.26 Macro domain FE mesh connected to the micro domain mesh by Lagrangian multiplier λ (Markovic and Ibrahimbegovic, 2004)	33
Figure 2.27 (a) Embedded cell approach(Gonzalez and Llorca, 2006) (b) Partial homogenization (Borokov and Sabadash, 2002)	33
Figure 3.1 Typical RVE and M^2RVE	35
Figure 3.2 M^2RVE for $[0/90]_n$ laminate	36
Figure 3.3 Schematic of the M^2RVE of the $[0/90]_n$ and $[\pm 45]_n$ laminate microstructure subjected to the in-plane shear loading	37
Figure 3.4 (a) Schematic of the meshed M^2RVE used for implementation of periodic boundary conditions.(b) In-plane shear loading using M^2RVE	38
Figure 3.5 Schematic representation of the failure criterion used for matrix and fiber-matrix debonding	41
Figure 3.6 Standard traction-separation law	42
Figure 3.7 In-plane shear stress strain response for various thicknesses of the cubes in M^2RVE (a) Interfacial strength = 30 MPa; (b) Interfacial strength = 10 MPa	44
Figure 3.8 Specimen dimensions for the V-notched rail shear tests	46
Figure 3.9 V-notched rail shear test fixture in action	47
Figure 3.10 Fixture for V-notched rail shear test (ASTM 7078)	47
Figure 3.11 In-plane shear properties of cross-ply, $[0/90]$, laminate: (a) Load-displacement diagram, (b) τ_{12} versus ϵ_{+45} and ϵ_{-45} of the test specimen	48
Figure 3.12 In-plane shear properties of angle-ply, $[\pm 45]$, laminate: (a) Load-displacement diagram from the testing machine, (b) τ_{12} versus ϵ_{+45} and ϵ_{-45} of the test specimen	48
Figure 3.13 (a) Cross-ply, $[0/90]$ and (b) angle-ply, $[\pm 45]$ specimens at the end of the test	49
Figure 3.14 In-plane shear stress-strain experimental response for cross-ply, $[0/90]$ and angle-ply, $[\pm 45]$, laminate (Appendix-I)	50
Figure 3.15 In-plane shear stress-strain response of M^2RVE for the $[0/90]_n$ laminate with perfect and imperfect bonding between matrix and fiber	51
Figure 3.16 In-plane shear stress-strain response of M^2RVE for the $[\pm 45]_n$ laminate with perfect and imperfect bonding between matrix and fiber	52
Figure 3.17 (a) Contour plot of the in-plane shear stress in M^2RVE with cohesive strength equal to 30 MPa,(b) Contour plot of the in-plane shear strain in M^2RVE with cohesive strength equal to 30 MPa	53

Figure 3.18 (a) Contour plot of the in-plane shear stress developed in matrix material with one layer multi-fiber RVE	
(b) Contour plot of the in-plane shear stress in matrix material using M^2RVE	54
Figure 3.19 In-plane shear stress-strain response of M^2RVE for $[0/90]_n$ laminate with different matrix friction angle	
.....	55
Figure 3.20 In-plane shear stress-strain response of M^2RVE for $[\pm 45]_n$ laminate with different matrix friction angle	
.....	56
Figure 3.21 In-plane shear stress-strain response of M^2RVE for $[0/90]_n$ laminate with different bonding strength between fibers and matrix.....	57
Figure 3.22 In-plane shear stress-strain response of M^2RVE for $[\pm 45]_n$ laminate with different bonding strength between fibers and matrix.....	58
Figure 3.23 Fiber-matrix debonding in $[0/90]_n$ laminate (a) Debonding initiation (b) Debonding propagation at the end of the step.....	59
Figure 3.24 Fiber-matrix debonding in $[\pm 45]_n$ laminate (a) Debonding initiation (b) Debonding propagation at the end of the step.....	60
Figure 3.25 In-plane shear strain versus percentage of damage fiber-matrix interface for $[0/90]_n$ laminate.....	61
Figure 3.26 In-plane shear strain versus percentage of damage fiber-matrix interface for $[\pm 45]_n$ laminate.....	61
Figure 3.27 Shear stress at the interface versus slip at the interface for $[0/90]_n$ laminate.....	62
Figure 3.28 Shear stress at the interface versus slip at the interface for $[\pm 45]_n$ laminate.....	63
Figure 4.1 Results with C3D4 and C3D10M element type.....	66
Figure 4.2 (a) In-plane tensile loading (b) In-plane shear loading (c) Out-of-plane shear loading (d) Combined in-plane tensile and out-of-plane shear loading.....	67
Figure 4.3 Schematic representation of the failure criterion used for matrix and fiber-matrix debonding.....	68
Figure 4.4 Typical experimental results of a classical load-displacement curve of glass fiber.....	69
Figure 4.5 WPP for tensile strength of the glass fibers.....	71
Figure 4.6 Weibull plot (Appendix-II).....	71
Figure 4.7 Specimen dimensions in-plane tensile loading tests.....	74
Figure 4.8 In-plane tensile stress-strain response of M^2RVE for $[0/90]_n$ laminate.....	75
Figure 4.9 Maximum principal stress in the E-glass fibers (a) Just before fiber failure (b) After fiber failure.....	76
Figure 4.10 Effect of matrix friction angle on the stress-strain response of M^2RVE for $[0/90]_n$ laminate subjected to in-plane tensile loading.....	77
Figure 4.11 Effect of fiber-matrix interfacial properties on the stress-strain response of M^2RVE for $[0/90]_n$ laminate subjected to in-plane tensile loading.....	78
Figure 4.12 Effect of delamination layer properties on the stress-strain response of M^2RVE for $[0/90]_n$ laminate subjected to in-plane tensile loading.....	79
Figure 4.13 Effect of fiber-matrix interfacial properties on the stress-strain response of M^2RVE for $[0/90]_n$ laminate subjected to out-of-plane shear loading.....	81

Figure 4.14 Effect of delamination layer properties on the stress-strain response of M^2RVE for $[0/90]_n$ laminate subjected to out-of-plane shear loading	82
Figure 4.15 QUADSCRT for delamination layer strength (a) 90MPa (b) 5 MPa at 1.5% out-of-plane shear strain .	82
Figure 4.16 SDEG for delamination layer strength of 5 MPa at 1.5% out-of-plane shear strain (a) just before failure (b) after failure	83
Figure 4.17 Maximum principal stress in the E-glass fibers at 0.6% of in-plane tensile strain and at 1.5% out-of-plane shear strain (a) before fiber failure (b) after fiber failure	84
Figure 4.18 Effect of matrix friction angle on the stress-strain response of M^2RVE for $[0/90]_n$ laminate subjected to in-plane tensile loading and out-of-plane shear loading	85
Figure 4.19 Effect of fiber-matrix interfacial properties on the stress-strain response of M^2RVE for $[0/90]_n$ laminate subjected to in-plane tensile loading and out-of-plane shear loading	85
Figure 4.20 Effect of delamination layer properties on the stress-strain response of M^2RVE for $[0/90]_n$ laminate subjected to out-of-plane shear loading	86
Figure 4.21 QUADSCRT for delamination layer strength (a) 60MPa (b) 5 MPa at 1.5% out-of-plane shear strain .	87
Figure 4.22 SDEG for delamination layer strength of 5 MPa at 0.2% out-of-plane shear strain (a) just before failure (b) after failure	87
Figure 5.1 Multi-level and multiscale methods in literature.....	89
Figure 5.2 Geometry of the (a) lamina with complete microstructure (b) partially homogenized lamina with the applied shear loading(c) meshing of the partially homogenized lamina	91
Figure 5.3 Comparison between full scale microstructural response and response predicted by micro-macro scheme and sub-modeling method.....	92
Figure 5.4 Proposed micro-macro approach	93
Figure 5.5 (a) Specimen geometry (b) model geometry	95
Figure 5.6 Geometry of the microstructural domain.....	95
Figure 5.7 Geometry of the unified specimen and microstructure.....	96
Figure 5.8 Boundary conditions on the finite element model for in-plane shear.....	97
Figure 5.9 Mesh seeds in the microstructure.....	99
Figure 5.10 Mesh convergence achieved by varying the number of mesh seeds	99
Figure 5.11 Comparison between experimental response and response predicted by micro-macro scheme.....	101
Figure 5.12 Effect of changing fracture energy of the fiber-matrix interface on shear stress-strain response.....	103
Figure 5.13 Contour plots of interfacial damage for fracture energies (a) 10 J/m ² (b) 100 J/m ² at 8% strain	103
Figure 5.14 Effect of changing matrix friction angle on shear stress-strain response.....	104
Figure 5.15 Von-Mises stress (MPa) distribution in a continuum model showing the regions of interest, i.e., regions near and away from the notch	105
Figure 5.16 Volume averaged shear stress as a function of applied shear load.....	106
Figure 5.17 Contour plot of Von Mises stress (MPa) in the matrix of cross-ply laminate at (a) notch (b) away from the notch at a 90 N load.....	107

Figure 5.18 Contour plot of accumulated plastic strain in the matrix of cross-ply laminate at (a) notch (b) away from the notch at a 90 N load..... 108

Figure 5.19 Comparison of evolution of the percentage of matrix elements damaged in the microstructure between the notch and away from it..... 109

Figure 5.20 Contour plot of damage of the fiber-matrix interface (a) notch (b) away from the notch at a 90 N load (the value 1 indicates total failure of the interface). 109

Chapter 1: Introduction

1.1 Micro-mechanical modeling

The Composite materials have opened up unique opportunities in structural design. Composites have very high strength-to-weight and stiffness-to-weight ratios which could potentially replace the conventional metallic materials in a host of applications. The key factor in utilizing the strength and uniqueness of laminated composite plates is the proper understanding of its structural response under different work load conditions. An in-depth understanding of their structural behavior can help us to explore this versatility to the maximum possible extent. It is important to accurately predict the mechanical behavior of fiber reinforced plastic (FRP) composite laminates for their efficient and reliable use in the structural applications. It is very important to develop in-depth understanding about the global and local damage response of the composites for reliable design of composite structures.

Mechanical properties of the laminated composites are easily obtained by using macro-mechanical models. These material models are usually phenomenological in nature and rely on a number of parameters obtained by performing standard experiments. The damage variables are calibrated with the experimental results, restricting the range of their applications for typical loading and boundary conditions. Different failure mechanisms like matrix failure, fiber fracture, fiber matrix debonding and delamination as shown in Fig. 1.1 takes place at different scales during the damage process. The fracture pattern obtained is relatively complex, even for simple loading conditions. Therefore, it is important to study the local damage initiation and evolution at different sites in the composite laminate for better physical understanding of the damage initiation and growth at the fiber and matrix level. Finite element (FE) based on micro-mechanics can accurately predict the mechanical response of a composite at the microscale (Sun and Vaidya, 1996). It utilizes a finite element (FE) based representative volume element (RVE) model for predicting the local as well as the global behavior of a composite lamina. These methods can effectively predict local and global damage response with the help of suitable failure criterion for each constituent as well as for the fiber-matrix interface. Considerable amount of research has been carried out in predicting damage response of the composite by using FE based periodic homogenization technique (Kanouté, 2009).

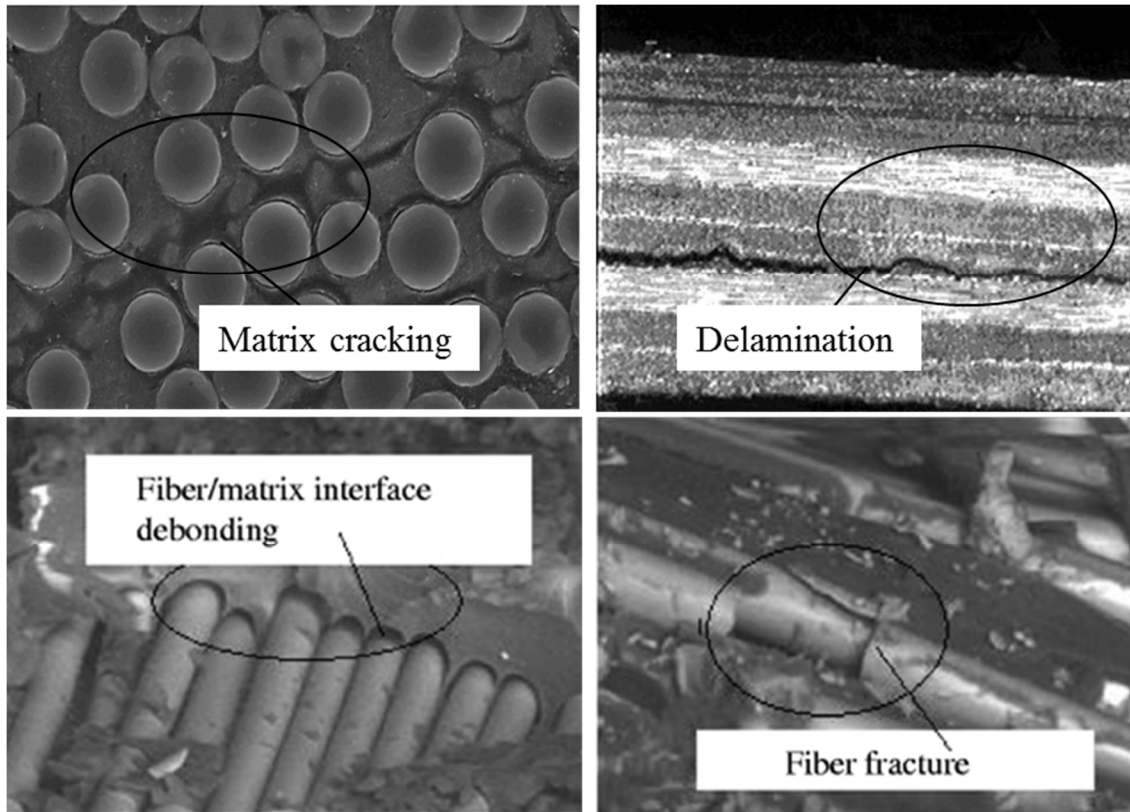


Figure 1.1 Damage mechanisms in composite laminates

At present, application of micro-mechanics via RVE based model is limited to the unidirectional lamina. The results obtained for unidirectional lamina are used to predict the properties of the lamina at an angle by using laminate theories. Numerical model for the laminate is then assembled using these effective properties of different plies. A detailed micro-mechanical model involving multiple fibers and multiple layers representing composite laminates has not been developed. There is huge potential to utilize micro-mechanics for the study of multidirectional laminate involving different failure mechanisms evolving at different sites at same time. Multiple fibers will ensure that the model is closed to the reality. There is no comprehensive model available in the literature, for predicting fiber failure, matrix damage, and interface failure all at the same time. Delamination between the plies has not been studied with the help of micro-mechanics. Therefore, the proposed work is expected to developed FE based M^2 RVE model, which can predict all the damage mechanisms including delamination.

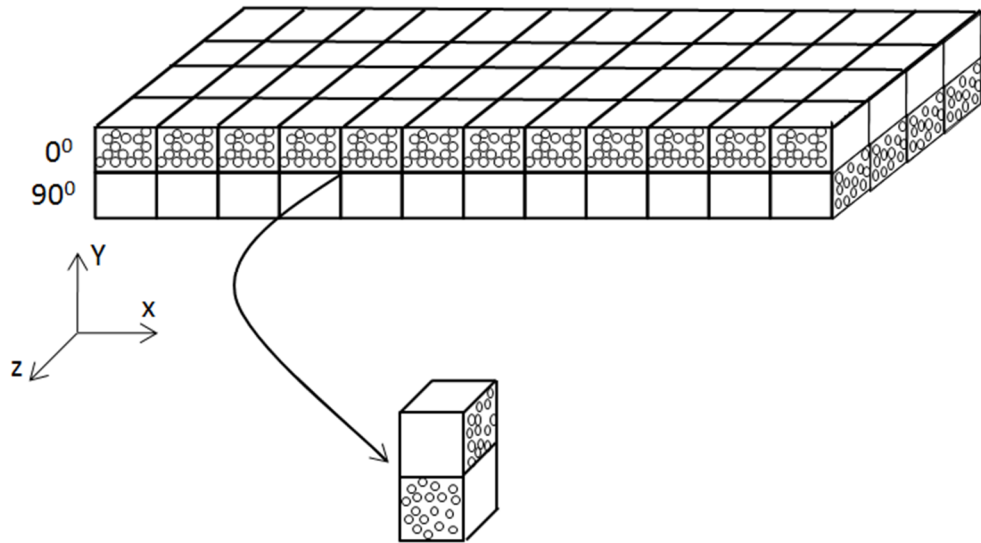


Figure 1.2 Schematic diagram of M^2RVE for cross-ply [0/90] laminate

This work explores the possibility of predicting mechanical properties as well damage response at laminate level using 'multi-fiber multi-layer representative volume element' (M^2RVE). Fig. 1.2 shows the schematic diagram of proposed M^2RVE for cross-ply laminate. Note that this technique is valid for periodic structures.

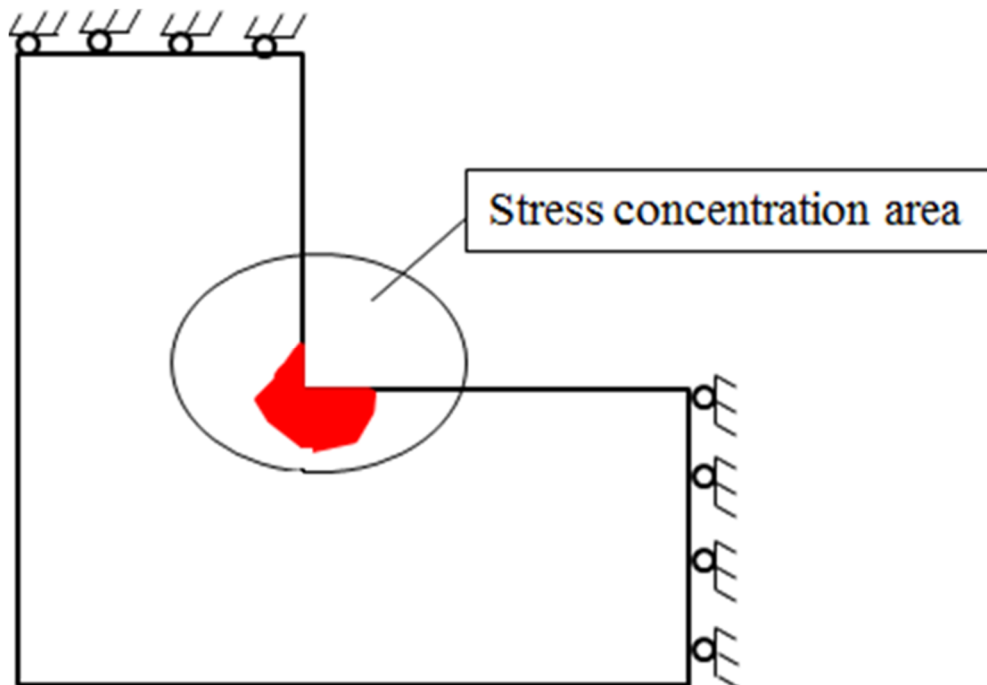


Figure 1.3 Local damage in composite

The periodic homogenization method has major limitation apart from its basic assumptions of uniformity of the macroscopic fields within each RVE and spatial periodicity of the RVE. The uniformity assumption is not appropriate in critical regions of high gradients, and free edges as shown in Fig. 1.3. Interfaces, macro-cracks, neighborhood of material discontinuities and most importantly in the regions of evolving microscopic damage and instability are the potential sites of non-uniformity. Stresses and strains in these regions are several orders of magnitude higher than the average stresses and strains in the structure. The periodicity of simple unit cells is also unrealistic for non-uniform microstructures, due the presence of randomness, clustering or evolving microstructural behavior. Consequently, above mention approach is limited in identifying local damage in real structural members.

To address the limitations of the M^2RVE approach, a micro-macro multiscale modeling is proposed as shown in Fig. 1.4. The micro-macro model is comprised of two levels, namely, microscale and macroscale. Macro level makes use of conventional homogenized material with effective properties obtained from the assumption of periodic boundary conditions (Sun and Vaidya, 1996). The micro level is modeled with the all the microstructural details like fiber and matrix materials. All the details are modeled in order to capture damage initiation and propagation at micro level. It is an effective and computationally efficient technique for modeling the deformation and local damage in real composite structures.

1.2 Problem definition

In order to study all the possible damage mechanisms mentioned in Fig.1, M^2RVE can be used to capture all the damage mechanisms, simultaneously. Different damage failure criterion will be used to model different failure mechanisms. Effect of each constituent on the local as well as global material response will be characterized.

It is known, that results obtained by homogenization of RVE response cannot be used for predicting accurate local damage response of the composite where the assumption periodicity is not valid. Modeling different regions with different approach can be used to handle this issue. Thus, a micro-macro model can be used to capture damage response in real structures. The micro level contains a detailed microstructure is modeled in the region of high stress gradient as shown in Fig. 1.4.

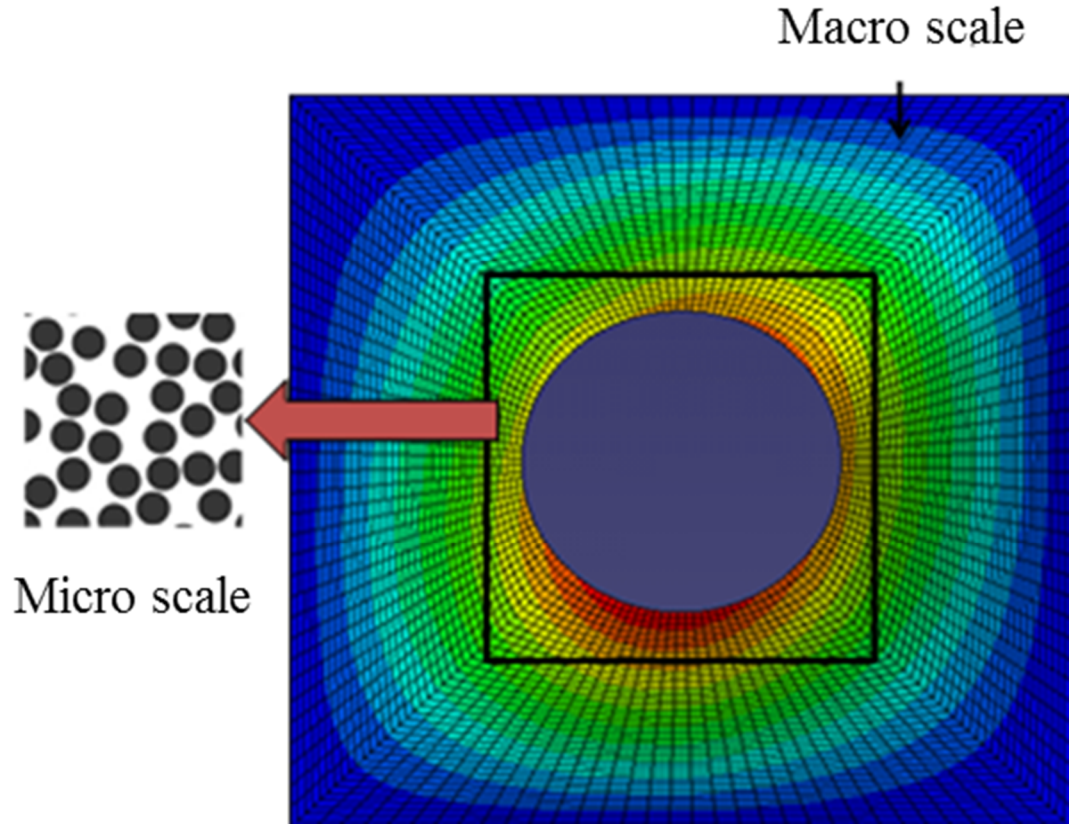


Figure 1.4 Schematic of representative problem using macro-micro approach

1.3 Aim of the present work

The main aim of this thesis is to enhance the fundamental understanding about the local and global damage behavior of composite laminates. Following specific objectives are identified to achieve this goal:

- Implementation of multi-fiber multi-layer representative volume element (M^2RVE) for the prediction of all the damage mechanisms simultaneously including delamination between plies.
- Use of M^2RVE for the prediction of mechanical response to different loading conditions.
- Development and implementation of micro-macro multiscale modeling approach for local damage investigation in real structures.
- Validation of the developed models against experimental data.

1.4 Organization of thesis

The thesis is organized in the form of six chapters. The first chapter provides brief introduction about the problem and objectives of the current research. Chapter 2 provides the critical literature survey mainly on present state of art about multiscale modeling and damage initiation and propagation modeling via multiscale methods in composites. Chapter 3 covers analysis of cross-ply $[0/90]_n$ and angle-ply $[\pm 45]_n$ laminates using M^2RVE . Detailed damage analysis including all damage mechanisms using M^2RVE is presented in chapter 4. Chapter 5 presents development and implementation of micro-macro multiscale modeling technique. Final chapter highlights the findings of the work done.

Chapter 2: Literature Review

2.1 Introduction

The literature review presents prior work done in the relevant areas, namely, multiscale modeling, and application of finite element method to micro-mechanics based multiscale modeling techniques. It covers a work developed using RVE based multiscale modeling methods for periodic media. It also covers work reported in multilevel methods, leading to establishment of micro-macro method.

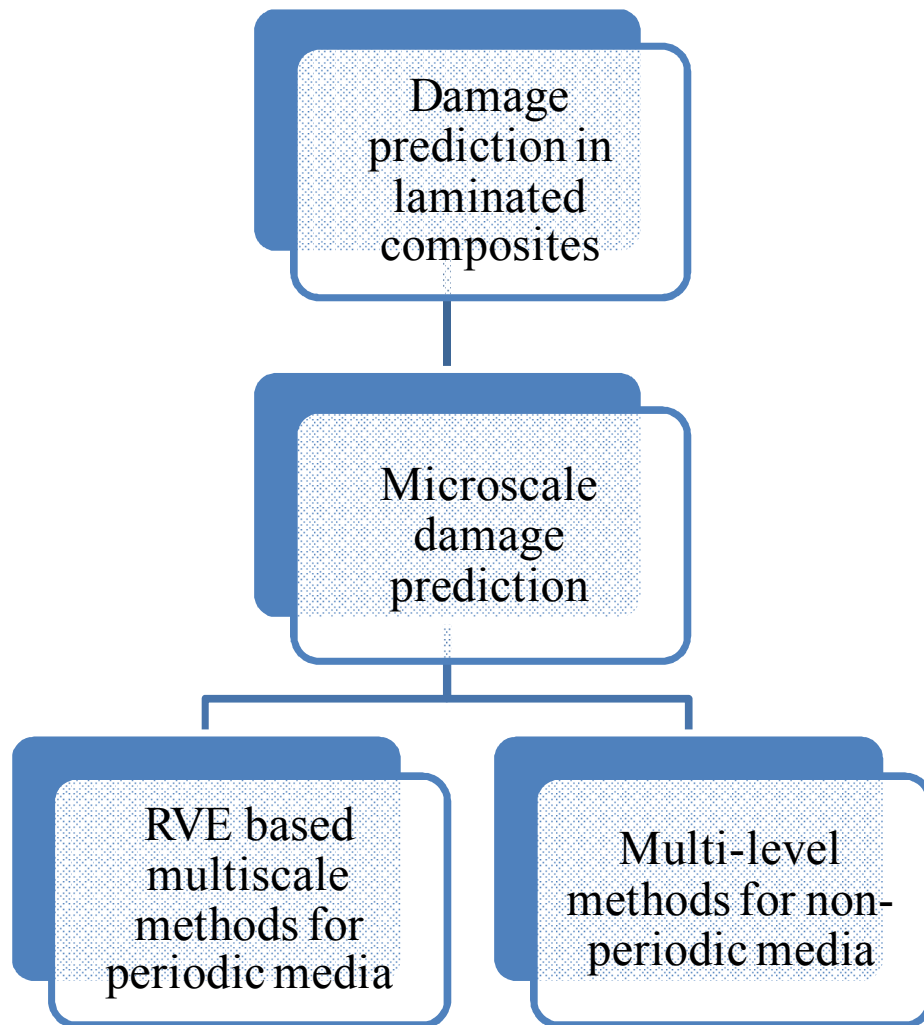


Figure 2.1 Flow chart of literature survey

It is always possible to refer directly to the microscopic scale, but such microscopic models are too complex and expensive to handle for the analysis of large structures. Further, the data obtained would be redundant and complicated procedures would be required to extract needed

information. A way out is multiscale modeling, where macroscopic and microscopic models are coupled to take advantage of the efficiency of macroscopic models and the accuracy of the microscopic models. The scope of such multiscale modeling is to design combined microscopic-macroscopic computational methods that are more efficient than solving the full microscopic model and at the same time give the information that we need to the desired accuracy (Asp et al., 1996). Fig.2.1 shows a flow chart of the literature survey done to understand and implement micro-mechanics based multiscale modeling.

2.2 RVE based multiscale modeling for damage prediction in periodic media

Prediction of overall material behavior of the composites is an essential problem in many engineering applications. It is known that heterogeneous nature of composite material has a significant impact on the macroscopic behavior of the material. The overall behavior of the composite material depends on the size, shape, spatial distribution and properties of the fibers, matrix and interfaces. In order to predict the macroscopic behavior of composites various homogenization methods are proposed over a last two decades. In the homogenization process effective properties of the structure are predicted. Most of the homogenization methods proposed in the literature are not suitable for large deformation and complex loading paths. Only limited number of methods can account for evolving microstructure. With improved computational power of computers computational micromechanics methods have emerged as an accurate tool to study the mechanical behavior of composites. Computation micromechanics makes use of representative volume element (RVE) to predict macroscopic properties of the composite by performing numerical simulation (Michel et al., 1999; Lusti et al., 2002; Segurado and Llorca, 2002; Gonzalez et al., 2004; Smit et al., 1998; Feyal et al., 2000; Terada and Kikuchi, 2001). An RVE usually consists of a single fiber or multiple fibers surrounded by the matrix material and the interface between the fiber and the matrix. The properties of the constituents (phase and interface) are used for the prediction of effective properties of the lamina. The lamina properties are then used for the prediction of macroscale stresses in the laminate.

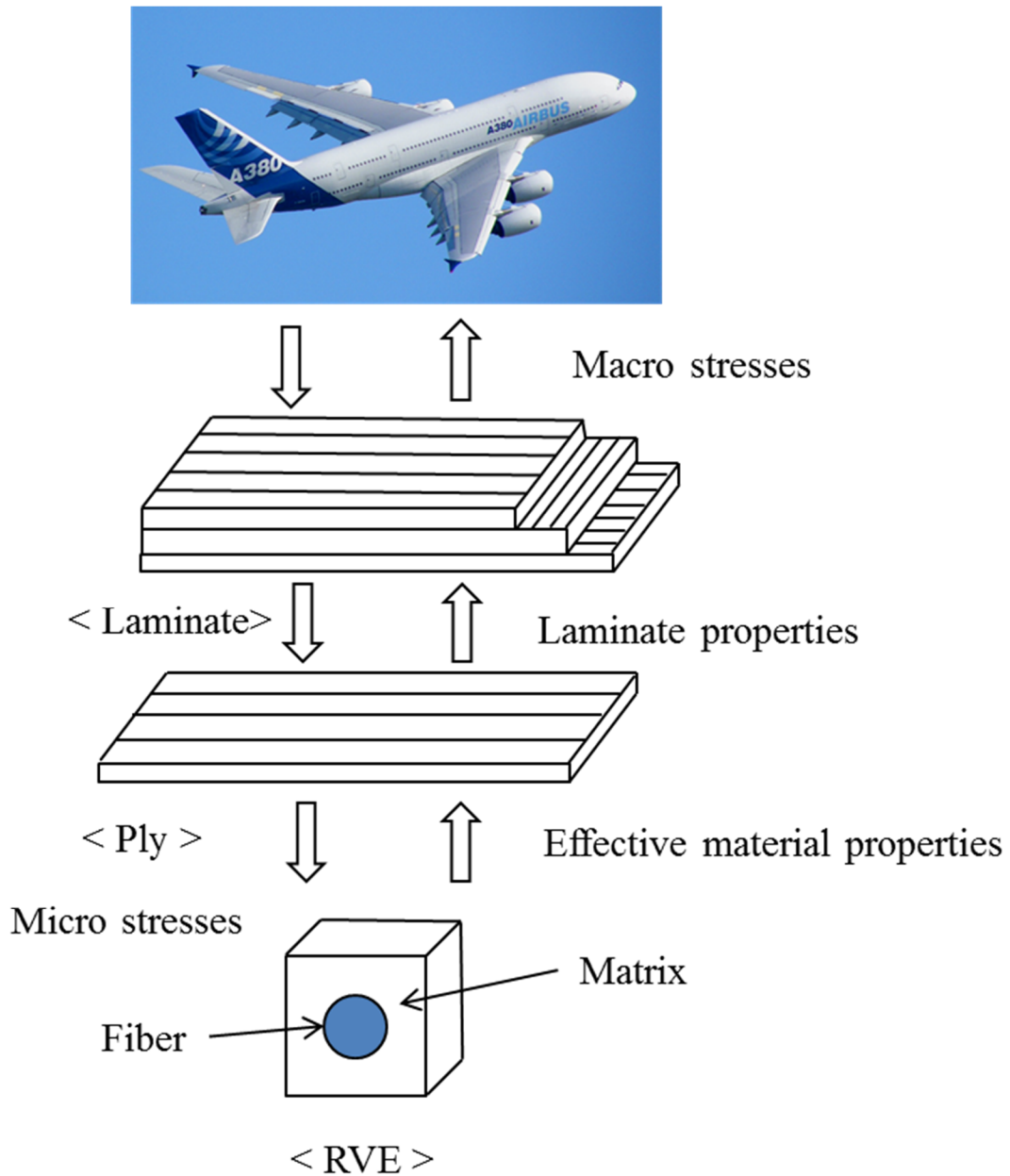


Figure 2.2 General methodology used in multiscale modeling of composite laminates
 Fig. 2.2 shows a typical approach used in modeling of composites. It also describes the flow of information from one scale to another. Computational micromechanics provide three important advantages when compared with classical homogenization theories:

- Computational homogenization permits to study effect of constituent size, shape and clustering on macroscale material response.

- It is possible to predict damage initiation and propagation using stress and strain fields throughout the microstructure.
- It is possible to study large deformation of evolving microstructure using computational homogenization.

Many researchers have used computational micromechanics to study the effect of the reinforcement particle shape (Chawla et al., 2006), reinforcement particle clustering (Segurado et al., 2003; Segurado and Llorca, 2006) and the influence of constituent's damage (Bohm et al., 2004; Llorca and Segurado, 2004) on the mechanical behavior of the particulate composites. The microstructure of the particulate composite may be obtained by using computer assisted microscopy (Youssef et al., 2005; Borbely et al., 2006). To understand computational micromechanics it is important to study definition and implementation of representative volume element (RVE). In the next section, implementation and use of representative volume element has been explained.

2.2.1 Representative volume element (RVE)

If it is assumed that the composite is made up of nearly regular structure, it is possible to imagine that the structure is made up of many repetitive unit cells or RVE as shown in Fig 2.3. The important assumption is that two length scales associated with macrostructure and microstructure should be separated as shown in Fig. 2.4.

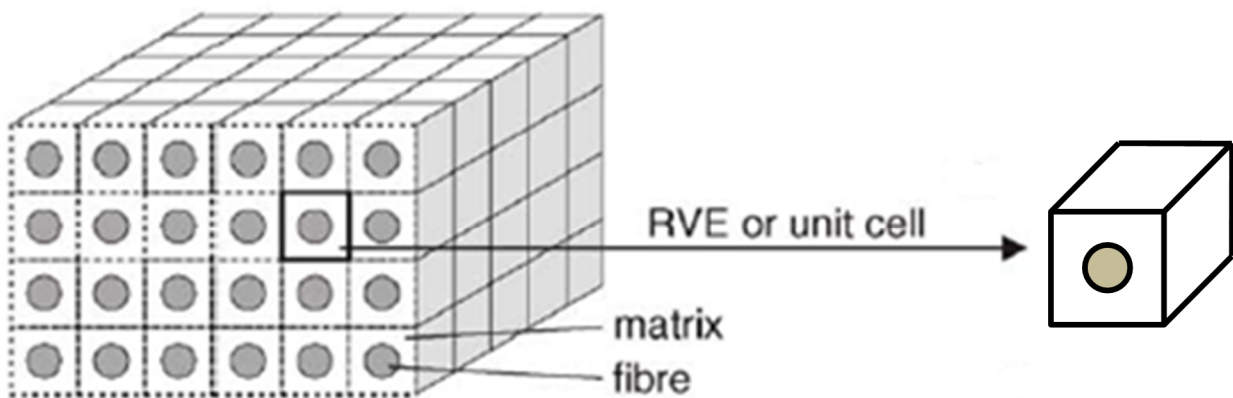


Figure 2.3 Typical representative volume element (RVE)

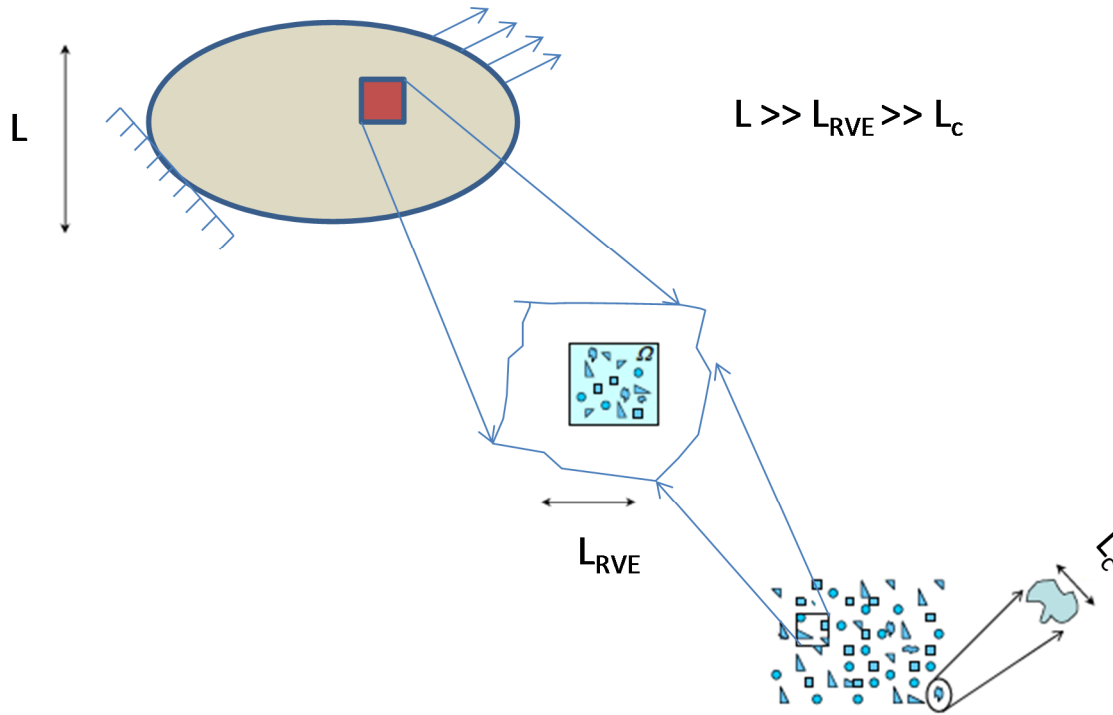


Figure 2.4 The size requirement of a representative volume element

The RVE is commonly defined as a cube of material with dimension L_{RVE} subject to the following conditions (Jones, 1999)

$$\frac{d}{L_{RVE}} \ll 1, L_c \leq L_{RVE} \leq L, \quad (2.1)$$

Where d is the characteristic size of micro constituents, L_c is the heterogeneity length, L is a characteristic macroscopic structural dimension, (Jones, 1999). The macroscopic properties of the composite lamina can be determined by using computational micromechanics via homogenization process. In a homogenization process, the effective stresses and strains acting on a statistically representative volume element (RVE) or unit cell are calculated. Computational micromechanics is then used to predict the overall behavior (local and global) of the composites from the fiber, matrix and fiber-matrix interface properties via an RVE analysis as described in Kanoute et al. (2009). Similar approach has been used by Geers et al.(2010) and Sun and Vaidya (1996). Kaseem (2000) and Teradaa et al. (2000) have demonstrated that the effective behavior obtained using periodic boundary conditions is always bounded by those obtained using force and displacement boundary conditions as shown in Fig 2.5. Thus, for the analysis of composites, most of the RVEs/unit cells make use of periodic boundary conditions as described by Berger et

al.(2005), Tyrus et al.(2007), and Xia et al. (2006). Periodic boundary condition assumes that the structure is repetitive in nature as described in Fig 2.3. Details about periodic boundary conditions and its implementation have been explained in Chapter 3.

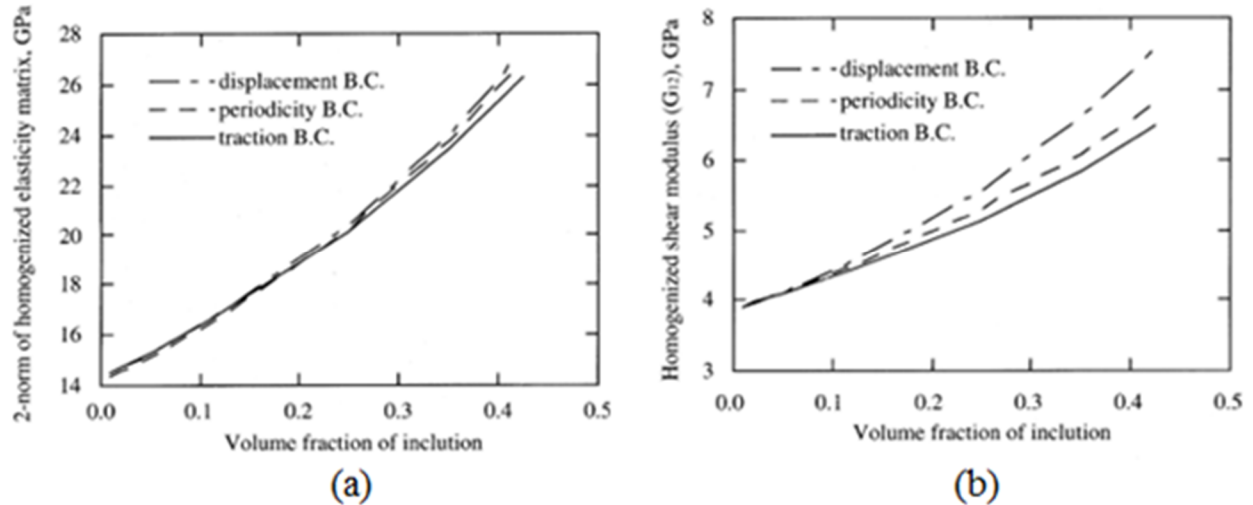


Figure 2.5 Homogenized material properties vs volume fractions of inclusions: (a) in two-norm of homogenized elasticity matrix; (b) in homogenized shear modulus G_{12} (Teradaa, 2000)

The finite element method (FEM) was used to predict the material response and damage behavior of the composite materials using an RVE in Mahmoodia et al. (2011), Ng et al. (2010), and Taliercio et al. (1999). Fig. 2.6 shows typical fiber arrangement used in RVE formulation (Jones, 1999).

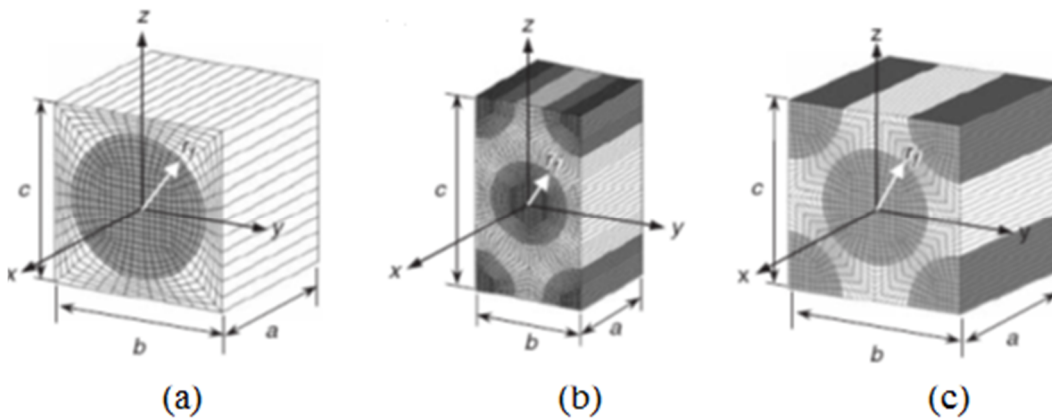


Figure 2.6 FE model of RVE; (a) Square array, (b) Hexagonal array, (c) Diamond array (Jones, 1999)

2.2.2 Implementation of RVE for damage prediction

Many researchers have used multi-fiber RVE using periodic boundary conditions for the prediction of damage response of composites. Gonzalez and Llorca (2007) have done pioneer work in use of RVE for prediction of damage response. A 2D representative volume element model of Hexcel epoxy matrix reinforced with 57% of AS4 carbon fibers subjected to transverse compression was used. Random and homogeneous dispersion of circular elastic fibers embedded in the matrix were modeled to simulate composite microstructure as shown in Fig. 2.7. Matrix and interface failure have been taken into account to model the total failure.

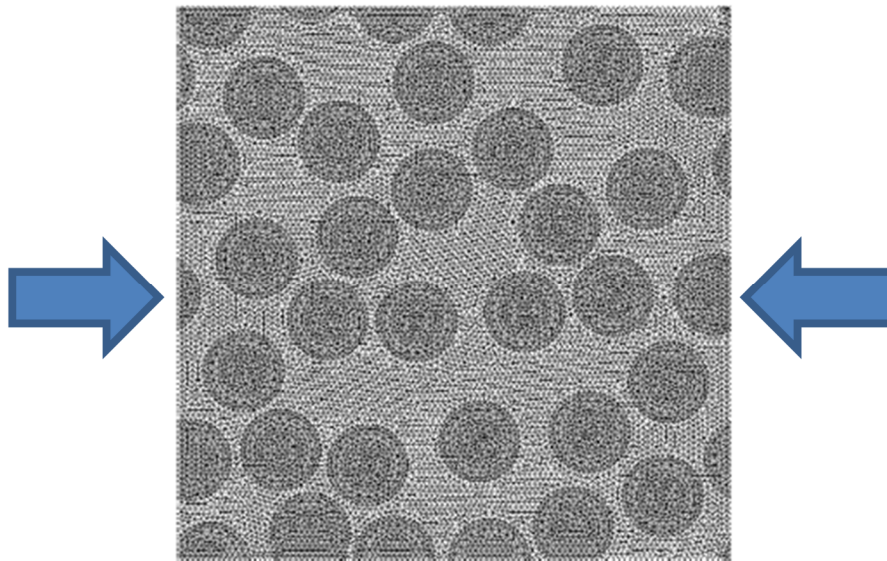


Figure 2.7 Fiber distribution and finite element discretization of a representative volume element of the composite (Gonzalez and Llorca, 2007)

A parametric study was performed to study effect of failure strength of fiber, matrix and interface on the global stress-strain response. It was found that compressive loading leads to formation of bands of plastic deformation in the matrix, inclined at an angle of 56° with respect to the plane perpendicular to the loading axis. The formation of plastic bands at 56° was in line with the experimental findings. Interfacial damage followed the formation of matrix shear bands. It was observed that the strength of fiber-reinforced polymers under transverse compression is controlled by the matrix and the interface damage alone. The study demonstrated that computational micromechanics can effectively and accurately capture matrix failure and interface damage in composite materials. The Hexcel epoxy matrix material was modeled as anisotropic and elastic-plastic material following Mohr-Coulomb yield criterion. Fiber-matrix

decohesion was modeled using standard traction separation law. Parametric study was performed to ensure that the correct size of RVE is selected. It was found that an RVE with 70 fibers provides the same estimate of stresses and strains as the RVE with 30 fibers. Therefore, the RVE with 30 fibers was used for all the subsequent simulations.

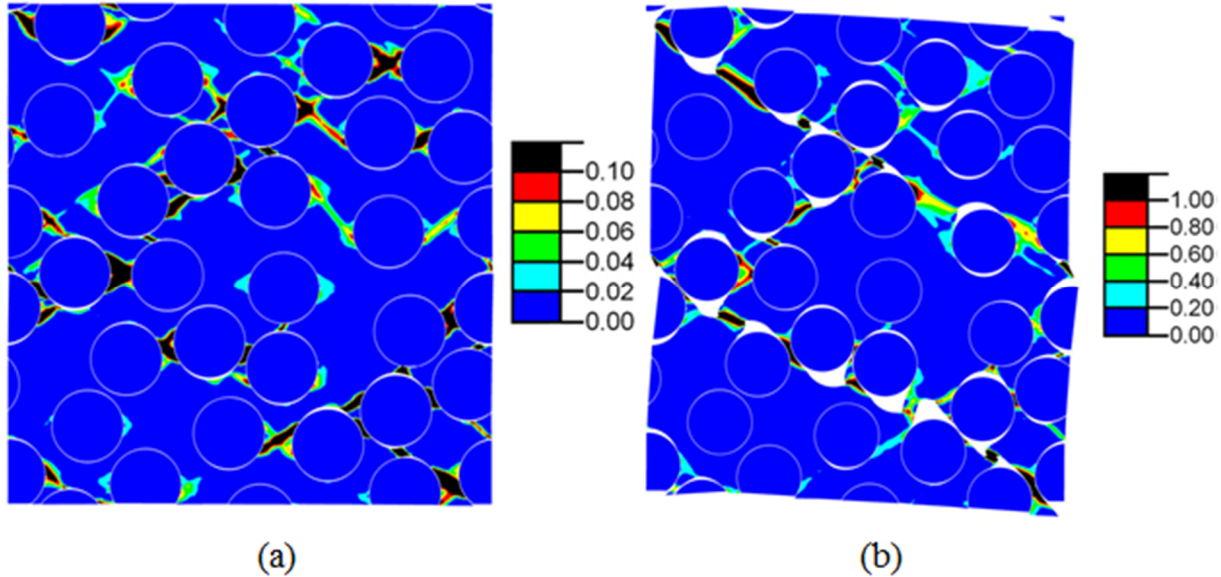


Figure 2.8 Contour plot of the accumulated plastic strain in the matrix in the composite with low interfacial strength (a) = 1.7% corresponding to the maximum strength. (b) = 4% (Gonzalez and Llorca., 2007)

The values of friction angle and cohesive strength of the matrix material were estimated by using compressive and tensile strength of the matrix material. The value of the interfacial stiffness was kept high to ensure displacement continuity at the interface and avoid modification of the stresses around the fibers in the absence of damage. Fig 2.8 shows contour plot of accumulated plastic strain developed in matrix for low interfacial strength. It was concluded that interfacial strength has a significant effect on the formation of matrix bands and eventually final failure. It was observed that the interfacial cracks are generated at very low stresses in composites with weak interfaces. With an increase in loading strain, the amount of interfacial damage increases. Parametric studies showed that matrix friction angle has significant effect on the compressive strength of the composite. The matrix was more susceptible to the formation of shear bands as the friction angle increased. Changes in the interface fracture energy by two orders of magnitude did not alter the compressive strength significantly.

Totry et al. (2008) used a 2D RVE proposed by Gonzalez and Llorca (2007) to study the mechanical behavior of a fiber-reinforced composite lamina under combined loading of

transverse compression and out-of-plane shear. The results showed that the proposed model was able to accurately reproduce the physical fracture mechanisms observed experimentally. The proposed methodology opens the possibility of replacing costly and time consuming mechanical tests by virtual tests. It was shown that virtual tests provided full control of composite microstructure as well as constituent properties. Virtual tests also provide opportunity to apply very complex loading and boundary conditions. Virtual tests can be useful to determine optimum composite properties for a particular loading. For the composites with higher fiber-matrix interfacial strength, the failure locus computed from the numerical simulations was consistent with the failure locus predicted by Hashin (1980), Puck and Schurmann (2002) and LaRC failure criterion used in Davila et al. (2005). In the studies done by Hashin (1980), Puck and Schurmann (2002) and Davila et al. (2005) the only experimental parameter considered was the strength of the composite lamina under transverse compression. The formation and location of plastic strain in the matrix in the form of shear bands was found to be in line with the one predicted by Puck and Schurmann (2002) and LaRC models. For a weak fiber-matrix interface, the dominant failure mechanism was interfacial decohesion rather than matrix plastic deformation. The numerical simulations points out this new mode of failure, namely, interfacial decohesion. It was suggested that interfacial debonding should be consider to have realistic estimate of the damage response in the composites.

Totry et al. (2009) proposed a 3D RVE for the prediction of shear-strain response of the composites subjected to in-plane shear loading as shown in Fig 2.9. Periodic boundary conditions have been applied on all the faces of the RVE to simulate the macrostructure. To capture in-plane shear deformation of the cross-ply laminate as shown in Fig. 2.9, two different simulations were performed on the same RVE. In the first simulation load is applied parallel to fibers and the volume averaged stresses strains at each instant were captured. In the second simulation load was applied perpendicular to fibers and volume averaged stresses and strains were noted at each instant. The estimate material response of the cross-ply laminate, arithmetic mean of the stresses and strain at each instance has been used. It was assumed that there is no inter-ply failure.

It was observed that shear parallel to the fibers creates localization of deformation in the matrix causes formation of shear bands parallel to the fibers. Fiber rotation becomes inevitable to accommodate the shear strain in the matrix in case of shear perpendicular to the fibers. This

causes hardening of the lamina during non-linear deformation. Differences were observed in shear response of the lamina parallel and perpendicular to the fibers as shown in Fig. 2.10. These differences are not taken into account in laminate theory, but these differences cannot be ignored in order to accurately estimate the maximum shear load borne by the laminate.

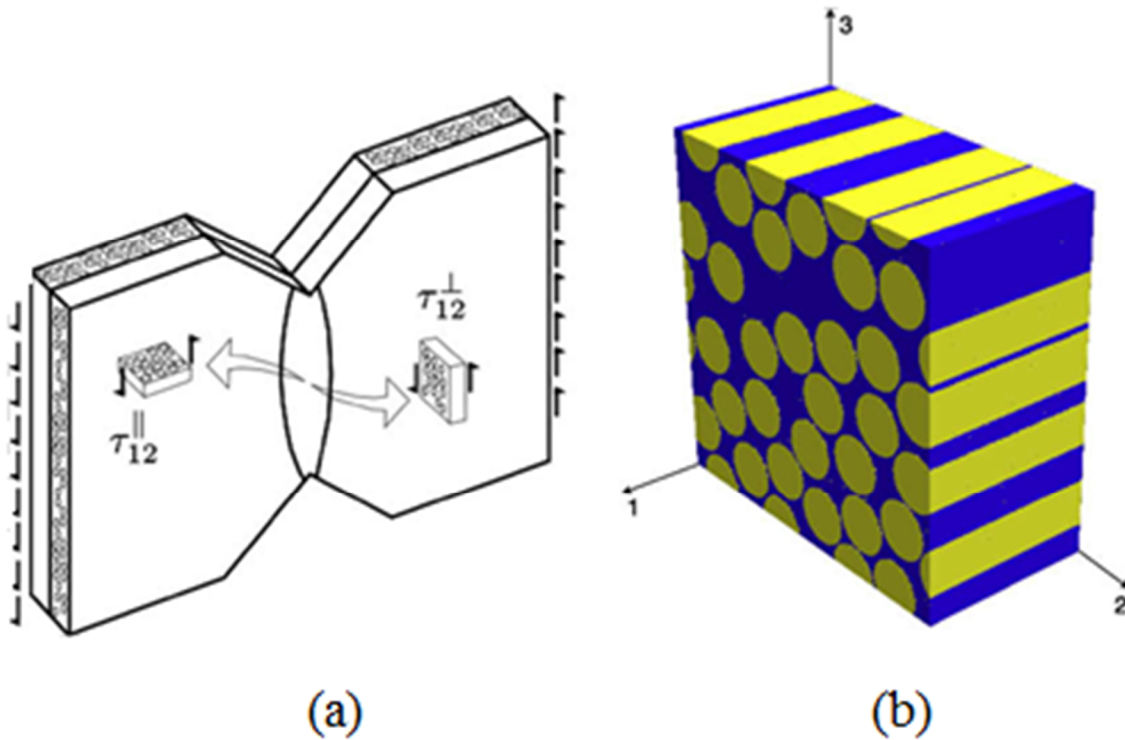


Figure 2.9 (a) Schematic of the simulation strategy to model the in-plane shear behavior of the cross-ply composite through the combination of loading parallel and perpendicular to the fibers. (b) Representative volume element of the lamina microstructure (Totry et al., 2009)

The differences observed can be utilized for developing accurate model for the composite including damage. In case of using continuum damage mechanics (Ladev ze and Lubineau 2001; Camanho et al. 2007; Maim  et al. 2007), it is assumed that the damage response is same when shear loading is applied parallel or perpendicular to the fibers. It was observed that direction of failure propagation is controlled by the orientation of the fibers when loaded in shear. The direction of the damage propagation may not follow the maximum stress concentration (Der Meer and Sluys 2008). Therefore the proposed model was said to provide better understanding about the damage of composites when subjected to in-plane shear as compared to continuum based damage models.

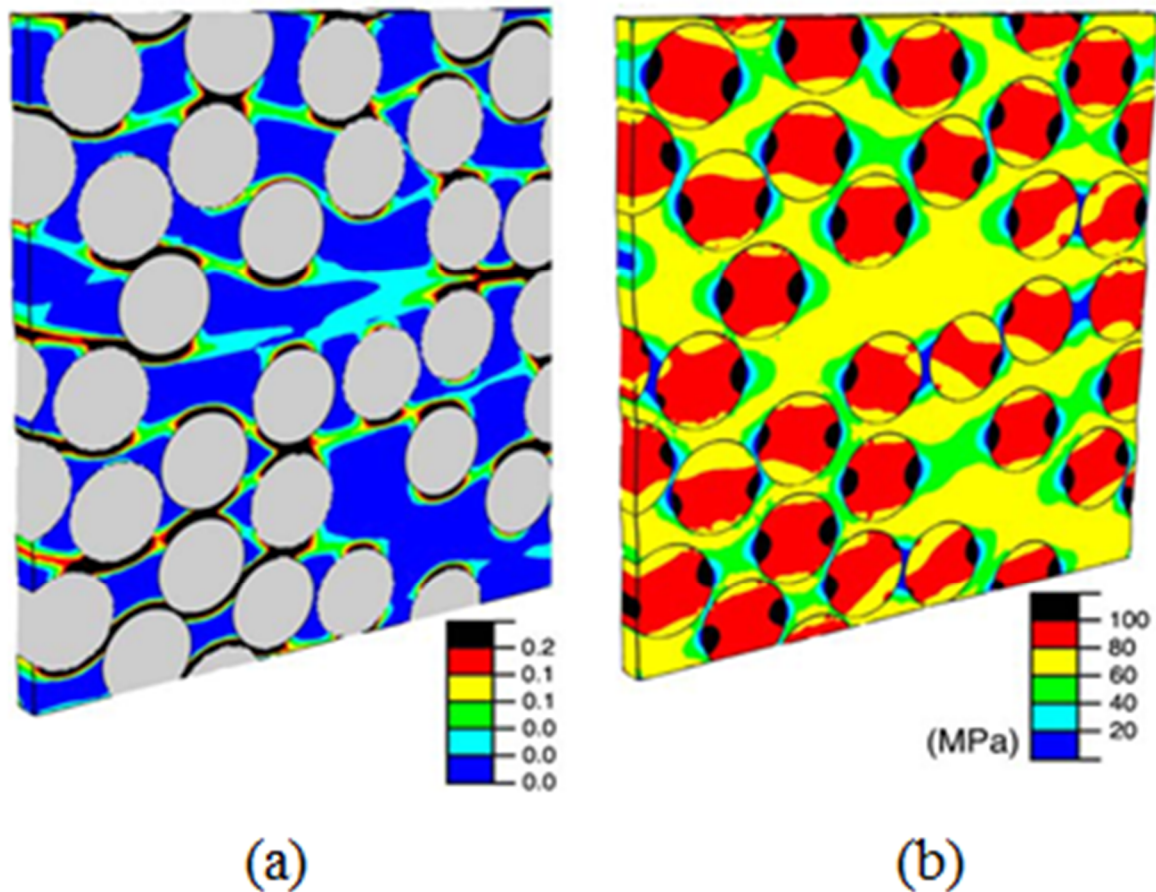


Figure 2.10 (a) Contour plot of the accumulated plastic strain in the matrix for the lamina deformed under in-plane shear perpendicular to the fibers. (b) Contour plot of the shear stress, τ_{12} for the lamina deformed under in-plane shear perpendicular to the fibers. The far-field applied shear strain was $\tau_{12}=4\%$ (Totry et al. 2009).

Totry et al. (2010) studied the effect of micro constituent's properties and spatial distribution on the macroscopic performance. They have used two composites, one with high strength fibers and another with high modulus fibers. Experiments were performed on both the cross ply composite laminates using V-notch rail shear test. Numerical simulations showed the complex deformation and damage mechanism observed during experiments. It was found that interfacial layer properties (between fiber-matrix) significantly affect the macroscale material response in both the cases. The stress-strain responses for both the laminates show that the slope of the linear hardening region after yielding decreases rapidly with a decrease in the interfacial strength. The strain to failure also changes significantly with a decrease in the interfacial strength. It was found that the shear strength of the cross-ply composite is equal to the fiber-matrix interfacial strength.

Totry et al.(2008) have used 3D RVE to predict failure locus of C/PPEK composite subjected to combination of transverse compression and longitudinal shear as shown in Fig 2.11. The predicted failure locus predicted was compared with the predictions by using theory proposed by Puck and Schurmann (2002) and LaRC failurecriterion used in Davila et al. (2005).

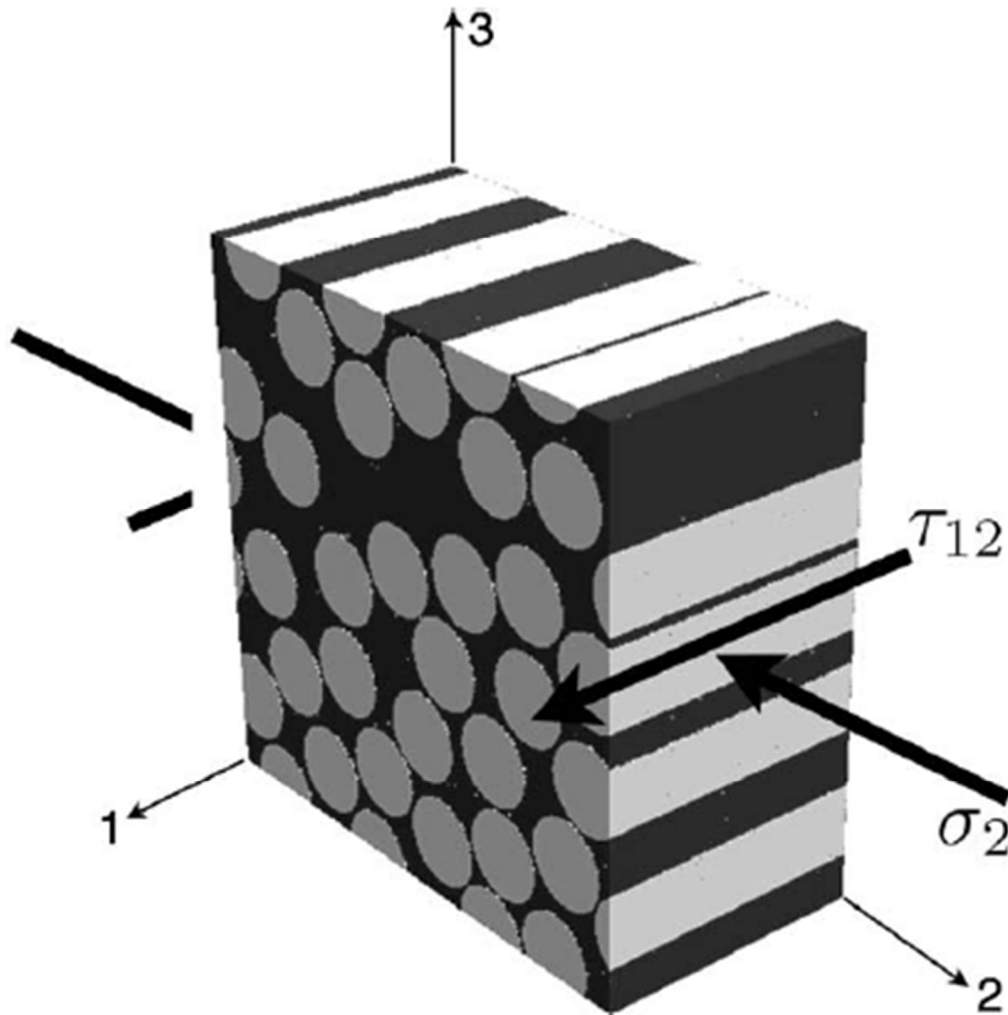


Figure 2.11 Schematic of the representative volume element of the lamina microstructure subjected to transverse compression and longitudinal shear (Totry et al., 2008)

Fig. 2.12 shows experimental results (Vogler and Kyriakides, 1999) as well as predictions of the Puck and Schurmann (2002) and LaRC03 model used in Davila et al. (2005) along with results obtained by performing numerical simulations and experiments. It was observed that numerical simulations using RVE can provide accurate estimate of the failure envelope.

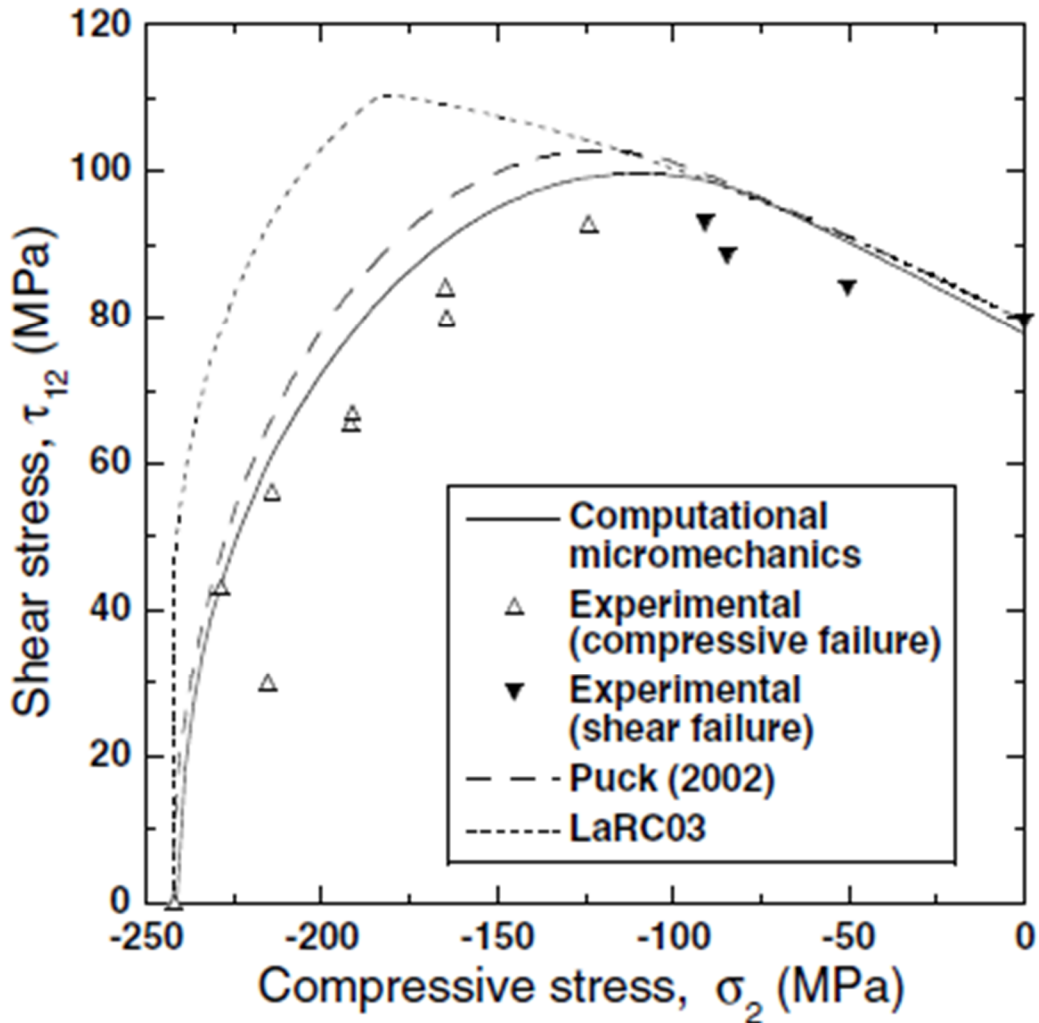


Figure 2.12 Failure locus under transverse compression and longitudinal shear (Totry et al., 2008)

A micromechanical numerical algorithm to determine the homogenized elastic properties of bidirectional fibrous composites has been presented by Abolfathi et al. (2008). A repeating unit cell (RUC) to represent the microstructure of the composite was proposed based on a bidirectional fiber packing. For angular bidirectional fiber distribution, the symmetry lines define a parallelepiped unit cell as shown in Fig.2.13. The proposed RUC represents the periodic microstructure of an angular bidirectional fiber composite. Finite element analysis of RUC under six possible independent loading conditions was carried out. A volume averaging scheme is implemented to determine the average response. In this work the main focus was on the impact of the fiber cross angles on the stiffness properties of the composite. The accuracy of the results

of this micromechanics modeling was compared with the stiffness solutions from laminate theory.

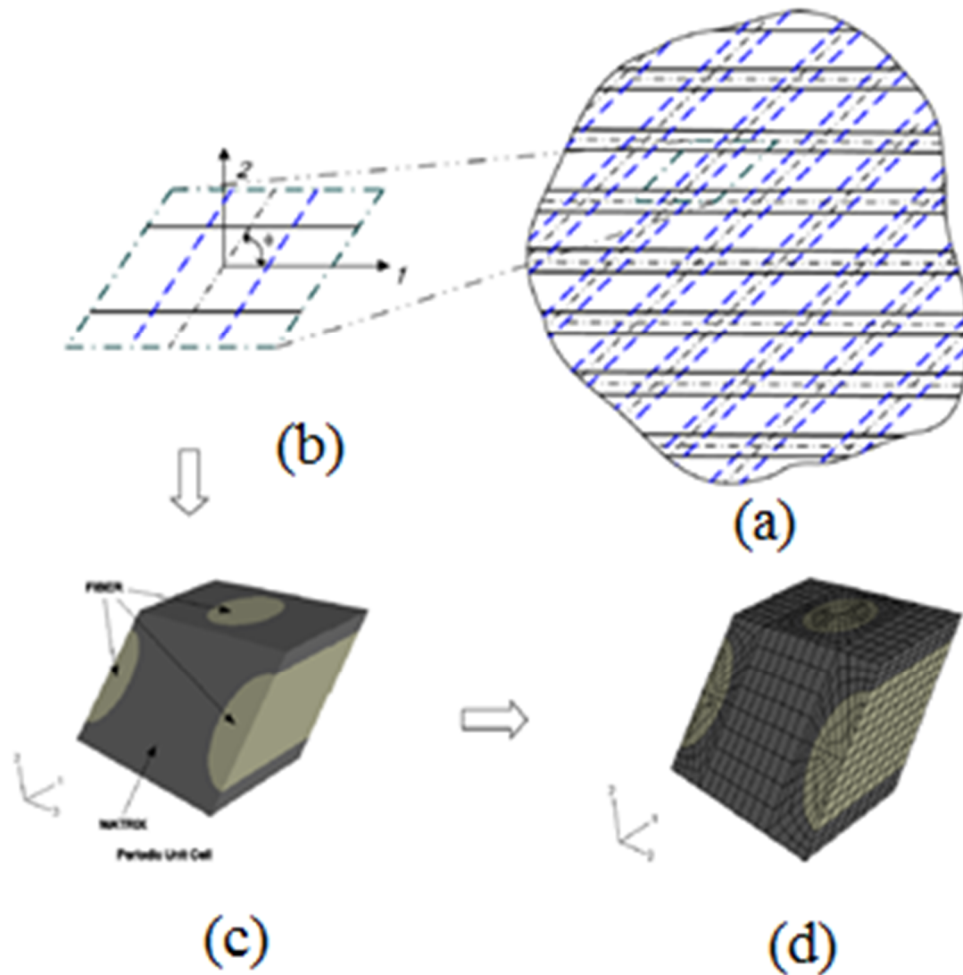


Figure 2.13 (a) The bidirectional fibers at cross angles embedded in matrix, (b) the cross-sectional view of a unit cell, (c) the periodic 3-D unit cell volume, and (d) the FEM discretized of the RUC (Abolfathi et al., 2008)

In addition, some results presented showed the impact of fiber volume fraction on the material properties of the composite. The volume average scheme provides the homogenized stresses and strains. This study demonstrated the method to evaluate the optimum angle for fibers to be inserted in matrix to achieve the best mechanical property in all directions. Fiber ply angle can be calculated based on the maximum stiffness required in certain direction. This tool was found to be extremely helpful for design and manufacturing of bidirectional fibrous composite materials.

Canal et al. (2009) studied the mechanical behavior of uniaxial fiber-reinforced composites with a ductile rubber-toughened epoxy matrix using computational micromechanics. The fibers were modeled as elastic and isotropic solids, while the rubber-modified epoxy matrix was modeled as anelastic-viscoplastic material. It was evident that the failure criterion such as Mohr–Coulomb or Drucker–Prager generally used for modeling failure of the brittle epoxy matrix material are not suitable for rubber toughened epoxy, which shows extensive plastic deformation prior to fracture. Therefore, the matrix flow stresses were assumed to follow the model developed by Jeong (Jeong, H.Y., 2002). A parametric study was performed to assess the influence of interface strength on the composite behavior. The RVE was subjected to transverse tension and out-of-plane shear to establish the effect of loading conditions on the dominant failure micro-mechanisms. In addition, the corresponding failure locus was obtained and compared with the phenomenological failure criterion for composites presented in literature. The range of validity and the areas for further improvement for these criteria were established by comparison with the numerical results.

A simple procedure to determine the non-linear in-plane shear response of laminated composites has been presented by Ng et al. (2010). They used experimental results of $\pm 45^\circ$ symmetric laminate tensile test to validate the results. The aim of the method was to characterize the lamina shear response and the in-situ matrix shear response. Non-linear shear stress response was computed by load, and axial and transverse strains measured in the tests. From the experimental results, the in-situ matrix equivalent stress–strain response was obtained. An RVE of $\pm 45^\circ$ symmetric laminate as shown in Fig. 2.14 was used to determine the accuracy of the non-linear response of the in-situ matrix. A $\pm 45^\circ$ laminate tensile test can be used to extract the linear elastic matrix shear stress–strain response using Concentric Cylinder Assemblage (CCA) model. CCA relates the matrix properties to the lamina properties. In the work presented in Ng et al. (2010) a procedure for extracting the full non-linear response of the in-situ matrix from the uniaxial tension test results of a $\pm 45^\circ$ symmetric laminate was described. The algorithm to obtain the complete non-linear response of the in-situ matrix from a single uniaxial test was proposed. Fig. 2.15 shows the formation of matrix cracks due to diagonal tension during tensile test of $\pm 45^\circ$ symmetric laminate.

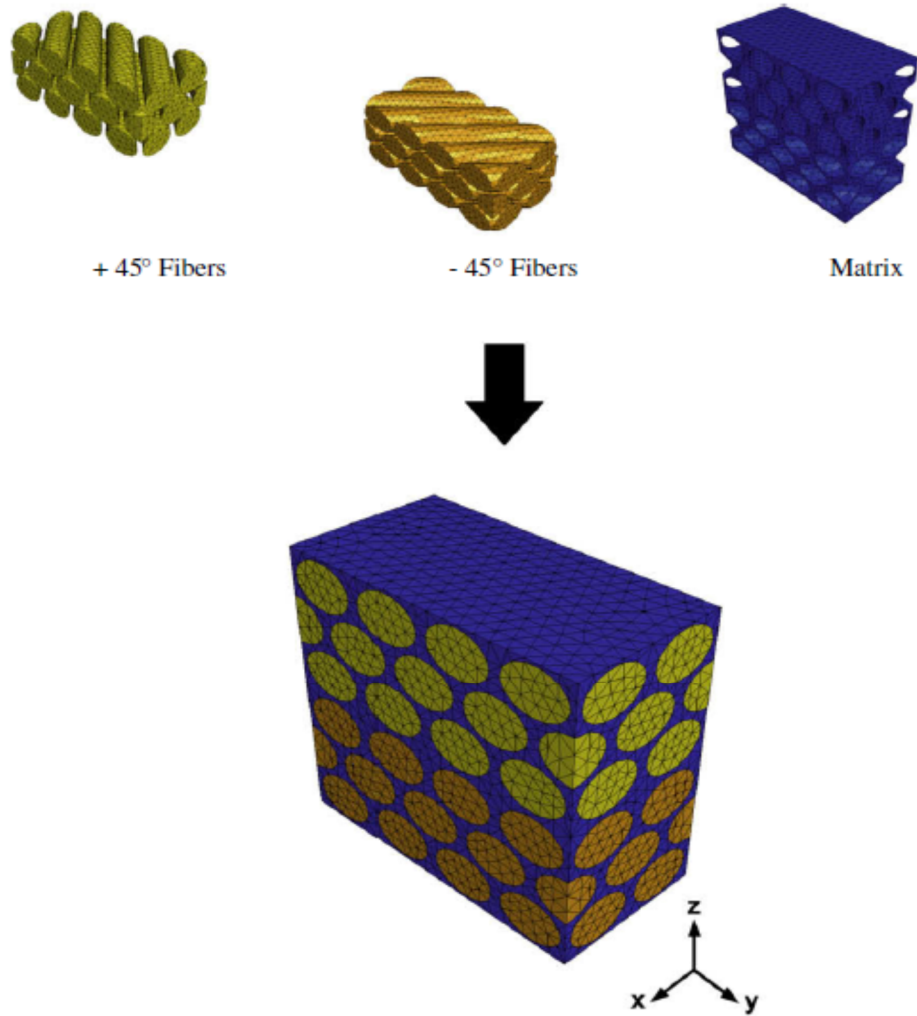


Figure 2.14 Constituents and final assembly of FE model of 1 RC (Ng et al.2010)

It may be noted that there are very few studies reported in the literature which model fiber failure using RVE and/or computational micromechanics. Damageable layers modeled with surfaced-based cohesive behavior were randomly placed as shown in Fig. 2.16 in the fibers to capture damage in fibers by Wang et al. (2011). The stiffness of the cohesive element layer was kept same as that of the fiber material in order to avoid any alteration in elastic response of the composite. With an increase in the load, the damageable layer fails at the designated strength.

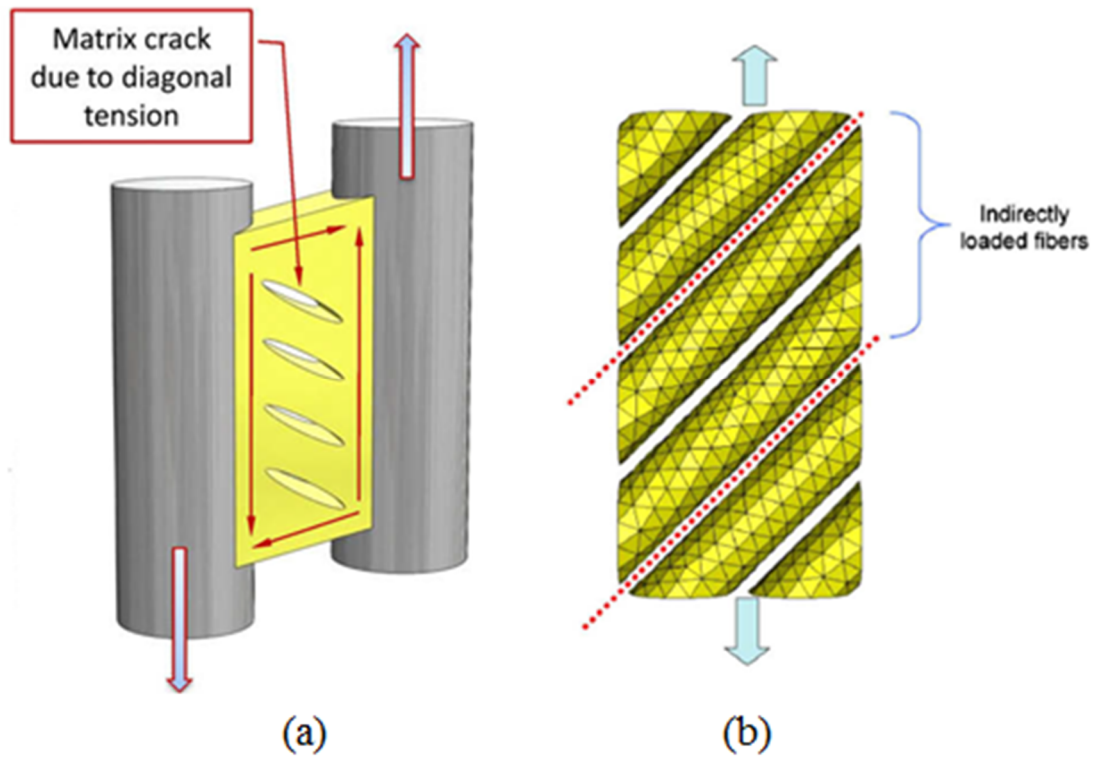


Figure 2.15 Formation of matrix shear cracks between adjacent fibers (b) Indirect loading of fibers in case of $[45]$ composite (Ng et al., 2010)

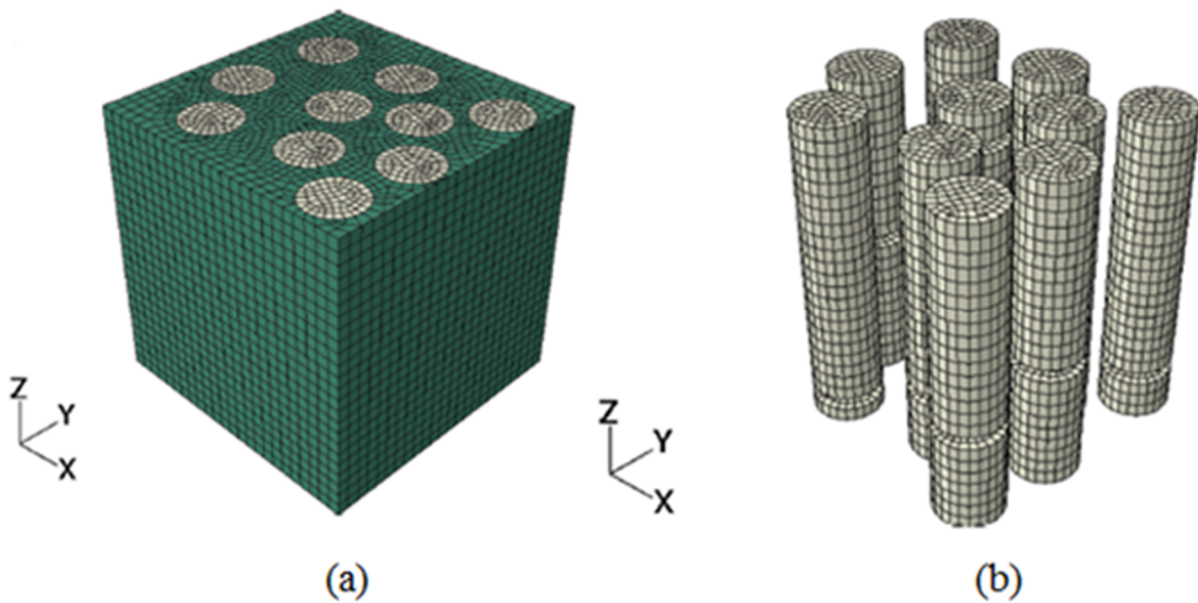


Figure 2.16 Multi-fiber FE model with one damageable layer in every fiber: (a) cell model, (b) fibers in the model with removed damageable layers (Wang et al., 2011)

In FE^2 method proposed by Feyal et al. (2000), the microscopic analysis was performed using homogenization of the periodic media. An RVE was assigned to each integration point at the macroscopic scale and a separate finite element computation is performed simultaneously as shown in Fig. 2.17. The local stresses were determined on a representative unit cell of the microstructure of the material microstructure with periodic boundary conditions and macroscopic fields were determined at each integration point of the structure. Macroscopic response was obtained by volume averaging the stresses and strains over an RVE. This method assumes that all points in the structure are periodic and microscale and macroscale is properly separated from one another, i.e., the microstructure is very small as compared to macrostructure. However, the assumption of periodicity is lost at the points close to free edges or points of high stress concentration, and these approaches cannot be used in these areas. Even for geometrically periodic microstructures, periodicity assumptions may not be appropriate when deformation or damage is localized. Another limitation of this technique is that it requires more time and memory and thus can be effectively applied for primarily two-dimensional problems.

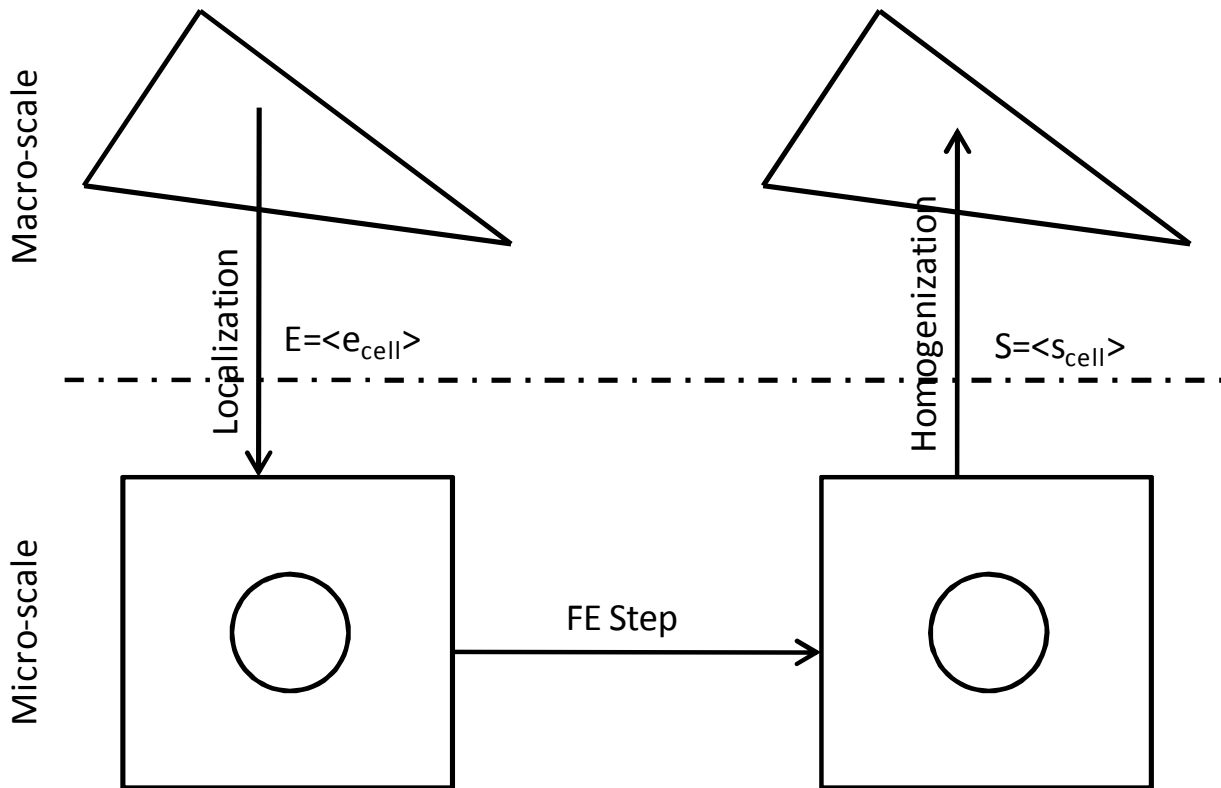


Figure 2.17 Schematic of FE^2 method (Feyal et al., 2000)

Another approach called as hierarchical multiscale modeling, which differentiates between the regions requiring different resolutions, is an effective tool for modeling deformation and damage in heterogeneous materials. Sub-structuring in these models enables pure macroscopic analysis in certain parts of the domain using homogenized or effective material properties and zooming in for local or microscopic modeling at a different scale in other regions of the domain. Such issues in modeling various heterogeneities were addressed by Pagano and Rybicki (1974), Oden and Zohdi (1997), Fish et. al.(1995) and Ghosh et. al. (1995,1996). They have introduced a domain decomposition method to accommodate hierarchical modeling of composite materials. Zohdi and Wriggers (1999) have also used domain decomposition of the heterogeneous domain into non-overlapping sub-domains. Most of these models are limited to linear elastic behavior.

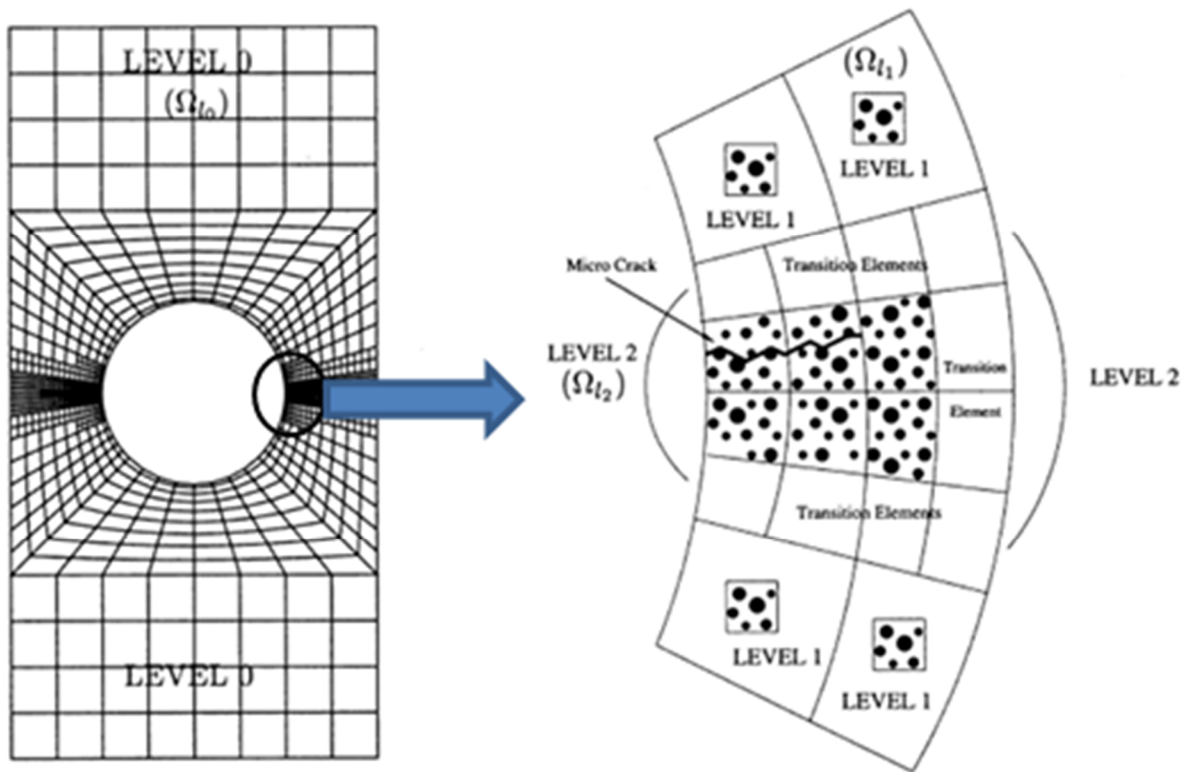


Figure 2.18 Schematic of multi-level method (Ghosh et al., 1995)

Analysis of microstructural response with arbitrary distributions, shapes and sizes of heterogeneities is effectively done by the Voronoi Cell finite element model (VCFEM) (Ghosh and Moorthy; 1995, 1996). A high level of computational efficiency with sufficient accuracy and resolution was achieved for elastic and elastic-plastic materials. The multi-level methodology developed in (Ghosh et al., 1995) addresses issue of differential scale issue by differentiating between non-critical and critical regions zooming in at 'hotspots' for pure microscopic simulations. The multilevel model proposed by Ghosh et al. (1995) is comprised of three levels, namely, macro, transition and micro as shown in Fig. 2.18. Macro level or level 0 makes use of conventional homogenized material with effective properties obtained from the assumption of periodic boundary conditions. Level 1 or transition elements are required to model with the advance multiscale modeling technique such as FE². The level 2 elements are model with the all the microstructural details like fiber and matrix materials. All the details are modeled in order to capture damage initiation and propagation at micro level. Several applications of the method to account for nonlinearity in composites have been presented in recent papers. This is a fully coupled micro-macro technique, thus computationally expensive.

2.2.3 Multi-layer representative volume element

Single layer RVE presented above is suitable for modeling a lamina. The laminate theory is then used to predict the material response of the laminate. Inter-ply damage is neglected in this case. To address these limitations of single layer RVEs (i.e. an RVE for the lamina), a multi-layer RVE (i.e. an RVE for the laminate) could be used to predict the damage response and the material behavior accurately as shown in Fig.2.19. A cubic meso/micro rhombohedral single fiber multi-layer RVE as shown in Fig. 2.20 has been proposed for the prediction of mechanical behavior of any angle ply laminate by Xia et al. (2000, 2003). For the angle-ply laminates, special meso/micro rhombohedral RVE as shown in Fig. 2.20 was developed. It can be seen as a periodical array of this unit cell as shown in Fig.2.19. An explicit unified form of boundary conditions stated by Suquet (1987), suitable for FEM analyses of parallelepiped RVE models was proposed. It was assumed that fibers are uniformly distributed in the matrix and have the same diameter. Therefore, each unidirectional layer could be represented by a unit cube with a single fiber having the same fiber volume fraction as the ply as shown in Fig. 2.19.

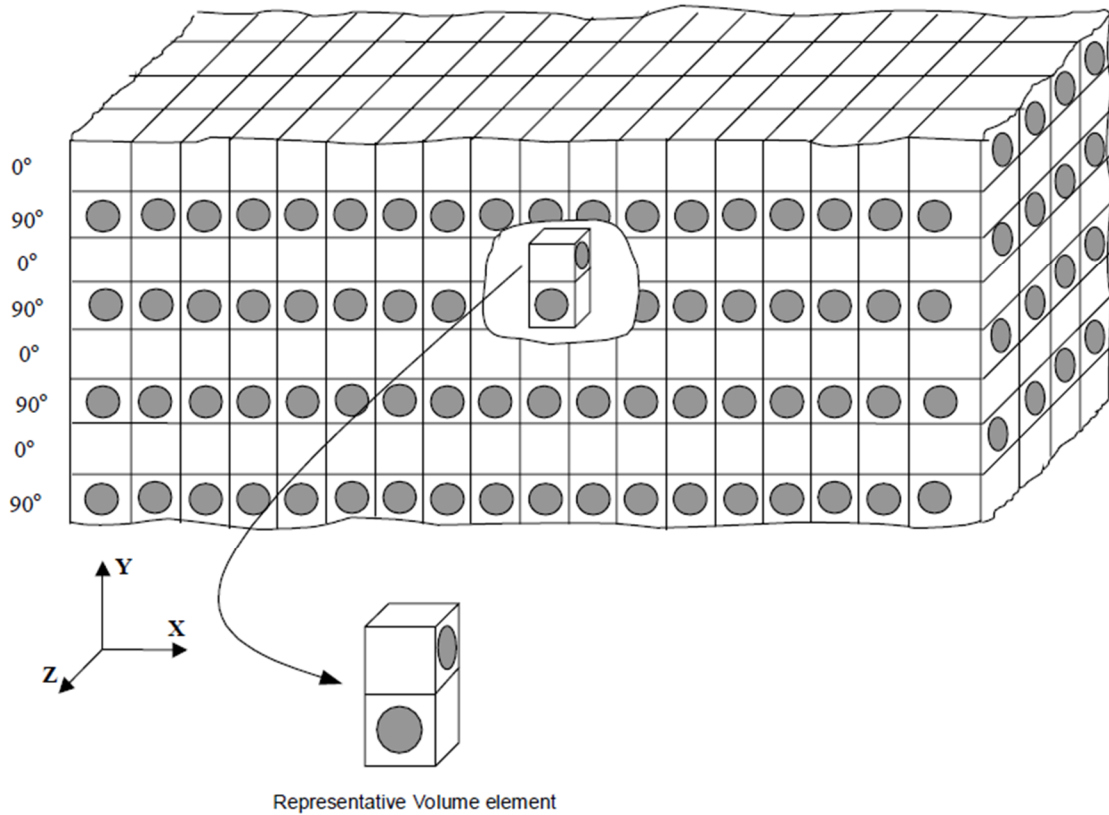


Figure 2.19 Multi-layer representative volume element (Ellyin et al., 2003)

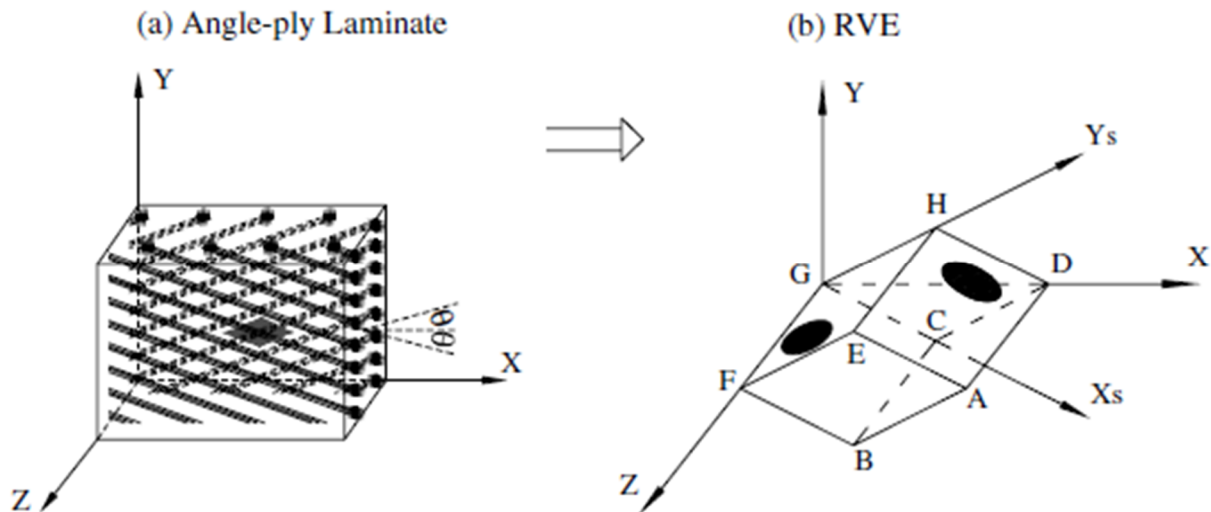


Figure 2.20 A representative volume element for an $[\pm 45]$ angle-ply laminate (Xia et al., 2003)
 All elastic moduli for the angle-ply laminates were predicted by performing numerical simulation using proposed RVE shape subjected to periodic boundary conditions. The predicted results were in good agreement with the results available in the literature and results predicted by

using laminate theory as shown in Fig. 2.21. It was further stated that the proposed methodology can be applied to nonlinear micromechanical analysis of the composites under multi-axial loads. However, all the derived equations in this work were based on small deformation theory.

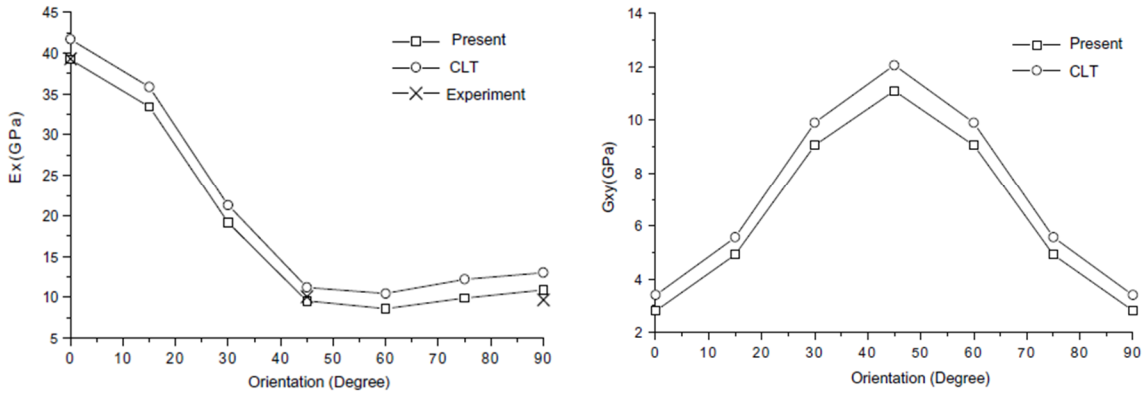


Figure 2.21 Comparison of results predicted by classic laminate theory and numerical simulations (Xia et al., 2003)

The use of a single fiber in a unit cube neglects the effect of fiber-to-fiber interaction within a lamina. A similar model was used for micromechanical characterization of an angle-ply fibrous composite by Abolfathi et al. (2008). The multi-layer single fiber approach was also used for micromechanical modeling of damage propagation in titanium based metal-matrix composites by Sherwood (1995). Zanfa et al. (2005) used the model proposed by Xia et al. (2003) to predict damage progression in glass fiber/ epoxy cross-ply laminates by finite element analysis. In another study, Ellyin et al. (2003) used a multi-layer single fiber RVE, using visco-elastic micromechanical model for modeling matrix, to capture free edge and time effects in glass fiber/epoxy cross-ply laminates. The proposed micromechanical model provided local stress-strain near the edge surface. This local stress-strain was used along with the damage criteria to investigate damage evolution in composite. It was found that the early damage initiation on the free edge surface has a negligible effect on the macro material response.

Xia et al. (2000) proposed a 3D multi-cell meso/micro-mechanical model for the prediction of the overall mechanical behavior of a $[0,90_3,0]_T$ as shown in Fig. 2.22. In this model the periodic condition is assumed only in the in-plane directions. It was assumed that no periodicity exists in the thickness direction. Single fiber is modeled to represent the entire volume fraction of the reinforcement. The epoxy matrix was modeled as a non-linear visco-elastic material through the

user-subroutine. It was found that numerical results global material response as well as damage response from the finite-element analysis is in good agreement with experimental data.

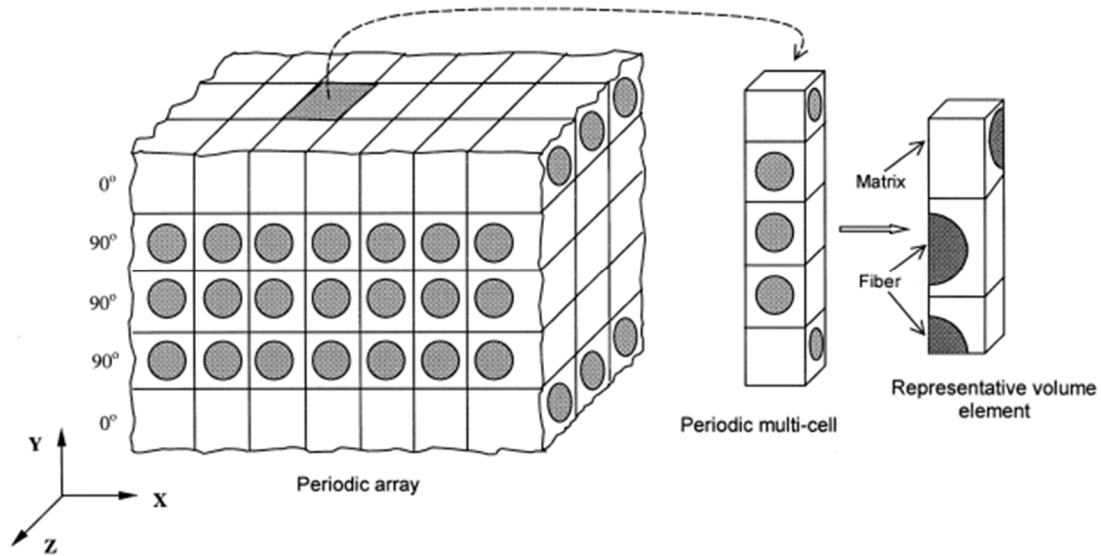


Figure 2.22 Representative volume element for $[0/90_3/0]_T$ laminate (Xia et al., 2000)

Due to the periodicity in the XZ plane, a representative volume element consists of two cells with 0° fiber and three cells with 90° fiber orientation. This representative structure was treated as a building block of the laminate, as shown in Fig. 2.22. It can be noted that the same RVE can be used if the number of each layer in the laminate is doubled, i.e., $[0_2,90_6,0_2]_T = [0_2,90_3]_S$, provided the volume fraction for each layer is same.

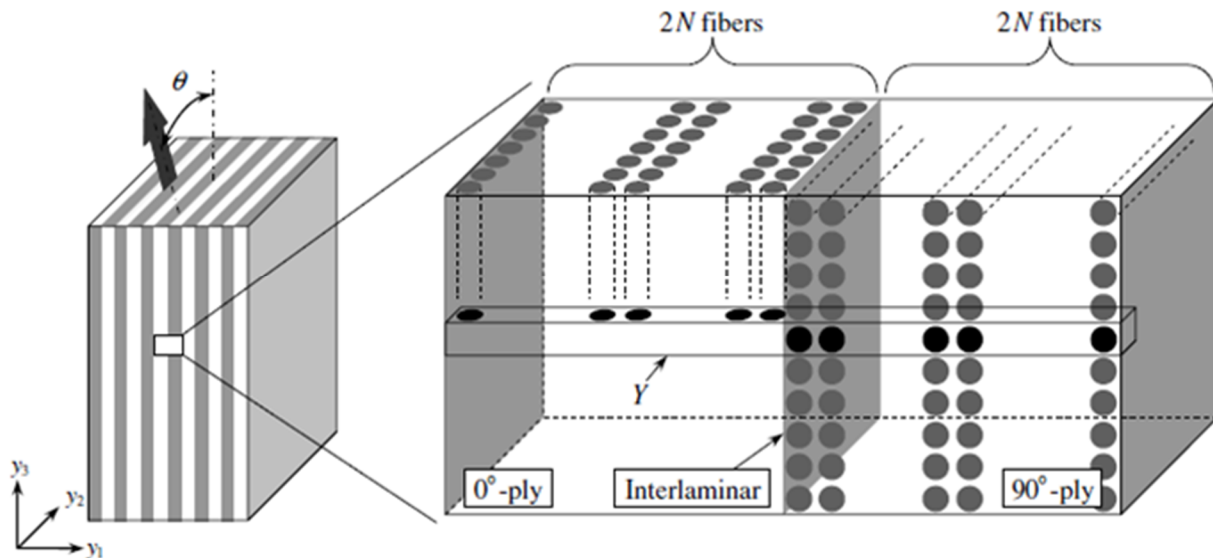


Figure 2.23 Multi-fiber multi-layer unit cell with orderly arranged fibers (Matsuda et al., 2007)

A multi-layer multi-fiber unit cell having an orderly distribution of fibers was proposed by Matsuda et al. (2007) to predict the inter-laminar stress distribution under the assumption that each lamina in the laminate as shown in Fig.2.23. The model is used for predicting microscopic interactions between unidirectional long fiber-reinforced laminae subjected to in-plane uniaxial tension and 45° off-axis loading. A unit cell proposed includes inter-ply area. Point symmetry was utilized, and only half of the unit cell was modeled (Ohno et al., 2001). To reduce the computational cost further sub-structuring method was utilized (Zienkiewicz and Taylor, 2000). It was observed that relatively high microscopic shear stress occurs prominently at the interface between the 0° and 90°plies. It was further shown that the microscopic interaction between the two plies was observed only in the vicinity of the interface. The main outcome of the study was that it is necessary to consider the microscopic structure consisting of fibers and matrix around the interface of laminae. The microscopic structure at a distance of more than a fiber diameter away from the interface may be replaced by the equivalent homogeneous material. The multi-fiber multi-layer RVEs reported in the literature do not take into account the random distribution of the fibers in the matrix. The damage initiation and propagation in the matrix and the interface have not been fully characterized.

2.3 Multilevel methods for non-periodic media

It is known that the material failure often occurs due to stress concentration. The M^2 RVE approach introduced in Chapter 1 is not suitable to determine micro-stresses distribution in the areas involving stress concentration, e.g., free-edges, interfaces etc., as the periodic boundary conditions are no longer applicable. To determine the severity of the stress concentration and possible failure consequences, it is important to investigate the micro-stress distribution in the area involving stress concentration. However, a full-field micro-stress analysis would require a huge amount of computational efforts. In fact, it is unrealistic to perform full micro-stress analysis for structural design. Therefore, homogenization approach is widely used for the engineering analysis of composites as composite microstructure is usually much smaller than the material domain used for the analysis. The composite is considered as a continuum with effective properties. Local stresses are predicted using effective stresses obtained using continuum mechanics. However, it is important to describe failure mechanism as microscale, specially, in

the stress concentration area. There is a need to determine different approach to estimate micro-stresses in the stress concentration areas. Multi-level method proposed by Wang and Yan (2001) is one of the most common methods to determine the micro-stresses in the stress concentration regions of composite structures. In a two-level macro-micro approach proposed by them, the effective properties derived from the laminate theories are utilized to predict the effective (macroscopic) stress and effective (macroscopic) displacement fields. Subsequently, the area of interest (stress concentration area), is modeled at microscale i.e. with actual fibers, matrix and interface. Macro-stresses and/or macro-displacements are used along the microscale domain as boundary condition.

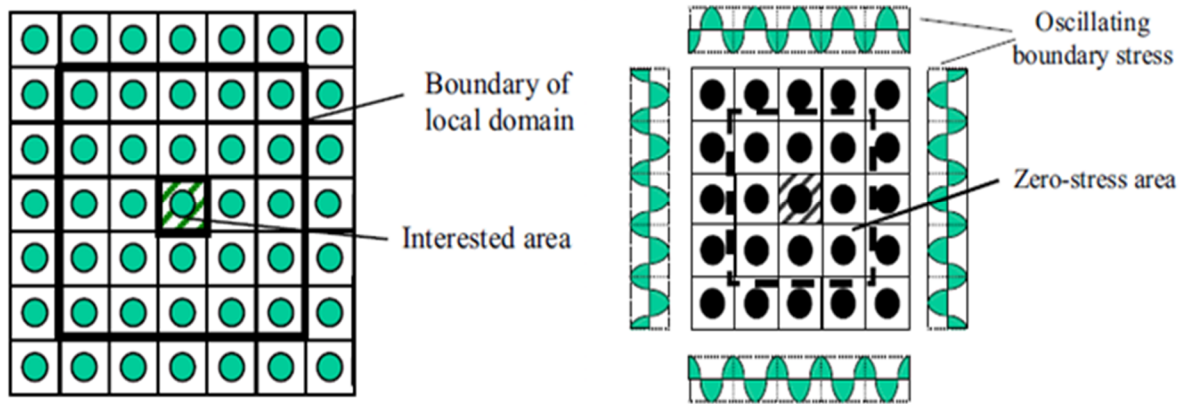


Figure 2.24 Schematic of macro-micro analysis (Wang and Yan, 2001)

It was demonstrated that if there is no severe stress concentration along the boundary of the local domain, the resultant force of the effective boundary stress is same that of the micro stress along the external edge of each cell on the boundary of the local domain as shown in Fig. 2.24. It was assume that oscillating boundary stress affect only at the vicinity of the boundary. Stress reduces as distance increases from the boundary. Stress vanishes in the area far from the boundary. It was found that if the area of interest is in the zero-stress zone, the micro-stress in the area of interest matches with full-field micro-stress analysis. Wang and Yan (2001) found out that there are two prerequisites to ensure micro-stresses obtained from the macro-micro analysis are in agreement with the full microscale analysis. The first condition is that there shouldn't be severe effective stress concentration along the boundary of the selected microscale area. The second requirement is that the boundary of the microscale domain must be far from the area of the interest. Wang and Yan (2001) proposed "local domain test", which states that, if the stress in the area of the

interest is very small, the domain selected for microscale modeling in two-level analysis is sufficient as shown in Fig 2.24. It was shown that micro-stresses in the area of interest obtained from two-level analysis are in good agreement with the micro-stresses obtained from full microscale analysis.

Wang and Yan (2004) proposed an inter-scale theory for the onset of matrix-dominated tensile failures in unidirectional and multi-directional laminates loaded globally. The proposed model is an extension of the idea proposed earlier by the same author (Wang and Yan, 2001). The theory is formulated at the fiber and matrix scale where the micro field is recovered from the macro-field of the laminate. The proposed model predicts critical global load at the onset of matrix cracking, at the laminate scale. Fig. 2.25 shows schematic of inter-scale theory.

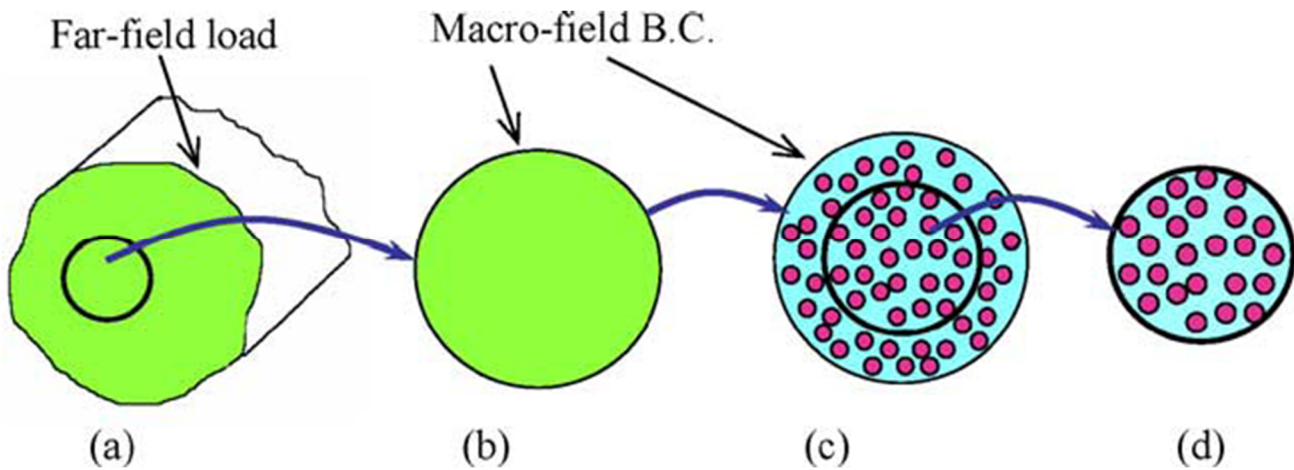


Figure 2.25 (a) A body of homogenized UD composite under load; (b) isolated critical element; (c) critical element with microstructure restored; (d) the isolated interior element (Wang and Yan, 2004)

Markovic and Ibrahimbegovic (2004) proposed a two-scale computational strategy for modeling the inelastic behavior of heterogeneous materials. Finite element method was applied to the structural scale as well as on the micro scale. The special care was taken in handling the interface condition between microscale and macroscale. The proposed approach is based on the localized Lagrange multiplier method. Parametric study was performed to study influence of the boundary conditions, of microscale. The model is suitable where the assumptions of completely separated and decoupled scales are not justified. In such problems, the heterogeneities on the micro scale are bigger with respect to the macro scale dimensions and where its typical length would affect the macroscale response of the structure, the phenomenon being usually called the ‘scale effect’.

Consequently, the hierarchical approach has to be replaced by a strongly coupled multiscale model, where sophisticated modeling methods are used at all the relevant scales. Fig 2.26 shows macro domain FE mesh connected to the micro domain mesh by Lagrangian multiplier λ .

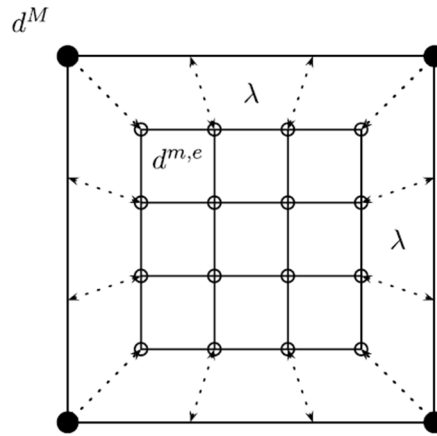


Figure 2.26 Macro domain FE mesh connected to the micro domain mesh by Lagrangian multiplier λ (Markovic and Ibrahimbegovic, 2004)

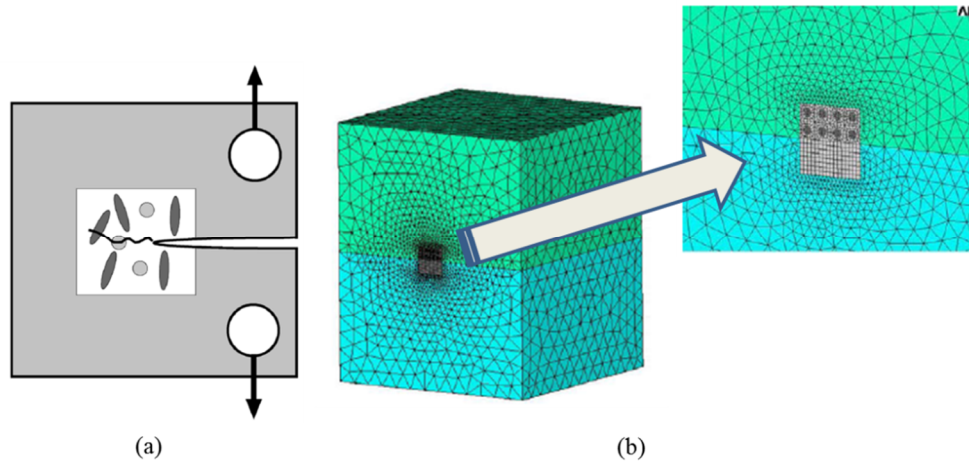


Figure 2.27 (a) Embedded cell approach(Gonzalez and Llorca, 2006) (b) Partial homogenization (Borokov and Sabadash, 2002)

Gonzalez and Llorca (2006) simulated the fracture behavior of a notched fiber-reinforced composite sample under tension, where the fibers were aligned in the direction of loading and perpendicular to the notch. Their method was based on an embedded cell approach as shown in Fig.2.27(a). In front of the notch tip, where the damage is concentrated, actual fiber/matrix topology was modeled while the rest of the beam was represented by a transversally isotropic homogeneous solid. Plastic deformation of matrix, brittle fiber fracture and fiber/matrix

frictional sliding was explicitly modeled. The simulation results and experimental response was in good agreement, demonstrating the potential of this approach to simulate the complex fracture behavior at both microscopic as well as macroscopic level. Borokov and Sabadash (2002) have proposed a partial homogenization approach for obtaining micro-stresses in the region of interest. They proposed an approach in which the microscale and macroscale are coupled as a single domain and analyzed simultaneously as shown in Fig.2.27 (b).

It can be concluded from the literature survey that multi-level modeling technique can be used to find micro-stresses in the region having stress concentration (periodicity is not applicable). But, multi-level methods available in the literature are fully coupled methods and are computationally very expensive. Multi-level method uses transition elements (like FE^2), which are difficult to implement in 3D problem. Micro-macro two-level is computationally less expensive, if proper care is taken in selection of size microscale domain (local domain test) as described by Wang and Yan (2001). Details of the work done using macro-micro approach have been presented in chapter 5 of this thesis.

2.4 Summary

In this chapter a detailed literature survey has been carried out on multiscale modeling. Recent works in the area of estimating damage response using multiscale method via micro-mechanics based methods have been reviewed. A comprehensive micromechanics approach which captures all the modes of failure along with delamination has yet to be developed. A multi-fiber multi-layer representative volume element will be useful to capture all the modes of phase and interface damage, viz., matrix damage, fiber-matrix decohesion, delamination and fiber failure. Furthermore, it has been observed that the assumption of global and local periodicity is not suitable for regions, such as free edges, interfaces, macro-cracks, neighborhood of material discontinuities and most importantly in the regions of evolving microscopic damage. Therefore, there is need for modeling damage in the structure without use of periodicity assumption. There are many multi-level methods available, e.g., FE^2 method, multi-level hierarchical method to address the issue of localized damage. However, micro-macro two-level approach is computationally least expensive, if proper case is taken in selection of size of microscale domain. The next few chapters address these two issues in detail.

Chapter 3: Damage analysis in in-plane shear via multi-fiber multi-layer representative volume element (M^2RVE)

3.1 Introduction

In the present work, a randomly distributed multi-fiber multi-layer representative volume element (M^2RVE) has been proposed to capture all likely inter-laminar and intra-laminar damage mechanisms, namely, fiber breakage, fiber-matrix debonding, and matrix cracking. It is a better geometrical representation of the lamina as compared to an equivalent single fiber multi-layer RVE suggested by Xia et al. (2003) and orderly distribution of fibers suggested by Matsuda et al. (2007). In this model, the effects of geometry and spatial distribution of the fibers on the onset and propagation of the matrix damage and fiber-matrix debonding can be captured explicitly, which is not possible with either multi-fiber single layer RVEs or with single fiber multi-layer RVEs.

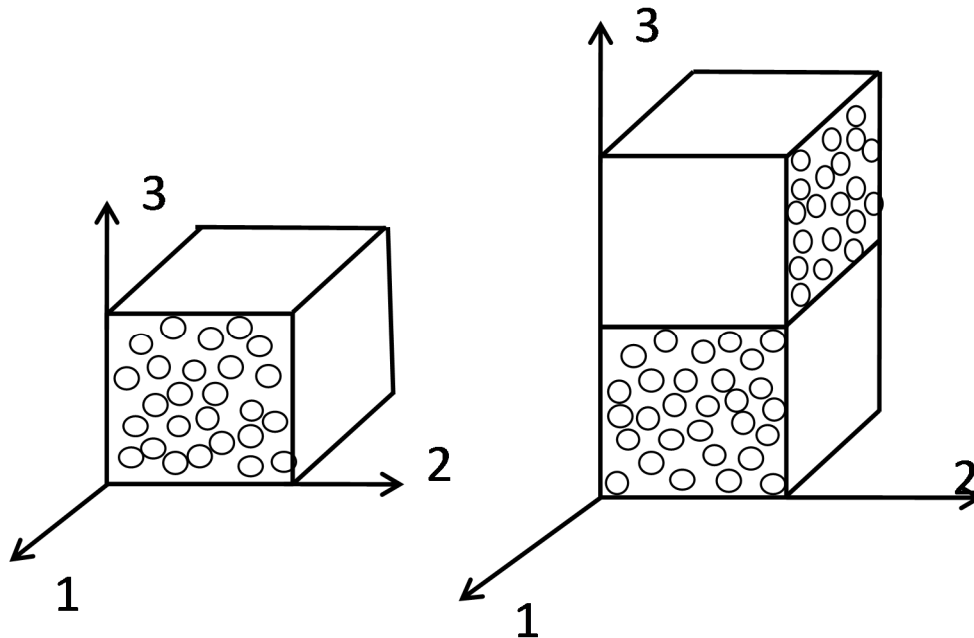


Figure 3.1 Typical RVE and M^2RVE

Fig.3.1, shows a typical M^2RVE for $[0/90]_n$ laminate used in the present study via finite element analysis. The proposed M^2RVE captures the effects of matrix and fiber-matrix interface failures

via Mohr-Coulomb criterion and surface based cohesive zone, respectively. It is known that the in-plane shear loading is one of the most complex deformation modes due to significant non-linear deformations before failure. Therefore, in-plane shear loading has been used to validate the proposed model. In-plane shear experiments were carried out according to ASTM D7078 (ASTM D7078/D7078M–05, 2000) to validate the proposed model. The model is then used to predict the global as well as local material response, including damage. This is followed by the effect of Mohr-coulomb matrix friction angle and fiber-matrix interfacial strength on the global material response, which has been captured. Finally, interface damage initiation and evolution has been fully characterized.

3.2 Finite element modeling of M^2RVE for cross-ply laminate

3.2.1 Generation of the geometrical and FE model

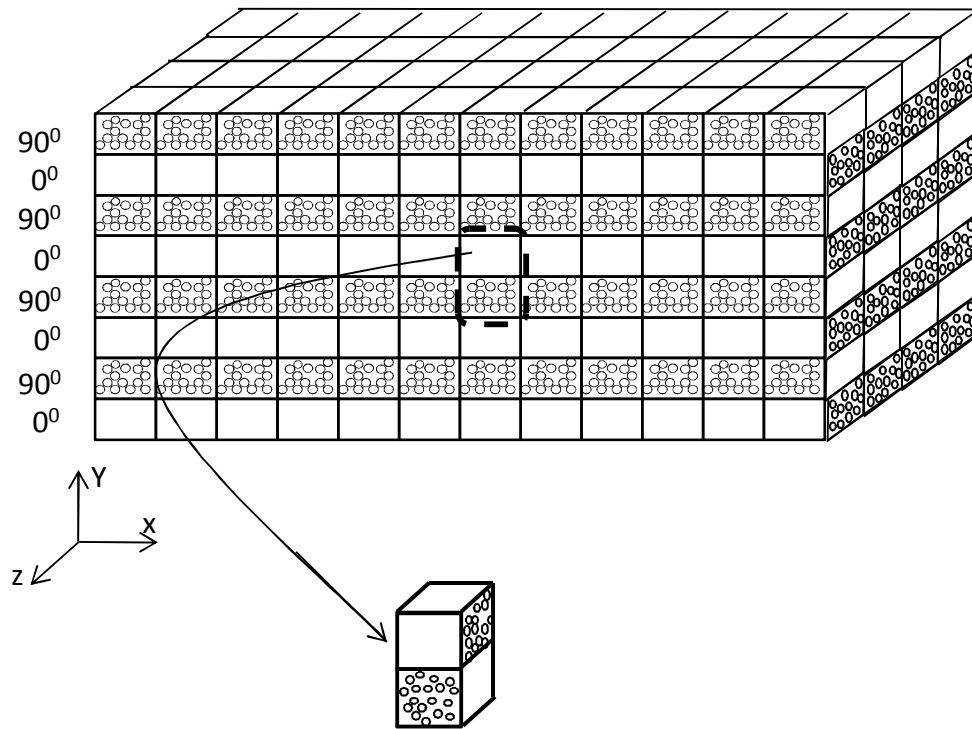


Figure 3.2 M^2RVE for $[0/90]_n$ laminate

Fig.3.2, shows a typical configuration of $[0/90]_n$ laminate which has been modeled using the M^2RVE . The same M^2RVE can be used to model $[0/90]_n$ laminate (‘n’ number of plies) due to the application of periodic boundary conditions to all the faces of the M^2RVE . Finite element analysis via the M^2RVE has been performed to understand the behavior of the $[0/90]_n$ and $[\pm 45]_n$

laminates. The geometries of $[0/90]_n$ and $[\pm 45]_n$ M^2RVE have been shown in Fig.3.3. M^2RVE consists of two cubes that have multiple randomly distributed fibers of identical diameter. The cubes have been placed at 90° to each other, and shear loading has been applied on the right face of the M^2RVE . A random distribution of circular fibers, $24\ \mu\text{m}$ in diameter, have been generated using a fiber randomization algorithm in DIGIMAT FE[®](2010). Each generated fiber has been accepted, if the distance between neighboring fiber surfaces was more than $1\ \mu\text{m}$ to ensure adequate discretization of that region. The distance between the fiber surface and the M^2RVE edges has been kept at more than $0.5\ \mu\text{m}$ to avoid distorted finite elements during meshing. It has been assumed that the laminate microstructure has had indefinite translation along the 1, 2 and 3 axes; thus, fiber positions within the M^2RVE have maintained periodicity. Fibers intersecting the edges have been split into two parts and copied to the opposite sides to create a periodic microstructure, shown in Fig.3.3. New fibers have been added until the desired 28% fiber volume fraction has been reached. The M^2RVE (matrix and fibers) have been meshed using modified quadratic 10-node tetrahedral (C3D10M) elements in ABAQUS Standard[®](2007).The element type has an additional internal node, which increases the accuracy to reproduce the strain gradient in the matrix between closely packed fibers. The FE mesh contains 15491 nodes and 54122 elements, shown in Fig.3.4 (a). Sensitivity analysis to determine the size of the M^2RVE has been performed in the subsequent section.

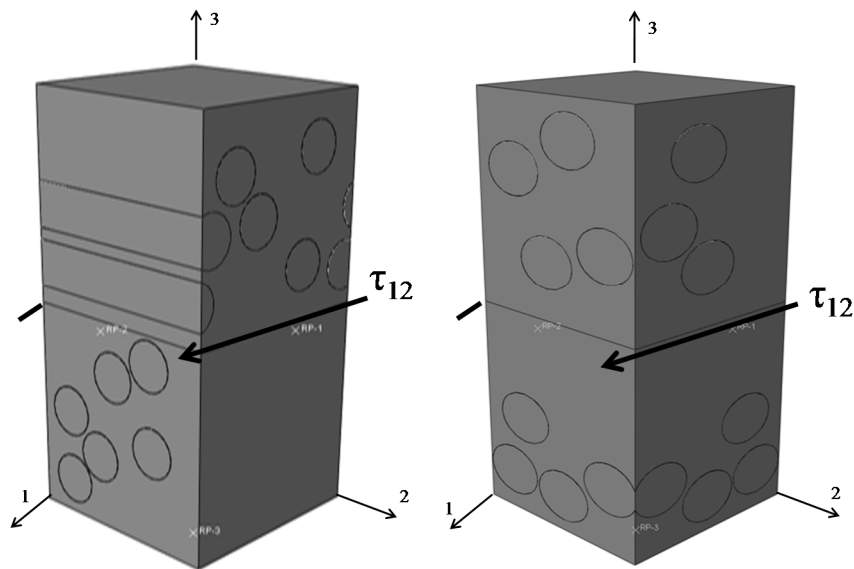


Figure 3.3 Schematic of the M^2RVE of the $[0/90]_n$ and $[\pm 45]_n$ laminate microstructure subjected to the in-plane shear loading

3.2.2 Boundary and loading conditions

As has been mentioned previously, the M^2RVE is a representative unit for the cross-ply laminate, shown in Fig.3.2. Therefore, the periodic boundary conditions have been applied on all the faces of the M^2RVE to maintain continuity between neighboring M^2RVE . Periodicity implies that each M^2RVE in the composite has the same deformation mode and there is no separation or overlap between the neighboring M^2RVE s. Perfect bonding has been assumed between the plies for all the simulations performed for in-plane shear loading.

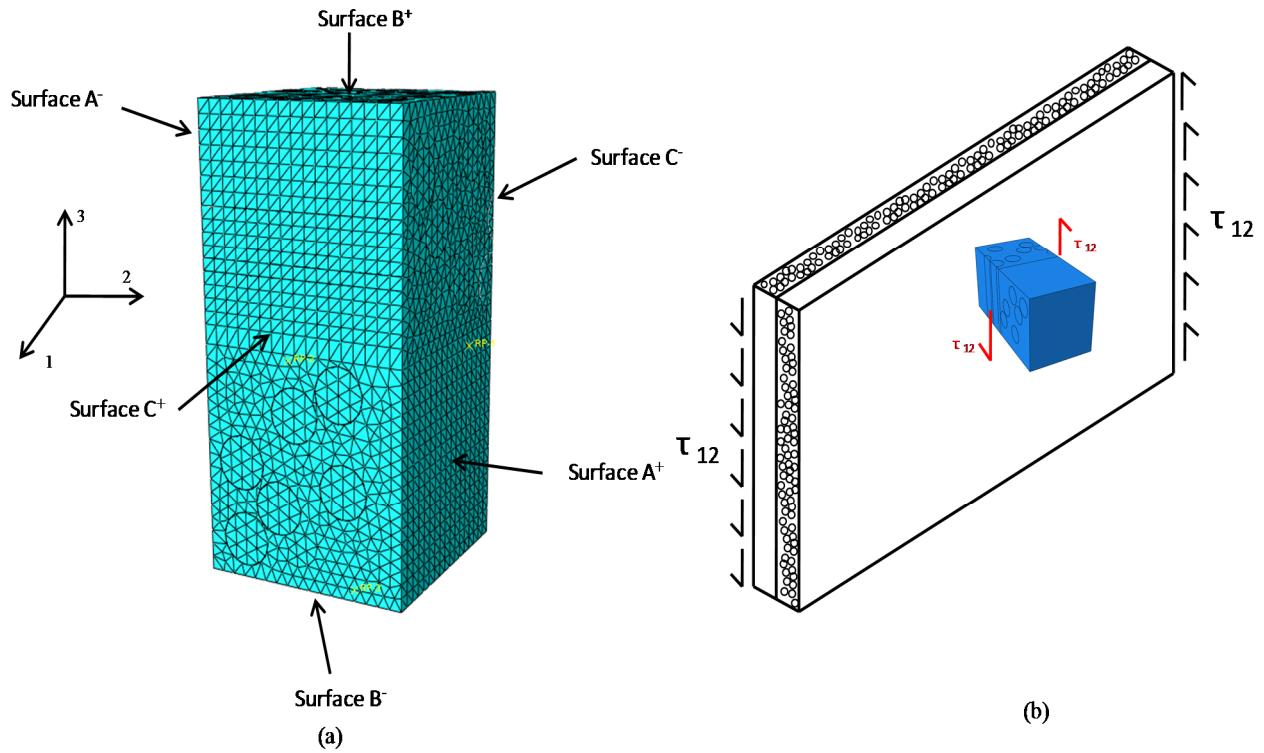


Figure 3.4 (a) Schematic of the meshed M^2RVE used for implementation of periodic boundary conditions.(b) In-plane shear loading using M^2RVE

The periodic boundary condition applied on the proposed M^2RVE has been shown in Fig.3.4 (a).

Eq.(3.1), shows the displacement ' u_i ' as a function of applied global loads as

$$u_i = \varepsilon_{ij}x_j + v_i \quad (3.1)$$

Where ε_{ij} is the average strain and v_i is the periodic part of the displacement components, u_i , on the boundary surfaces (local fluctuation). The indices i and j denote the global three-dimensional coordinate directions 1, 2, and 3. An explicit form of periodic boundary conditions suitable for

the proposed M²RVE model has been derived from the general expression mentioned above. For the M²RVE shown in Fig.3.4 (a), the displacements, u_i , on a pair of opposite boundary surfaces (with their normal along x_j direction) are:

$$u_i^{K^+} = \varepsilon_{ij}x_j^{K^+} + v_i^{K^+} \quad (3.2)$$

$$u_i^{K^-} = \varepsilon_{ij}x_j^{K^-} + v_i^{K^-} \quad (3.3)$$

where ‘ K^+ ’ means displacement along the positive x_j direction and ‘ K^- ’ means displacement along the negative x_j direction on the corresponding surfaces A^-/A^+ , B^-/B^+ , and C^-/C^+ (see Fig.3.4 (a)). The local fluctuations $v_i^{K^+}$ and $v_i^{K^-}$ around the average macroscopic value are identical on two opposing faces due to the periodic condition. Hence, the difference between the above two equations are the applied macroscopic strain condition, given by:

$$u_i^{K^+} - u_i^{K^-} = \varepsilon_{ij}(x_j^{K^+} - x_j^{K^-}) \quad (3.4)$$

The non-homogeneous stress and strain fields obtained have been reduced to a volume-averaged stress and strain by using Gauss theorem in conjunction with the Hill-Mandal strain energy equivalence principle proposed by Hill (1963). Finally, the elastic modulus has been obtained as the ratio of the average stress to the average strain. The average stresses and strains in the M²RVE have been calculated as described in Gibson (2007), Sun and Vaidya (1996):

$$S_{ij} = \frac{1}{V} \int_v s_{ij} dV \quad (3.5)$$

$$E_{ij} = \frac{1}{V} \int_v e_{ij} dV \quad (3.6)$$

Where V is the volume of the periodic representative volume element, S_{ij} and E_{ij} are average stresses and average strains in the M²RVE, respectively. s_{ij} and e_{ij} represent local stresses and strains over an elemental volume ‘ v ’, respectively.

Fig.3.4 (b) shows the in-plane shear loading on the proposed M²RVE model. The perturbation has been introduced to the system of equation used for implementation of periodic boundary conditions through a dummy node which has acted as a load carrier. Nodes on the face are attached to a dummy node and load transfer on the face has been applied through that dummy node. The material response of the M²RVE has been used with periodic homogenization to predict the global response of the structure.

3.2.3 Material Properties

E-glass (ER-459L) fibers were modeled as linear elastic isotropic solids and their constants have been given in Table 3.1 (provided by the supplier). The epoxy matrix (EPOFINE-556) with FINEHARD-951 hardener has been assumed to behave as an isotropic, elastic-plastic material and its elastic constants have also been provided in Table 3.1.

Table 3.1 Elastic properties of matrix and fibers

Constituent materials	Elastic modulus, E (GPa)	Shear modulus, G (GPa)	Poisson's ratio, ν
E-glass fibers, ER-469L	73	29.67	0.23
Epoxy resin, EPOFINE-556 (FINEHARD-951 hardener)	4.7	1.8	0.30

3.2.4 Failure criteria

During the damage process of the laminates in shear, matrix cracking (transverse cracking) is the first damage phenomenon to take place since the matrix has the lowest stress to failure of all the composite constituents as described in Gibson et al. (2007). Therefore, for the $[0/90]_n$ laminate and $[\pm 45]_n$ laminate, the considered dominant damage mode has been matrix transverse cracking followed by fiber-matrix debonding.

Although the M^2RVE model discussed here has been subjected to uniform in-plane shear loading, a tri-axial stress state exists in the individual elements of the model. Consequently, the Mohr–Coulomb multi-axial damage criterion has been used to model the matrix damage, shown in Fig.3.5. The Mohr-Coulomb criterion described in Jiang and Xie (2011) assumes that yielding takes place when the shear stress, τ , acting on a specific plane reaches a critical value which is a function of the normal stress, σ_n , acting on that plane; thus, the influence of the triaxiality on the shear yielding was taken into account as indicated in Eq.(3.7).

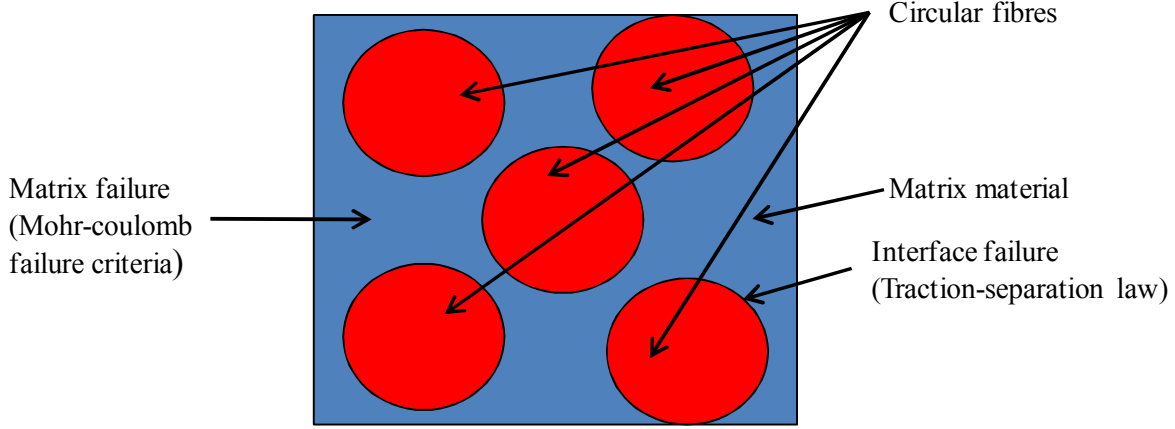


Figure 3.5 Schematic representation of the failure criterion used for matrix and fiber-matrix debonding

The yield surface corresponding to the failure criterion described, written in terms of the maximum and minimum principal stresses (σ_I and σ_{III}), has been given by Eq. (3.8).

$$|\tau| = c - \sigma_n \tan \varphi \quad (3.7)$$

$$F(\sigma_I, \sigma_{III}) = (\sigma_I - \sigma_{III}) + (\sigma_I + \sigma_{III}) \sin \varphi - 2c \cos \varphi = 0 \quad (3.8)$$

where c and φ stand for the matrix cohesion and the matrix friction angle, respectively. These two material parameters control the plastic behavior of the matrix. Physically, the cohesion ‘ c ’ represents the yield stress of the matrix under pure shear while the friction angle takes into account the effect of the hydrostatic stresses. It has been assumed that both constants have been independent of the accumulated plastic strain. The directions of plastic flow in the stress space have been determined using a non-associative flow rule, as has been explained by Jiang and Xie (2011). The value of both parameters for an epoxy matrix have been found using Eq. (3.9) which has been described by González and LLorca (2007)

$$\sigma_{mt} = 2c \frac{\cos \varphi}{1 + \sin \varphi} \text{ and } \sigma_{mc} = 2c \frac{\cos \varphi}{1 - \sin \varphi} \quad (3.9)$$

The experimental matrix tensile and compressive strengths, σ_{mt} , and σ_{mc} , have been equal to 75 MPa and 105 MPa, respectively. The value of friction angle has been found to be 10° which is within the range determined by González and Llorca (2007), and Puck and Schürmann (1998). The value of cohesion ‘ c ’ has been computed as 44.7 MPa using Eq. (3.9) and has been used subsequently for all the simulations that have corresponded to friction angle of 10° . This is

a reasonable value for ‘ c ’. Experiments were conducted to determine in-plane shear strength of the isotropic neat epoxy resin which was found to around $\sim 40\text{MPa}$.

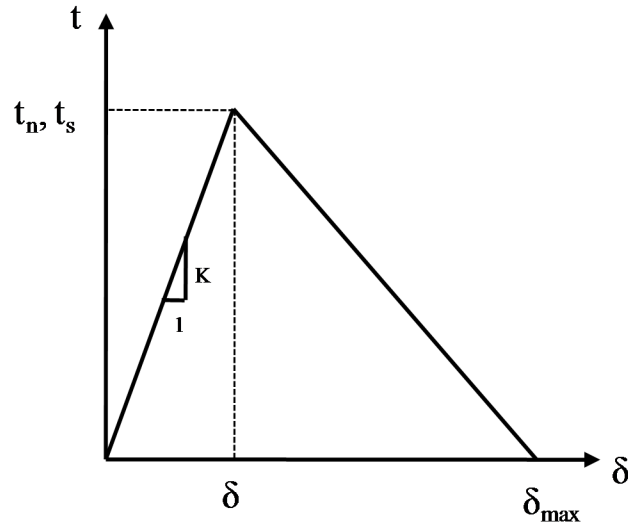


Figure 3.6 Standard traction-separation law

The fiber-matrix interfacial decohesion has been simulated using standard cohesive surface elements in ABAQUS Standard[®]. The mechanical behavior of the interface has been simulated using a traction-separation law which relates the displacement across the interface to the force vector acting on it. In the absence of any damage, the interface behavior has been assumed to be linear with a high value of an initial stiffness, K (35 GPa) to ensure the displacement continuity at the interface. The linear behavior ends at the onset of damage, using a maximum stress criterion which has been expressed as:

$$\max \left\{ \frac{\langle t_n \rangle}{N}, \frac{t_s}{S} \right\} = 1 \quad (3.10)$$

Where t_n and t_s are normal and tangential stresses transferred by the interface, respectively. t_n is positive or zero otherwise, because compressive normal stresses do not cause opening of the crack. N and S are the normal and tangential interfacial strengths, and have been assumed to be equal for simplicity. It is a suitable assumption for in-plane shear loading wherein normal strength is not expected to dominate interfacial damage.

Fracture energy, \dot{I} , is another parameter which controls the interface behavior other than cohesive strength (N, S). Fracture energy, \dot{I} , is the area under the curve shown in Fig.3.6. The

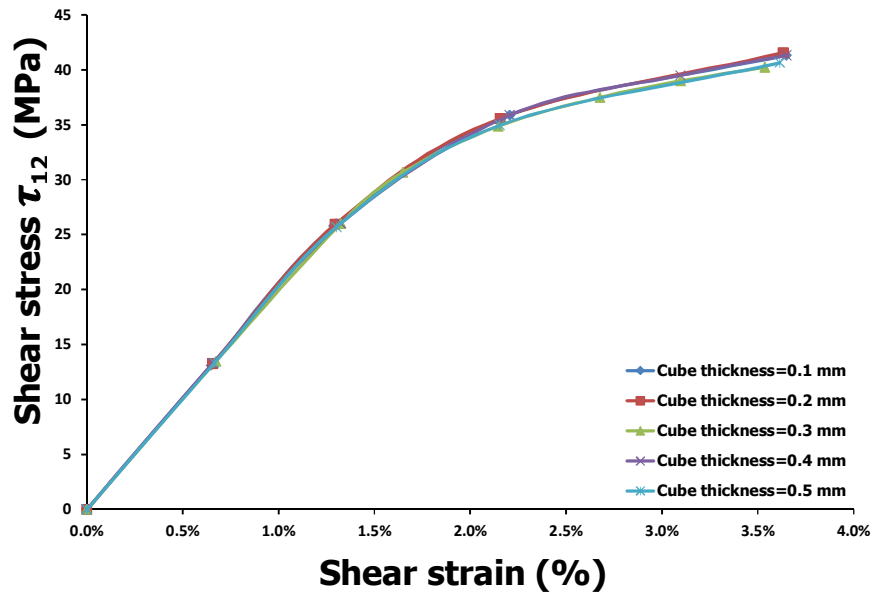
interface failure model assumes that the energy consumed during the fracture of the interface is independent of the loading path. Fracture energy, Γ has been described as

$$\Gamma = \frac{1}{2} \times t \times \delta \quad (3.11)$$

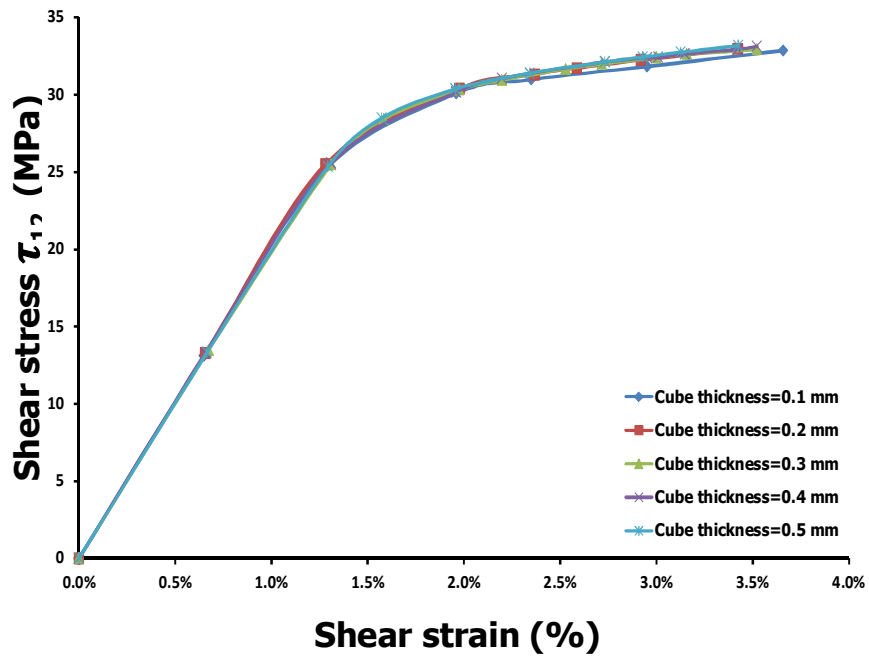
Where t (t_n or t_s) is the cohesive strength of the interface and ' δ ' is the displacement (tangential or normal) across the interface. The energy necessary to completely break the interface is kept equal to $\Gamma = 100 \text{ J/m}^2$ for all the simulations a reasonable value for glass fiber/epoxy matrix composite laminate as has been reported via push out tests by Zhou et al. (2001).

3.3 Sensitivity analysis for the size of M²RVE

One of the important issues in the simulations was the selection of the size of each cube in the M²RVE. Each cube should contain all the necessary information for the statistical description of the microstructure and its size should be large enough so that the average properties are independent of its size and position within the material. The critical size of the M²RVE depends on the phase, interface properties and spatial distribution, and no estimates have been available in the literature. Therefore, a parametric study has been performed to determine the size of each cube in M²RVE. Initially, the thickness of each cube has been considered to be 0.5 mm. Eventually, the thickness of the cubes has been reduced, and average stress-strain response has been plotted, shown in Fig.3.7. Two different values of interface strength 30 MPa and 10 MPa have been considered for the analysis to ensure that the size of the M²RVE would be sufficiently large and the periodic boundary conditions would not lead to erroneous results. The stiffness of the interface has been assumed to be very high (35 GPa/mm) in order to ensure displacement continuity between the fiber and matrix as suggested by Totry et al., 2010. The friction angle and matrix cohesive strength have been 10° and 44.7 MPa, respectively, for all the simulation runs. It can be clearly seen that the effect of the cube dimensions of the M²RVE is not appreciable on the global stress strain response in both the cases. Consequently, a thickness of 0.1 mm has been selected to perform all the subsequent simulations. Only six fibers per cube have been required for the model as opposed to approximately 155 fibers per cube in the case of a 0.5 mm thickness of the each cube. Due to the reduced thickness, computational efficiency of the model has been significantly improved while maintaining the same global response.



(a)



(b)

Figure 3.7 In-plane shear stress strain response for various thicknesses of the cubes in M^2RVE (a) Interfacial strength = 30 MPa; (b) Interfacial strength = 10 MPa

It can be observed in Fig.3.7 that the global in-plane shear stress-strain response of the cross-ply laminate has been relatively insensitive to the thickness variation of the cube for cohesive strength of 30 MPa and 10 MPa. However, the 3D stress state exists in all the elements of the model; thus the effect of the cube size on the normal stresses developed in all directions other than thickness has been also studied. Table 3.2 shows the effect of the different edge size of the cube on the volume-averaged normal stresses developed in M²RVE for the same loading. It has been observed that the volume averaged normal stresses are very low (<3 MPa) for σ_{11} and of the order of 10^{-4} for the other two components, shown in Table 3.2; consequently, it can be construed that the laminate remains in pure shear even if the edge size is increased.

Table3.2 Effect of edge of the cube on normal stresses

Edge of the cube (mm)	σ_{11} (MPa)	σ_{22} (MPa)	σ_{33} (MPa)
0.1	2.38	8.9×10^{-4}	1.84×10^{-4}
0.2	2.36	5.10×10^{-4}	0.52×10^{-4}
0.3	2.33	5.18×10^{-4}	0.55×10^{-4}
0.4	2.28	1.22×10^{-4}	3.86×10^{-4}
0.5	2.31	4.66×10^{-4}	2.63×10^{-4}

3.4 Model validation

As no detailed experimental data has been available to validate the proposed model in the open literature, experiments have been performed on glass fiber/ epoxy laminate specimens. The proposed M²RVE model has been then validated against the experimental results.

3.4.1 Experimental work

[0/90] and [± 45] glass fiber/epoxy matrix laminates were manufactured using a hand lay-up technique. The fiber volume fraction (V_f) was determined experimentally, according to ASTM D2584 (ASTM D2584–11, 2000). The average value of fiber volume fraction was found to be 28%. The elastic properties of the constituent materials are provided in Table 3.1.

The edges of the laminate were removed and V-notched specimens ($76 \times 56 \text{ mm}^2$) were cut from the [0/90] laminate according to ASTM standard D7078 (D7078/D7078M–05, 2000) as

shown in Fig.3.8. The $[\pm 45]$ laminate was cut at an off axis angle of 45° from the $[0/90]$ laminate. Two strain gauges (gauge length of 6 mm) were mounted at the center of the specimen (between the notch tips) and oriented at $\pm 45^\circ$ to the edge of the specimen as shown in Fig.3.8. The difference between the readings of both the strain gauges provided the shear strain γ_{12} according to:

$$\gamma_{12} = |\varepsilon_{+45}| + |\varepsilon_{-45}| \quad (3.12)$$

where ε_{+45} and ε_{-45} stand for the normal strains provided by the strain gauges.

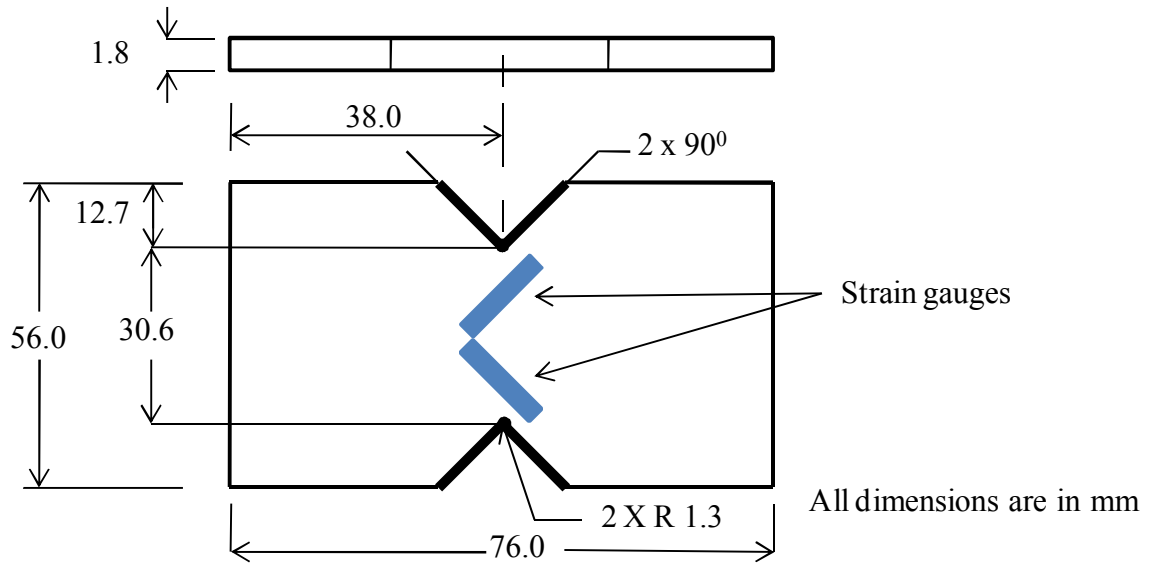


Figure 3.8 Specimen dimensions for the V-notched rail shear tests

3.4.2 Experimental Results

V-notch in-plane shear tests were carried out for the E-glass/epoxy $[0/90]$ and $[\pm 45]$ laminates, as per ASTM 7078 (ASTM D7078/D7078M–05, 2000). The specimens were tested in shear using an *LS 100 plus* universal testing machine by *LLOYD* instruments under stroke control and at a constant cross-head speed of 1mm/min as shown in Fig.3.9. The fixture used for test has been shown Fig.3.10. The applied load was measured simultaneously with a 100kN load cell. The corresponding shear strain, γ_{12} , was determined from Eq. (3.12), using strain gauges mounted on the specimen.

The load-displacement diagram for the $[0/90]$ laminate, up to a displacement of 2.5 mm has been plotted in Fig. 3.11 (a). The response becomes perfectly plastic at cross-head displacement of

1.5 mm. The final failure of the laminate takes place at 2500 N at a displacement of approximately 2.5 mm. Fig. 3.11(b) shows τ_{12} versus ϵ_{+45} and ϵ_{-45} of the test specimen.

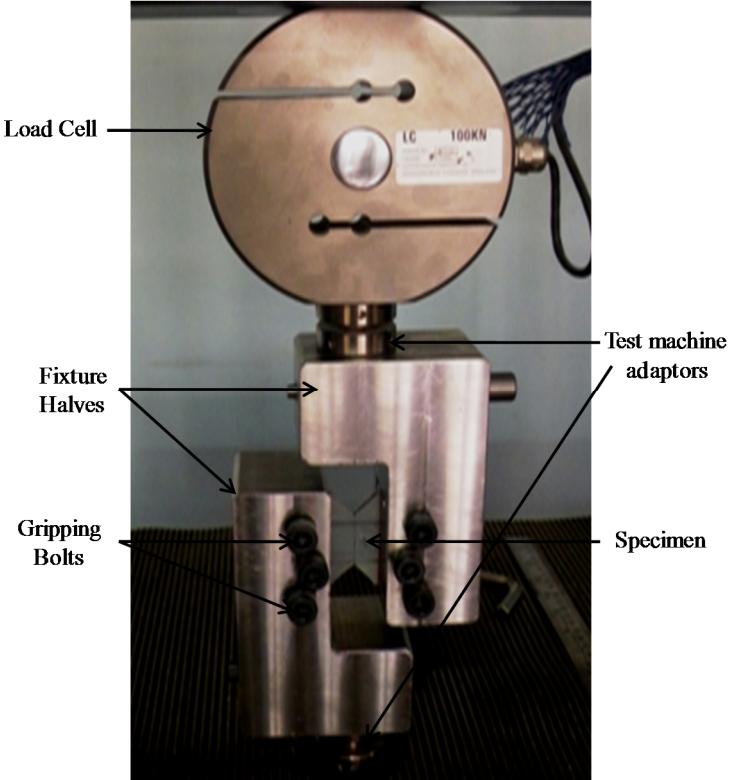


Figure 3.9 V-notched rail shear test fixture in action

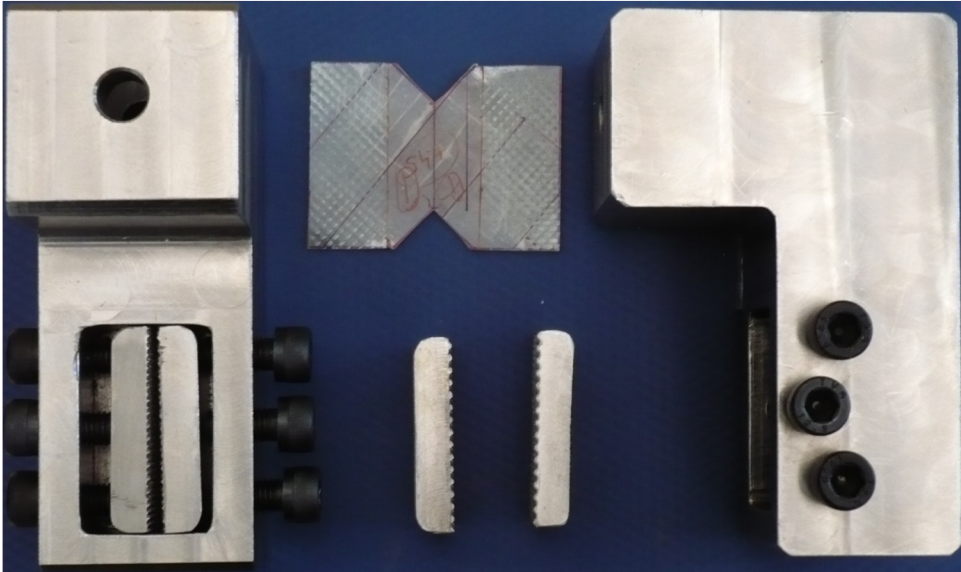


Figure 3.10 Fixture for V-notched rail shear test (ASTM 7078)

Figure 3.12 (a) shows the load-displacement curve for the $[\pm 45]$ laminate up to a displacement of 2.5 mm. The response becomes perfectly plastic at a load of approximately 5700 N and cross head displacement of 2.3 mm. Fig. 3.12 (b) shows a plot of τ_{12} versus ϵ_{+45} and ϵ_{-45} of this $[\pm 45]$ composite laminate specimen.

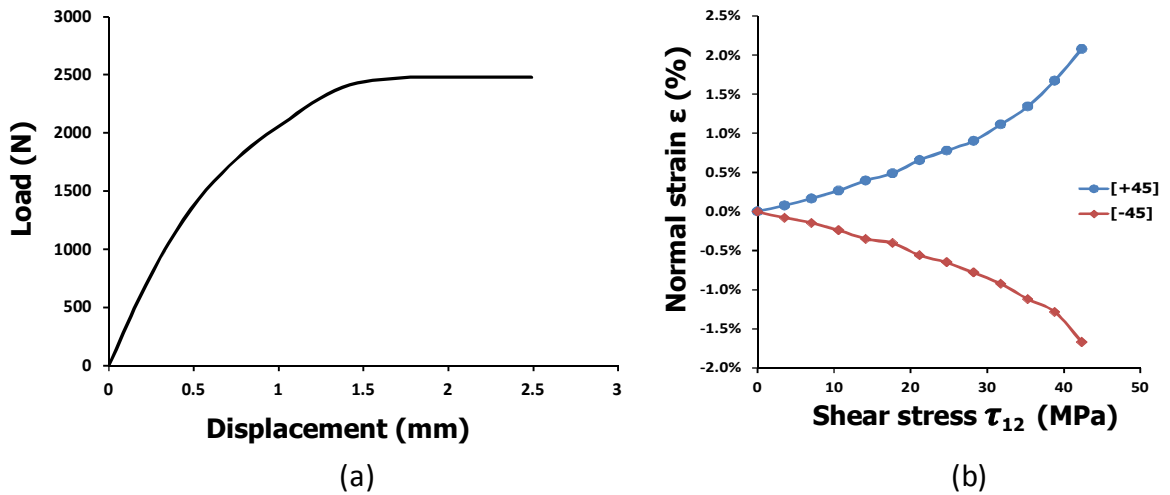


Figure 3.11 In-plane shear properties of cross-ply, $[0/90]$, laminate: (a) Load-displacement diagram, (b) τ_{12} versus ϵ_{+45} and ϵ_{-45} of the test specimen

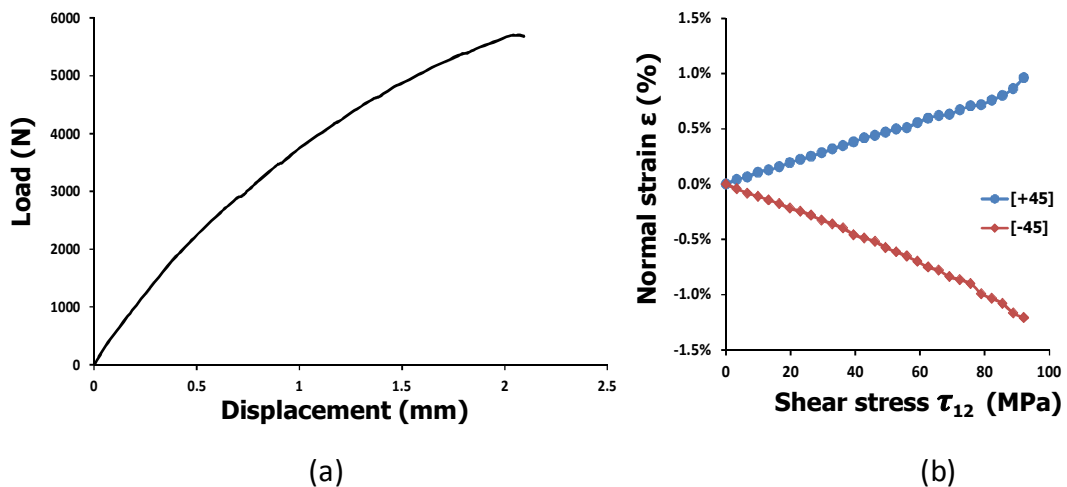


Figure 3.12 In-plane shear properties of angle-ply, $[\pm 45]$, laminate: (a) Load-displacement diagram from the testing machine, (b) τ_{12} versus ϵ_{+45} and ϵ_{-45} of the test specimen

3.4.3 Failure mode of the V-notch shear specimens

As the applied load was increased, cracks formed in the matrix of the 90° ply within the $[0/90]$ laminate (fibers are parallel to the loading direction). Small cracks coalesced, leading to the formation of one macro-crack running between the two ends of the specimen. Eventually, the stress got transferred to the 0° ply, leading to failure of fibers in bending. The $[0/90]$ laminate failed due to shear stresses along the roots of the notches. A straight shear crack parallel to the loading direction and parallel to the line joining two roots of the V-notches has been observed, shown in Fig. 3.13 (a).

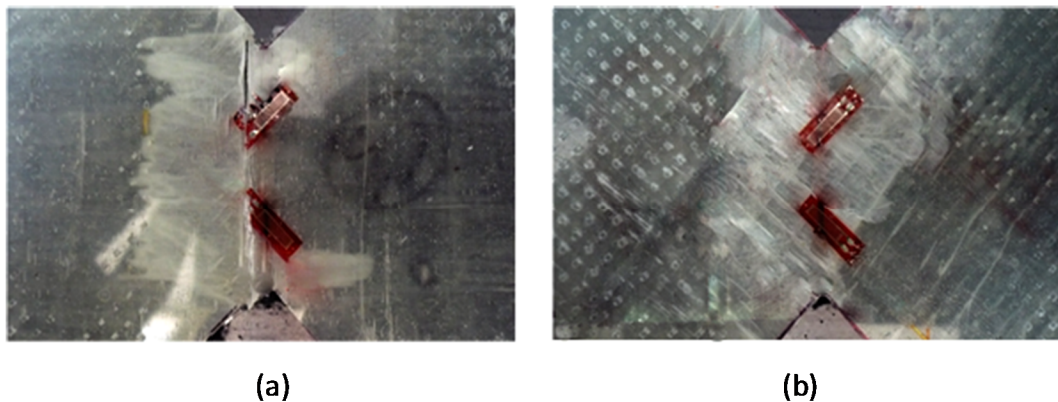


Figure 3.13 (a) Cross-ply, $[0/90]$ and (b) angle-ply, $[\pm 45]$ specimens at the end of the test. The cracks in the $[\pm 45]$ laminate had initiated at the roots of the V-notches and propagated along the fiber directions as shown in Fig. 3.13 (b). Catastrophic specimen failure of the $[\pm 45]$ laminate did not take place, even when subjected to a load of 6 KN more than twice the failure load in case of $[0/90]$ laminate. The shear strength and modulus of the $[\pm 45]$ laminate are higher than for the $[0/90]$ laminate, because the loading takes place along the fiber direction in the $[\pm 45]$ laminate.

The in-plane shear stress-strain curve, up to 4% strain, has been plotted in Fig. 3.14 for both the laminates. The stress-strain response has been nearly linear in the case of the $[\pm 45]$ laminate, as the fibers have taken the maximum load for in-plane shear loading. The stress-strain response has been non-linear from the beginning in the case of the $[0/90]$ laminate. Here, the maximum load has been taken by the matrix material for in-plane shear loading.

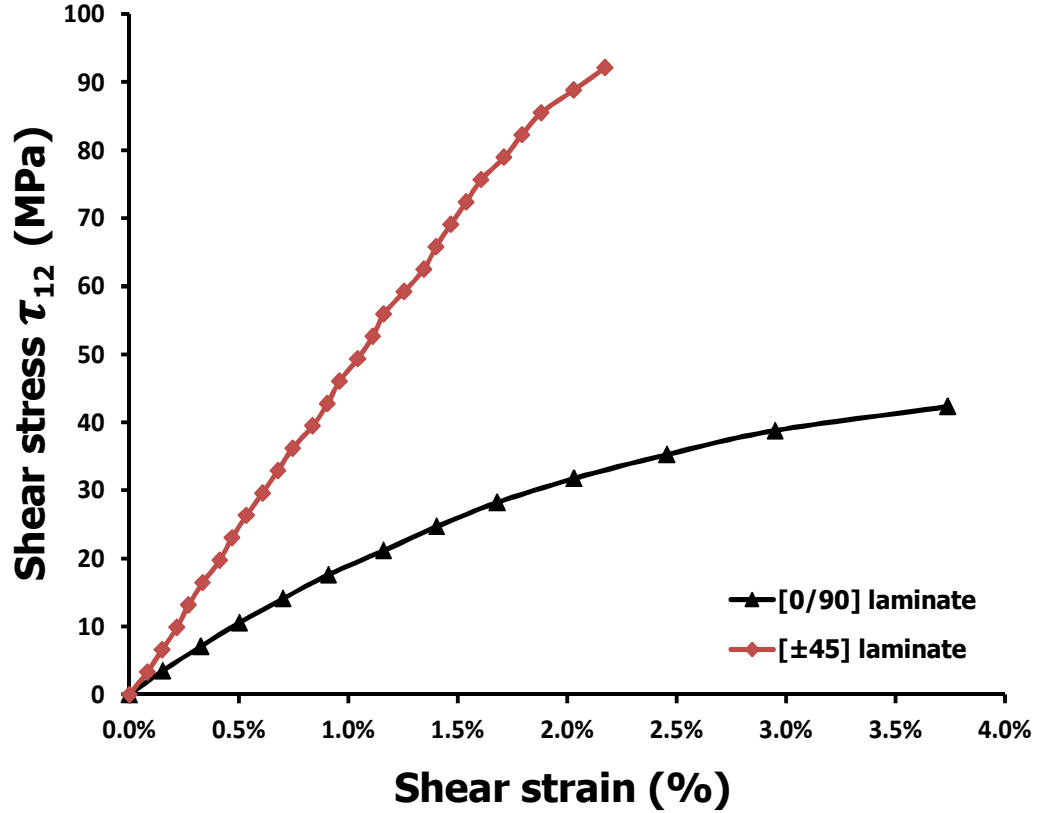


Figure 3.14 In-plane shear stress-strain experimental response for cross-ply, [0/90] and angle-ply, [±45], laminate (Appendix-I)

3.4.4 Global stress-strain response

The proposed M^2RVE has been subjected to in-plane shear loading with periodic boundary conditions explained in Section 3.2. The analysis has been performed using Rik's algorithm for non-linear analysis in ABAQUS Standard[®]. Rik's algorithm is type of arc length method used for non-linear analysis. Details about Rik's algorithm can be found in (Riks, 1978). At the end of each load step in the non-linear analysis, volume average stresses and strains for the [0/90]_n laminate obtained by using Eqs. (3.5) and (3.6), have been plotted, shown in Fig. 3.15. The in-plane shear stress-strain curves for the perfect bonding case, obtained from the numerical simulations for the composite have been also plotted (Fig. 3.15) along with the experimental data for the [0/90] laminates. Perfect bonding has been achieved by considering a very high value of interface stiffness and interfacial strength (50GPa, 70 MPa). Due to perfect bonding, the stresses developed in the matrix material have been transferred completely to the fiber material. Thus, the fibers take more load as compared to a model in which imperfect bonding has been used. The differences between simulations and experiments could be attributed to the assumption of perfect

bonding, and the assumption of no inter-ply delamination. In addition to perfect bonding, a curve with finite interfacial strength ($t_n = 30\text{MPa}$) for the $[0/90]_n$ laminates has been also plotted in Fig. 3.15. This value is consistent with the tests conducted by Zhou et al. (2001), where they had reported an interfacial strength value between 24 MPa and 38 MPa by fragmentation testing and 28 MPa and 58MPa by a push-out test for glass fiber/epoxy composite system. The initial region of the stress–strain curves with finite interfacial strength has been similar to experimental results up to a shear strain of approximately 1%. Beyond this point, the response from the finite interfacial bonding strength condition has approached the experimental response again only after a strain of 3%. The maximum difference between the shear stress predicted using $M^2\text{RVE}$ and the experimental results has been approximately 8% at the strain value of around 2% for the $[0/90]_n$ laminate. It can be clearly observed that the proposed $M^2\text{RVE}$, when used along with interface surfaces with finite cohesive strength, leads to the better estimation of the global stress-strain response.

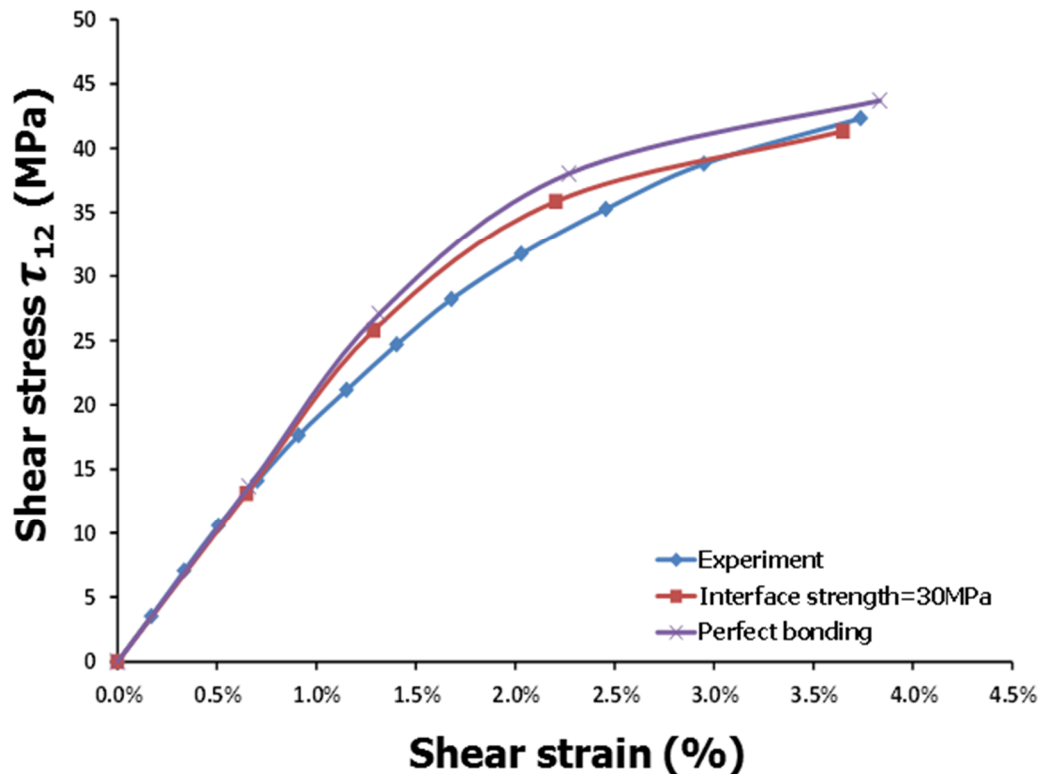


Figure 3.15 In-plane shear stress-strain response of $M^2\text{RVE}$ for the $[0/90]_n$ laminate with perfect and imperfect bonding between matrix and fiber

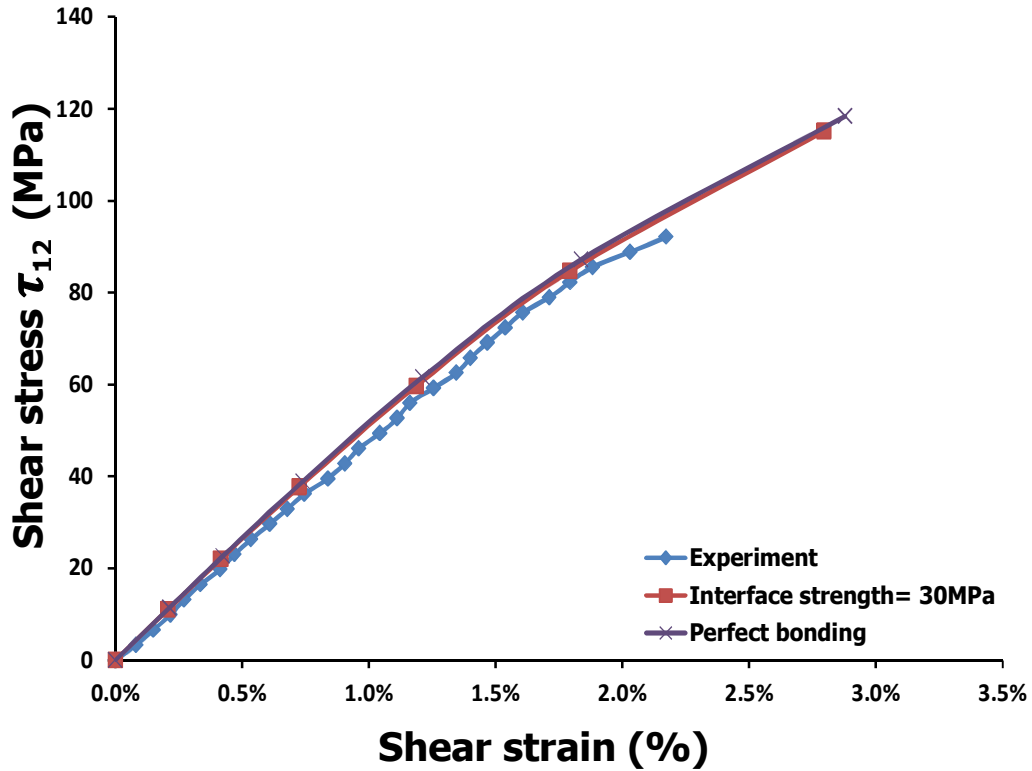


Figure 3.16 In-plane shear stress-strain response of M^2RVE for the $[\pm 45]_n$ laminate with perfect and imperfect bonding between matrix and fiber

Fig. 3.16 shows the predicted in-plane shear stress response of $[\pm 45]_n$ laminates along with the experimental results. Here, there is very small difference between the response predicted by perfect bonding and the response predicted using cohesive surfaces. Both curves show very good agreement with the experimental results. This may be due the fact that interfacial debonding may not have occurred until a strain of 2% was reached. The difference between the shear stress predicted with imperfect bonding and experimental results has been approximately 3% at the strain value of approximately 1% for the $[\pm 45]_n$ laminate.

3.5 Results and Discussion

3.5.1 Stress and strain evolution at microscale

Fig. 3.17 (a) and (b) show the contour plot of the in-plane shear stress and in-plane shear strain in M^2RVE with cohesive strength equal to 30 MPa, respectively. The top and bottom lamina have been referred to as 0° (parallel to the applied displacement) and 90° (perpendicular to the applied displacement), respectively.

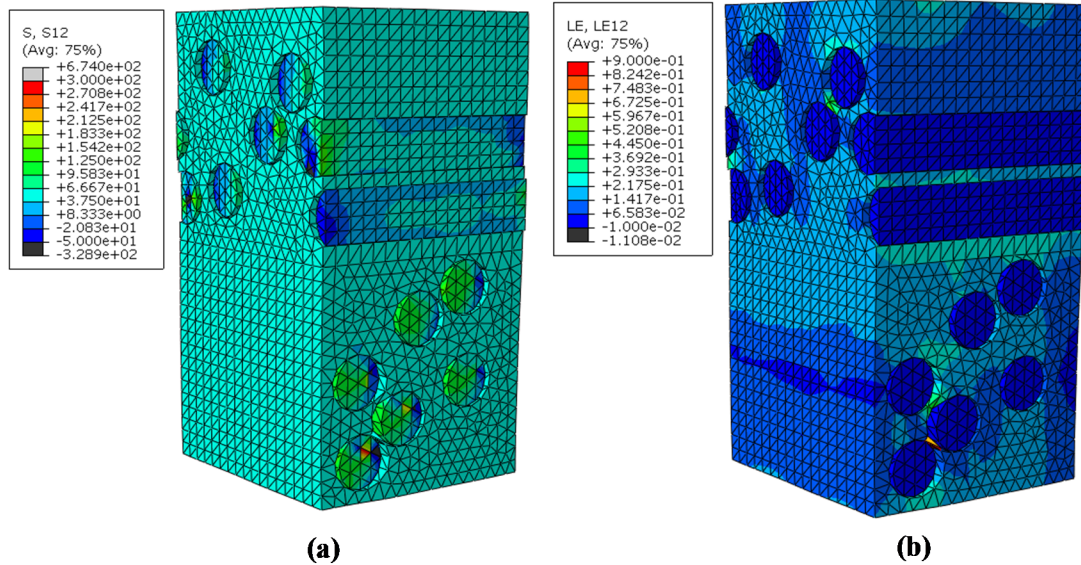


Figure 3.17 (a) Contour plot of the in-plane shear stress in M^2RVE with cohesive strength equal to 30 MPa, (b) Contour plot of the in-plane shear strain in M^2RVE with cohesive strength equal to 30 MPa.

In Fig. 3.17 (b), it can be seen that similar strain fields have been obtained in both the laminae. However, the stress plot that has been shown in Fig. 3.17 (a) is different because the 90° lamina is stiffer due to the perpendicular fiber orientation which induces higher stresses as opposed to the 0° lamina where the parallel fibers do not provide sufficient resistance to the deformation. The number of fibers consisting of higher (150 MPa) stresses are more in the 90° lamina than the 0° lamina, as seen in the plot. Fiber-matrix debonding is clearly visible in both the plots. The shear stresses developed in the fibers have been much higher than those of the matrix in both the cases due to the higher stiffness of fiber material.

3.5.2 Effect of fiber orientation on micro stress evolution

Fig. 3.18 shows the in-plane shear stress contour plot with an RVE (unidirectional lamina- single layer) made up of the same fiber and matrix material, with the same volume fraction subjected to in-plane shear loading parallel to the fiber direction.

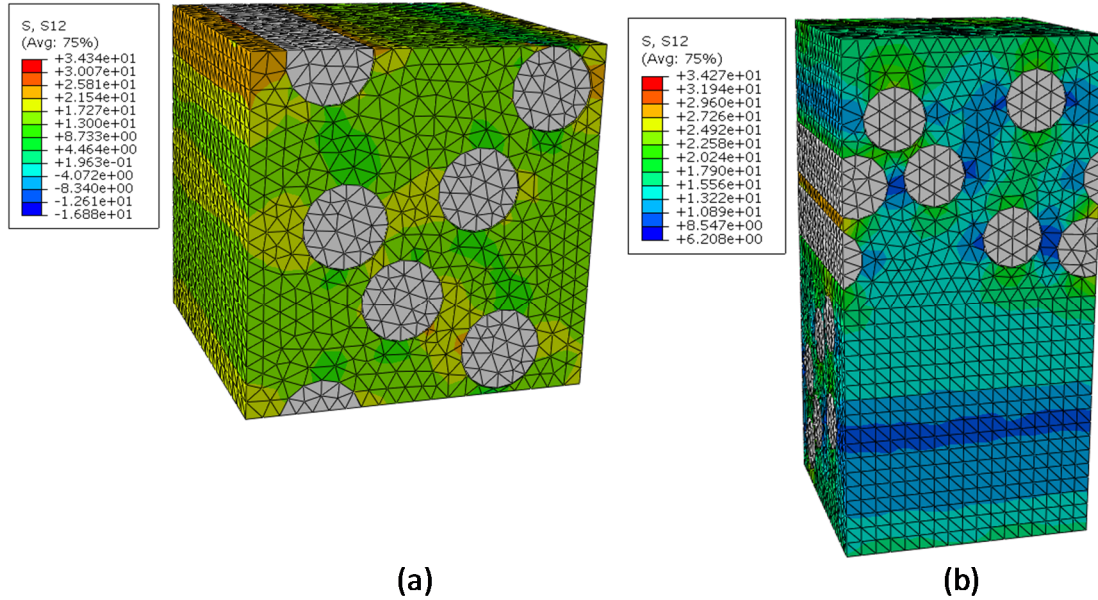


Figure 3.18 (a) Contour plot of the in-plane shear stress developed in matrix material with one layer multi-fiber RVE (b) Contour plot of the in-plane shear stress in matrix material using M^2RVE .

The matrix damage and interface failure criterion used has also been the same as used for the proposed M^2RVE . The results at the same load level have been compared with the in-plane shear stress plot of the 0° lamina (top cube from M^2RVE). The fiber distribution is different in both the models as it has been generated using a randomization algorithm. Shear stresses that had developed in both the microstructures at the same low load level during the non-linear analysis can be observed in Fig. 3.18. The presence of another lamina, that is, a 90° fiber cube in M^2RVE alters the micro level stress evolution in the structure. The proposed M^2RVE has provided a realistic model for estimating microscale stress evolution.

3.5.3 Effect of Mohr-Coulomb matrix friction angle on stress-strain response

The in-plane stress-strain curves predicted by using the M^2RVE have been plotted in Fig. 3.19 for six different $[0/90]_n$ composite laminates with matrix friction angles ranging from 0° to 15° . Since the matrix tensile strength has been assumed to be constant and equal to 75 MPa, changes in the friction angles modifies the cohesive strength 'c' of the matrix, given in Eq. (3.9). The cohesive strength of the matrix increases from 37.5 MPa ($\varphi=0^\circ$) up to 59MPa ($\varphi=25^\circ$). Fig. 3.19 shows that with an increase in the friction angle (consequently an increase in cohesive strength of the matrix) shear strength of the composite increases. The simulated response shows the same

response until a stress value of 30 MPa, followed by an increase in the hardening effect with an increase in the value of the friction angle.

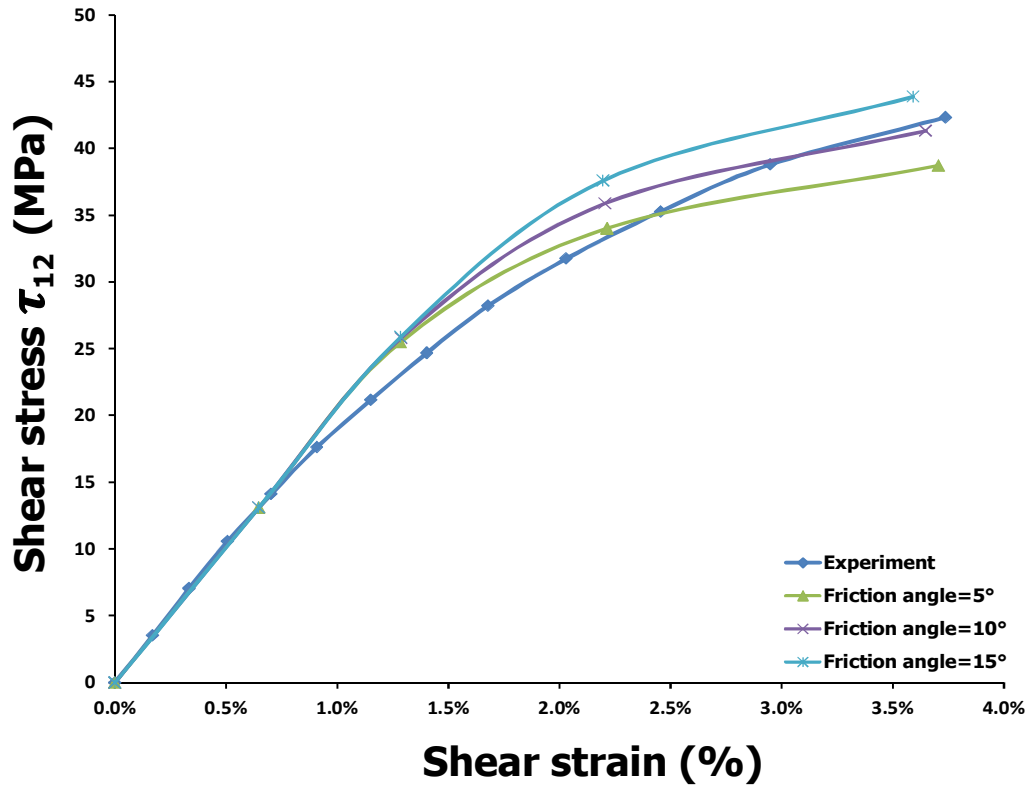


Figure 3.19 In-plane shear stress-strain response of M^2RVE for $[0/90]_n$ laminate with different matrix friction angle

Fig. 3.20 shows the effect of the matrix friction angle on the in-plane shear stress-strain response of a $[\pm 45]_n$ laminate. Here, the matrix friction angles between 0° and 15° have been used. The stress-strain response changes beyond a strain value of approximately 1.5%. It has been observed that the effect of matrix friction angle on the stress-strain response for the $[\pm 45]_n$ laminate has been negligible. A friction angle of 10° has been used for all the subsequent simulations of $[\pm 45]_n$ laminates.

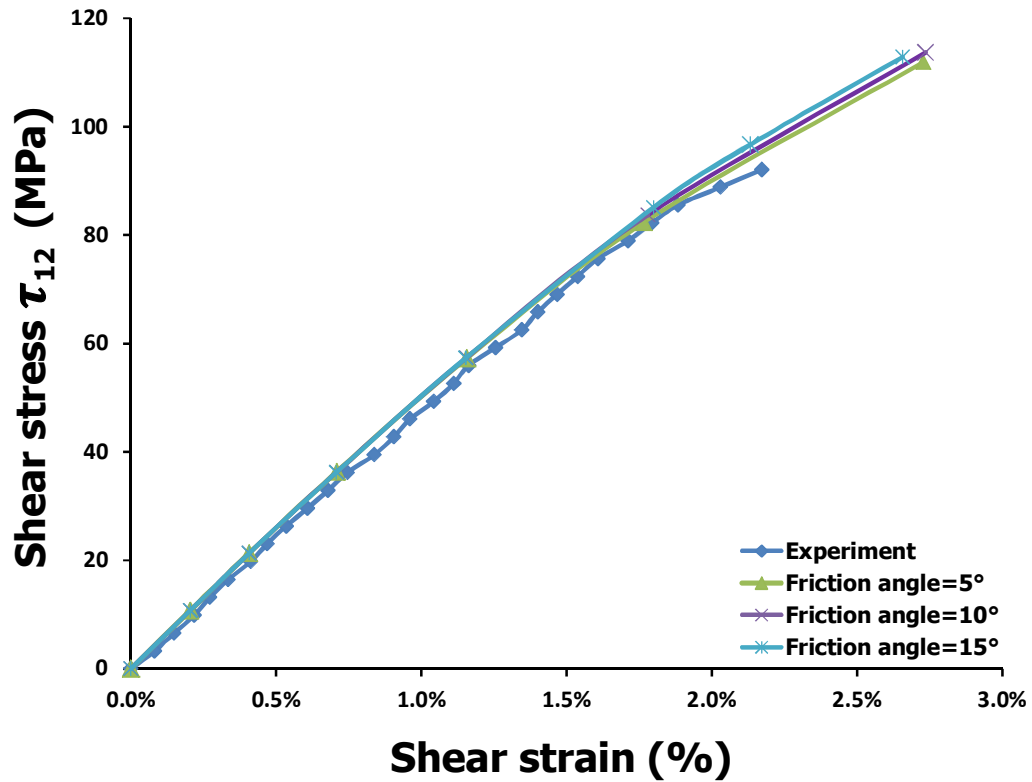


Figure 3.20 In-plane shear stress-strain response of M²RVE for [±45]_n laminate with different matrix friction angle

3.5.4 Effect of interface strength on global stress-strain response

It can be observed in Fig. 3.17 (a), that stresses are transferred to the fibers via the interface and high stresses are developed in the fibers in the case of a 90° lamina. Interface failure leads to the reduction in the slope of the linear hardening region of the stress-strain curve, shown in Fig. 3.15. The model prediction for the behavior of the cross-ply composite, assuming debonding between matrix and fiber has been in good agreement with the experimental data. In particular, the model has been able to account for the quantitative effect of damage by interface de-cohesion on the load transfer from the matrix to the fibers.

It is expected that the effect of interfacial bonding strength will affect the in-plane shear response. Hence, different cohesive strength values of between 10 MPa to 40 MPa have been used to perform a parametric study on the proposed model. The corresponding response curves for [0/90]_n laminates have been shown in Fig. 3.21. It has been found that there is no effect of increasing the interfacial strength beyond 30 MPa on the global shear stress- strain response. These results show that the interface de-cohesion limits the load transfer from the matrix to the

fibers under in-plane shear loading leading to a reduction in the slope of the linear hardening region after matrix yielding.

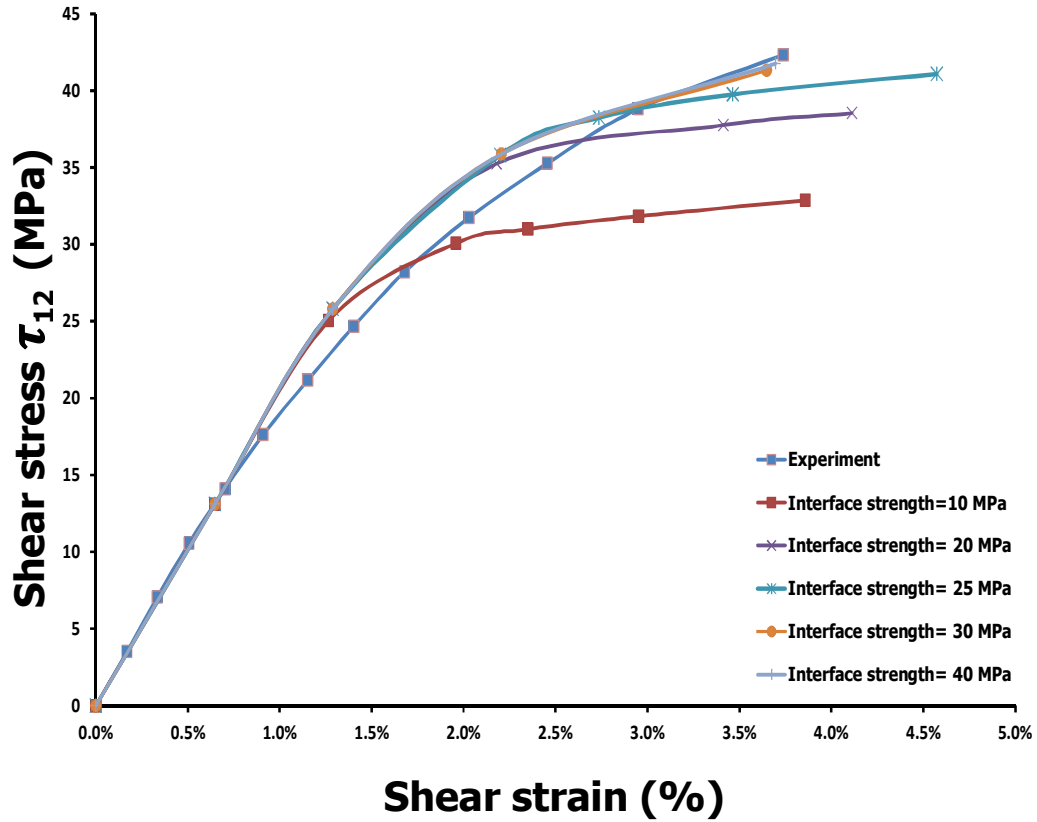


Figure 3.21 In-plane shear stress-strain response of M²RVE for [0/90]_n laminate with different bonding strength between fibers and matrix

Fig. 3.22 shows the effect of interface strength on the shear stress-strain response of [±45]_n laminates. Different cohesive strength values of 5, 10, and 30 MPa have been used in the simulations. It has been found that there is no effect of interface strength on the shear stress-strain response. Thus, it can be concluded that the interface strength has no significant impact on the shear stress-strain response on a [±45]_n laminate. This has been due to fact that there was little to no interface failure until a strain 3% had been reached. A Cohesive strength of 30 MPa, used for the simulations, provides an accurate global stress-strain response in the case of both laminates.

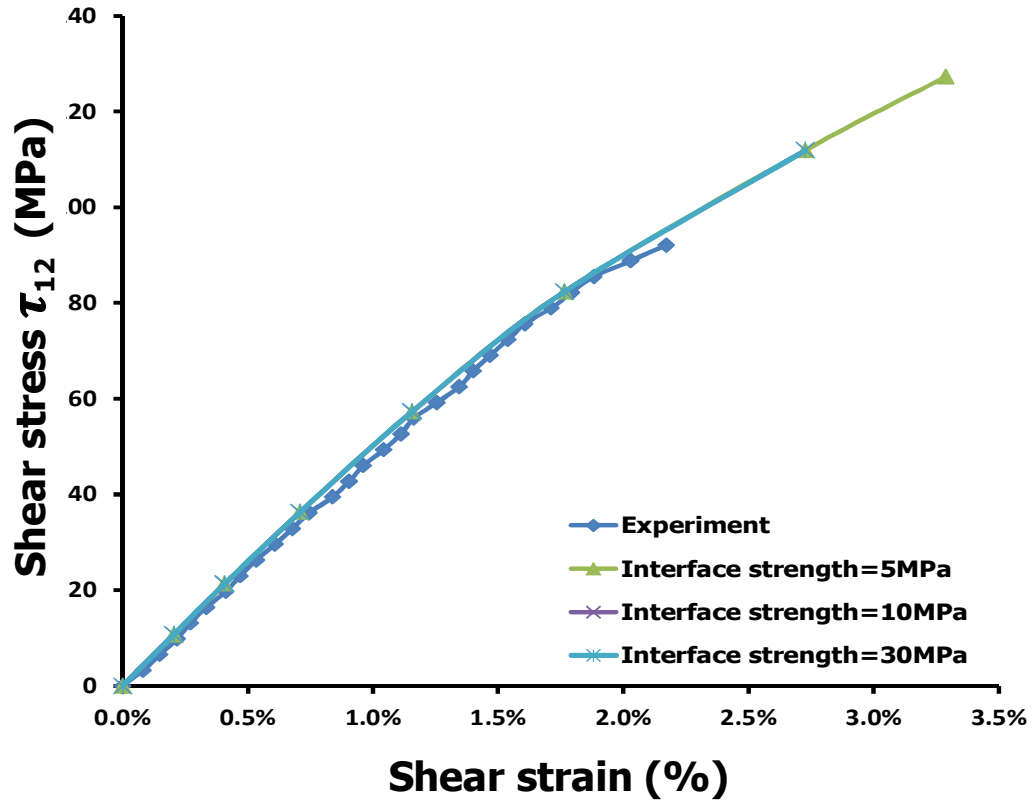


Figure 3.22 In-plane shear stress-strain response of M²RVE for [±45]_n laminate with different bonding strength between fibers and matrix

3.5.5 Effect of fiber orientation on debonding initiation and progression between the fiber and the matrix

The damage due to fiber-matrix decohesion or debonding has had a significant effect on the overall mechanical behavior of the composites, as observed in Fig. 3.15. In order to study damage initiation and progression due to debonding in the [0/90]_n and [±45]_n laminates, a “state-based” tracking algorithm has been used for three-dimensional finite-sliding, surface-to-surface contact pairs with deformable surfaces. Contour plots of variable COPEN used to find out clearance between surfaces in ABAQUS[®], have been presented in Fig.3.23 and Fig. 3.24, respectively. For node-to-surface discretization the variables COPEN represent the relative positions normal to the interface, that is, the closest distance between the node and the surface at the end of the simulation. The output COPEN is typically provided where surfaces are opened by a small amount compared to surface facet dimensions, suitable for the present case. The contour plot describes the distance between the node on the surface of the fiber and the matrix material (surface to surface interaction) at the end of the simulation. For a given integration point,

debonding has been said to have occurred when the value of variable COPEN exceeds the displacement ' δ ' value (see Fig. 3.23 and Fig. 3.24). In the present case, the stiffness of cohesive surfaces has been taken as 35 GPa, cohesive strength (t_n and t_s) has been taken as 30 MPa, and fracture energy has been considered as 100 J/m²; thus, the distance at which the fiber-matrix decohesion had been expected to have occurred has been calculated as $\delta = 0.086 \mu\text{m}$ (Ronald et al., 1991). As shown in Fig. 3.23 (a), fiber-matrix debonding initiates at 1% strain in the 0° lamina(layer 1). Fig. 3.23 (b) shows the progression of debonding in the [0/90]_n laminate. The progression plot shows that amount of debonding is equal at the end of the analysis in both the laminae and debonding has mainly accumulated in the side faces of all the fibers with respect to the loading direction.

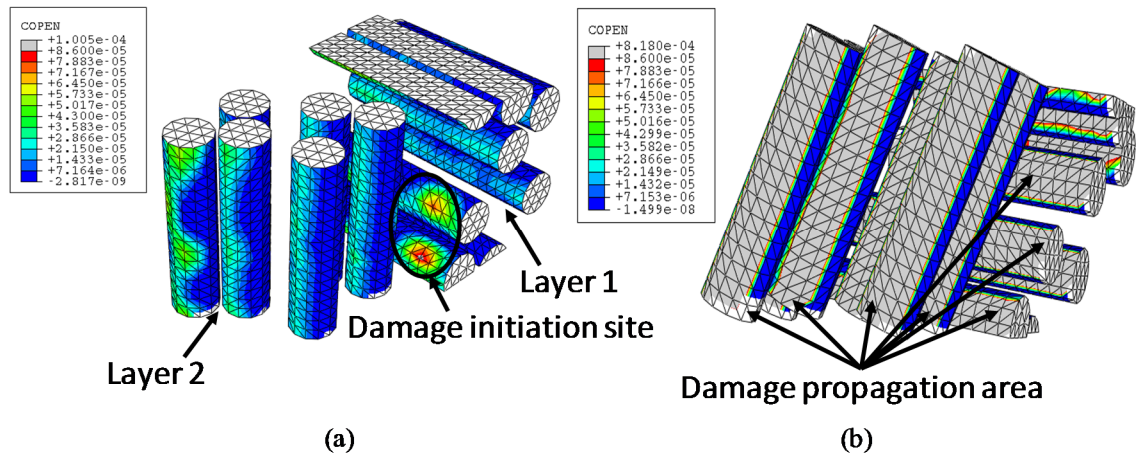


Figure 3.23 Fiber-matrix debonding in [0/90]_n laminate (a) Debonding initiation (b) Debonding propagation at the end of the step

As shown in Fig. 3.24 (a), decohesion initiates at a strain value of 2% in the case of a [± 45]_n laminate. For the [± 45]_n laminate subjected to in-plane shear loading, fibers in the [+45] lamina have experienced tension and fibers in the [-45] laminate have experienced compressive forces. The top and bottom laminae have been referred to as layer 1 and layer 2, respectively, as shown in Fig. 3.24. The decohesion initiates in the lamina which experiences tensile loading (layer 1). The progression of debonding has also dominated in the lamina experiencing tensile loading as shown in Fig. 3.24 (b). Uneven distribution of debonding has been observed in the case of the [± 45]_n laminate. 58% of total debonding has occurred in the top lamina (layer 1). This may be due the fact that tensile loading always tends to open the crack (decohesion in this case) as opposed to compressive loading.

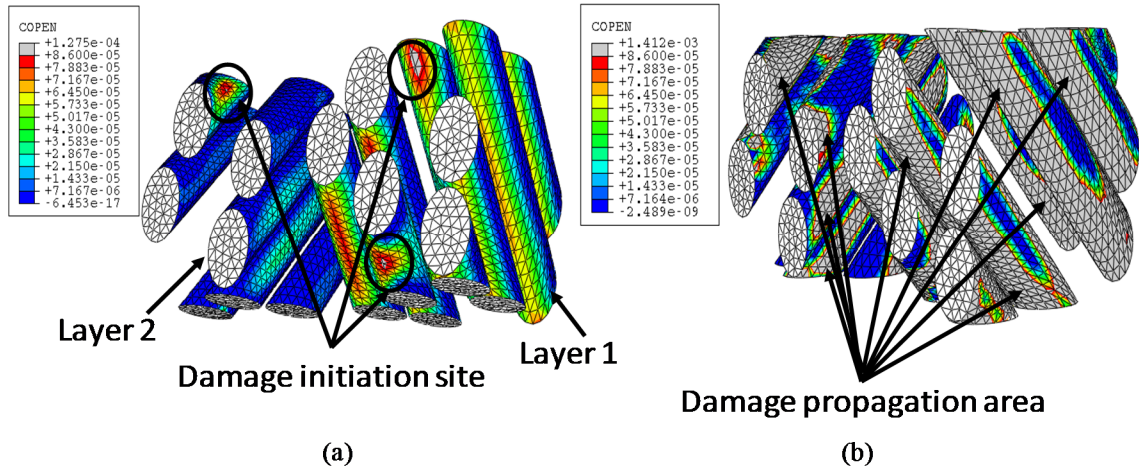


Figure 3.24 Fiber-matrix debonding in $[\pm 45]_n$ laminate (a) Debonding initiation (b) Debonding propagation at the end of the step

3.5.6 Effect of fiber orientation on evolution of interface damage area

The percentage of damaged interface has been defined as the ratio of the area of the interface that had undergone decohesion to the total interface area. Fig. 3.25 shows the percentage of damaged interface in each layer along with total percentage of damage interface with respect to in-plane shear strain for $[0/90]_n$ laminate. Interface damage initiates at 1% strain in layer 1 and propagates at a slow rate between 1% to 2% strains in both the layers. Eventually, the growth accelerates between the strain values of 2% to 4%. During this span there is a corresponding change in global in-plane shear stress response, which can be observed in Fig. 3.15. It can be observed that the amount of interface failure is nearly the same in both the layers during the entire simulation. The effect of decohesion starts becoming significant after the strain value of 2.5%, as observed in Fig.3.15 and Fig.3.21.

Fig.3.26 shows the percentage of damaged interface versus in-plane shear strain plot for the $[\pm 45]_n$ laminate. Here, it can be observed that fiber-matrix decohesion initiates at the in-plane shear strain value of 2%, as also observed in Fig.3.16. It can be observed that debonding has been prominent in layer 1 as compared to layer 2. 80% of the interface area in layer 1 has been damaged when only 22% of interface area has been damaged in layer 2 at the end of the simulation. As interface failure initiates it can be observed that there has been a sudden jump of 10% interface failure in the total interface area after the debonding initiation. A similar jump in the percentage of interface failure has been observed between the in-plane shear strain value of 1% and 3% followed by steady growth.

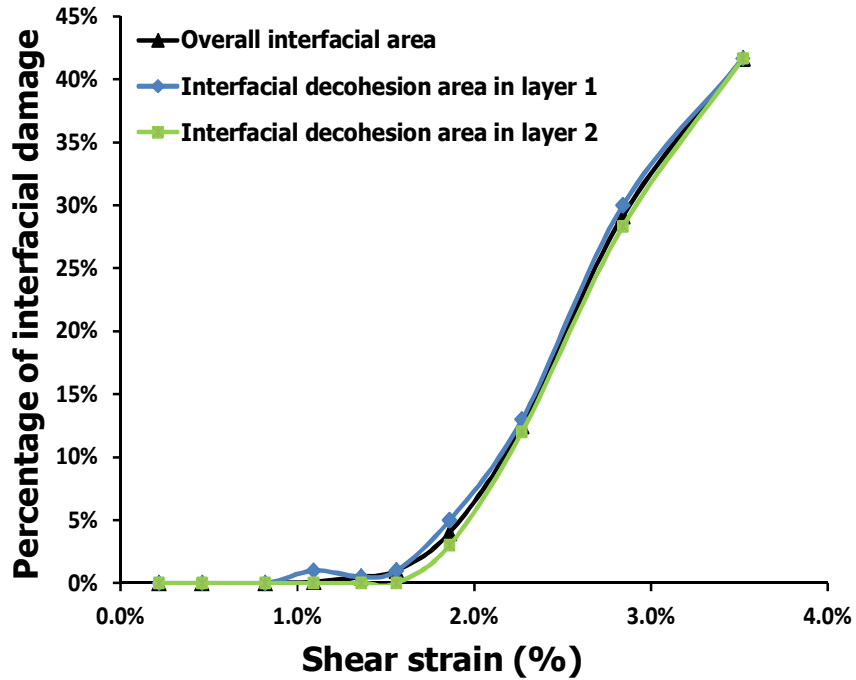


Figure 3.25 In-plane shear strain versus percentage of damage fiber-matrix interface for $[0/90]_n$ laminate

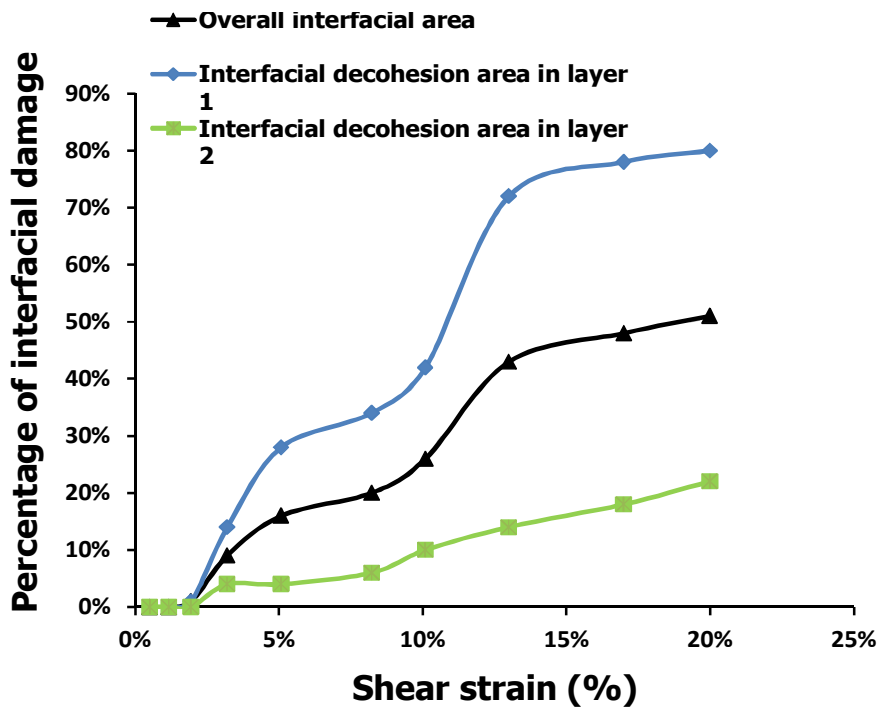


Figure 3.26 In-plane shear strain versus percentage of damage fiber-matrix interface for $[\pm 45]_n$ laminate

3.5.7 Shear stress-slip behaviour at the interface

Fig. 3.27 shows plot between frictional shear stress developed at the surface nodes of the interface as a function of slip developed at the interface for the $[0/90]_n$ laminate. Two slip directions have been considered, namely, slip parallel to the fibers and slip circumferential to the fiber diameter referred as direction 1, and direction 2, respectively. Fig. 3.27 shows that shear stresses have developed and the amount of slip has been same for both the directions in case of the $[0/90]_n$ laminate. Shear stresses in both the directions increase with an increase in the slip till a shear strength of 30 MPa (strength of the interface is defined as 30 MPa). The slip is inappreciable till the shear strength of the interface has been reached; once the shear strength is reached the slip increases significantly. This indicates that the physical separation has occurred at about 0.001 mm in both the slip directions.

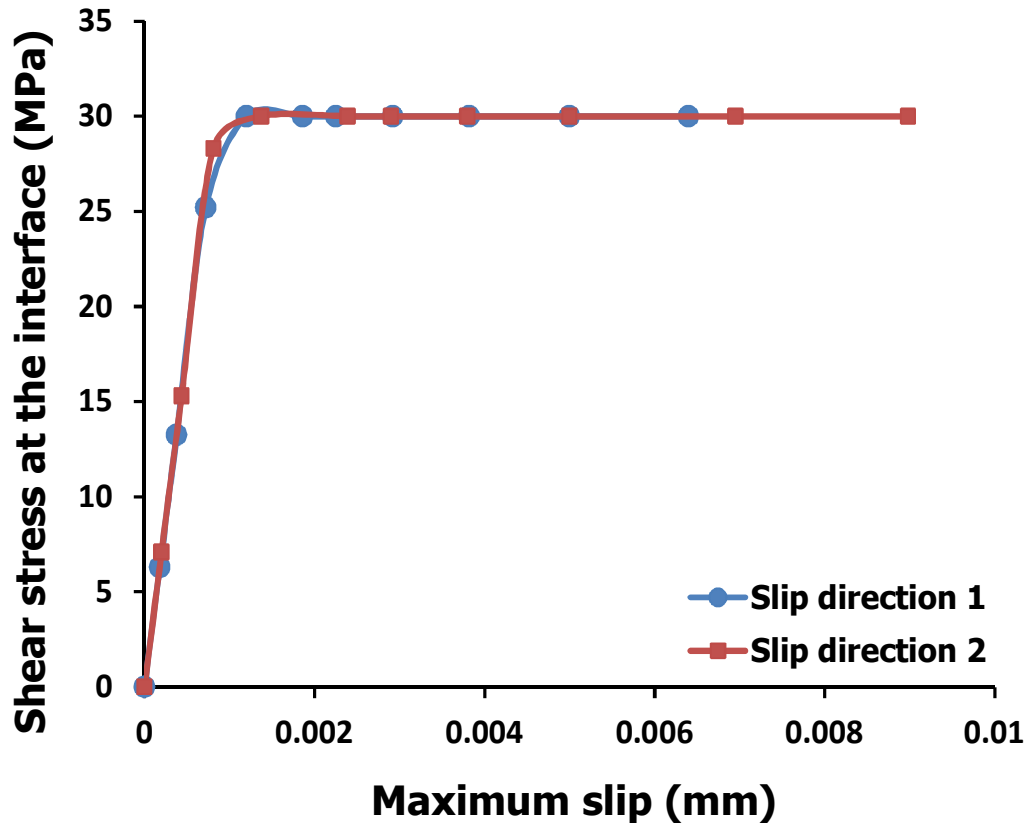


Figure 3.27 Shear stress at the interface versus slip at the interface for $[0/90]_n$ laminate

Fig. 3.28 shows plot between frictional shear stress that had developed at the surface nodes of the interface as a function of the slip that had developed at the interface for the $[\pm 45]_n$ laminate. It can be observed that the shear stress that had developed at the interface increases with an

increase in slip in both the directions. Shear stresses developed and the amount of slip has been higher in case of direction 1 as compared to direction 2 (having same slope). The observation is aligned with the amount of debonding to be more in the layer 1, which has experienced tensile loading in case of the $[\pm 45]_n$ laminate. Thus, it can be concluded that the amount of interfacial slip, shear stresses that had developed at the interface and slip are higher in the layer experiencing tensile loading in $[\pm 45]_n$ laminate. However, unlike $[0/90]_n$ the values of slip do not increase without an associated increase in the shear stress in the case of $[\pm 45]_n$. Consequently, it can be construed that physical separation does not occur in this case.

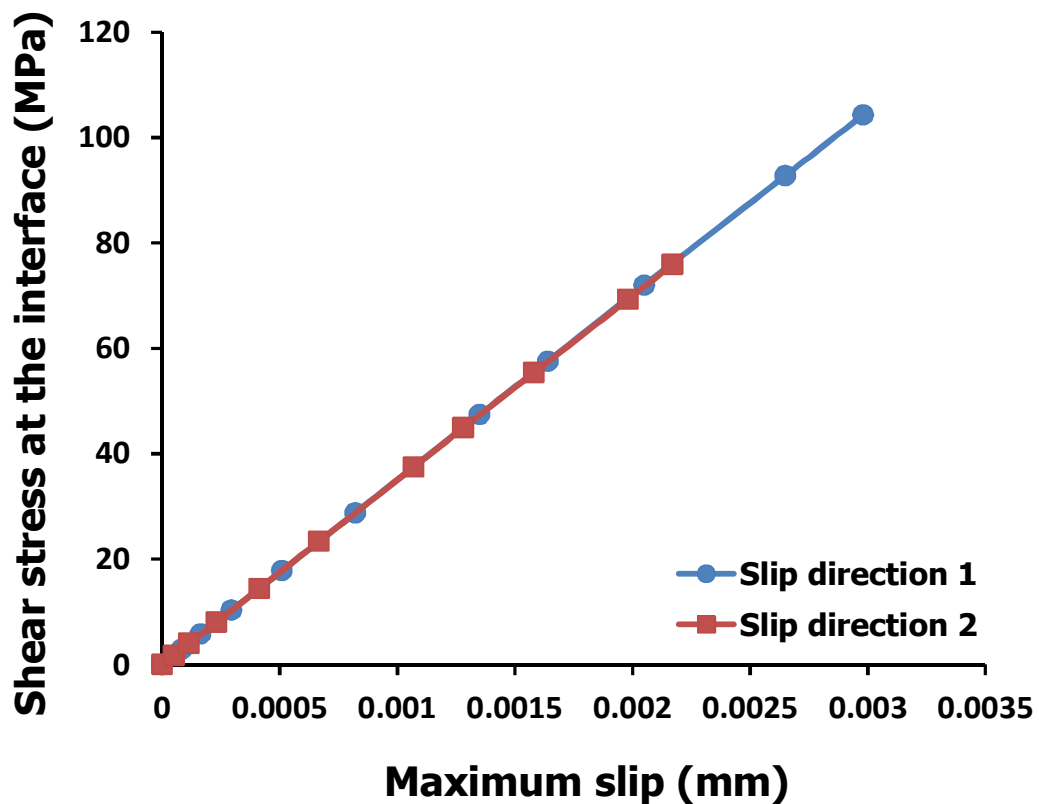


Figure 3.28 Shear stress at the interface versus slip at the interface for $[\pm 45]_n$ laminate

3.6 Summary

This chapter presented a multi-layer multi-fiber representative volume element (M^2RVE) approach to predict global material response as well as local stress fields and damage evolution in a composite laminate. The results obtained from simulations have been validated against experiments performed on glass fiber/epoxy cross-ply, $[0/90]$ and angle-ply, $[\pm 45]$ composite laminates. The proposed M^2RVE captures the intra-ply and inter-ply interactions on stress

evolution as it has used two laminae. It was found that there is a significant effect of matrix and interfacial properties on the global as well as local material response. The proposed model can quantify the fiber-matrix interfacial damage. It may be noted that this chapter studies only in plane shear loading, hence the next chapter presents is focused on damage evolution under complex multi-axial loading. In addition, the fiber failure and delamination which have not been addressed in this chapter have been incorporated in the improved M^2 RVE based model in the next chapter.

Chapter 4: Comprehensive damage analysis for complex multi-axial loading via M^2RVE

4.1 Introduction

This work is focused on using M^2RVE to capture all the damage mechanisms, namely, fiber failure, matrix damage, fiber-matrix and interlaminar decohesion for complex multi-axial loading. The fiber failure and matrix cracking are based on maximum principal stress criterion and multi-axial Mohr-Coulomb criterion, respectively. It has been demonstrated by Feih et al. (2005) that the fiber failure is often triggered by fiber surface flaws. To simulate fiber failure González and Llorca (2006) have used randomly placed damageable (cohesive) elements along the fiber length. Random arrangement is provided to incorporate statistical variability of the fiber properties. Wang et al. (2011) have also used randomly placed damageable layers having same elastic properties as fiber material (except that they are damageable) along the fiber length. Very few studies using RVE have implemented brittle failure models, such as maximum principal stress or brittle cracking. Fiber-matrix debonding and delamination between plies have been captured by introducing a cohesive layer in conjunction with standard traction separation law. It is known that the nature of damage evolution depends on the loading conditions. In plane tensile loading primarily causes the tensile failure of the fibers. Damage due to in-plane shear loading is dominated by matrix cracking and fiber-matrix debonding. Out-of-plane tensile loading triggers delamination. Additionally, in order to study the evolution of different damage mechanisms simultaneously, a combination of loads which trigger different failure mechanisms has been used.

4.2 Finite element modeling of M^2RVE

4.2.1 Generation of the geometrical and FE model

Fig.3.4 shows a typical configuration M^2RVE for $[0/90]_n$ laminate. The M^2RVE (matrix and fibers) is meshed using a four-node linear tetrahedral (C3D4) elements in ABAQUS Standard[®](2009). Higher order elements modified quadratic 10-node tetrahedral (C3D10M) elements have also been checked. However, higher order elements were requiring higher computational power without change in results as shown in Fig.4.1. Also, there was a

compatibility issue with higher order elements and cohesive elements used for delamination capture, therefore linear tetrahedral (C3D4) elements have been used in this model.

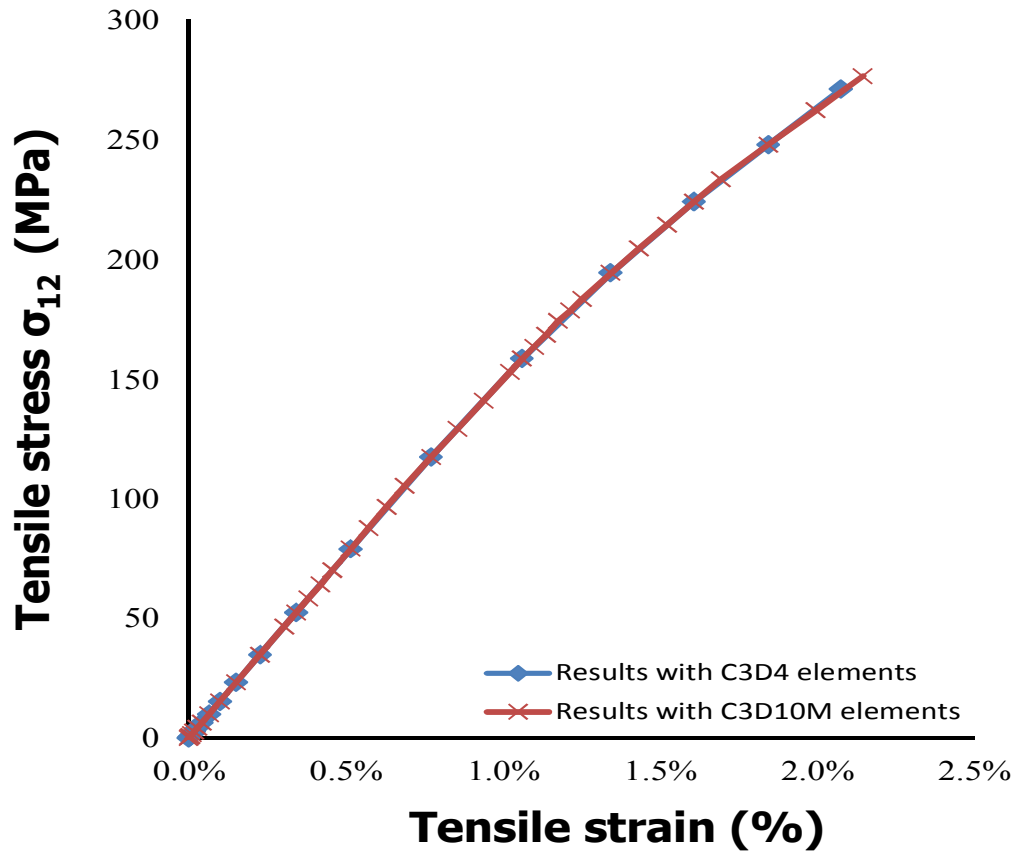


Figure 4.1 Results with C3D4 and C3D10M element type

Cohesive surfaces are included between each fiber and matrix material to capture fiber-matrix debonding. A thin layer of COH3D6 cohesive elements are provided between 0° lamina cube and 90° lamina cube for capturing possible delamination. The size of M^2RVE should be large enough so that the average properties are independent of its size and position within the material. The size of the M^2RVE also depends on the phase, and spatial distribution. In the chapter 3 of the thesis it has been demonstrated that there is no effect of cube size on the global stress and strain response. Therefore, 0.1 mm size cube has been used in the further study.

4.2.2 Boundary conditions

As has been mentioned previously, the M^2RVE is a representative unit for the cross-ply laminate, shown in Fig.3.2. Periodic boundary condition has been applied to M^2RVE as explained in section 3.2.2 .

4.2.3 Loading conditions

The aim the present work is to study all the microscale damage mechanisms, viz., fiber breakage, fiber-matrix debonding, matrix failure and delamination in laminated composites. To capture the prominent failure mechanisms observed in laminated composites different loading conditions have been identified. Fig. 4.2 shows various loading conditions used to study microscale damage evolution via M^2RVE .

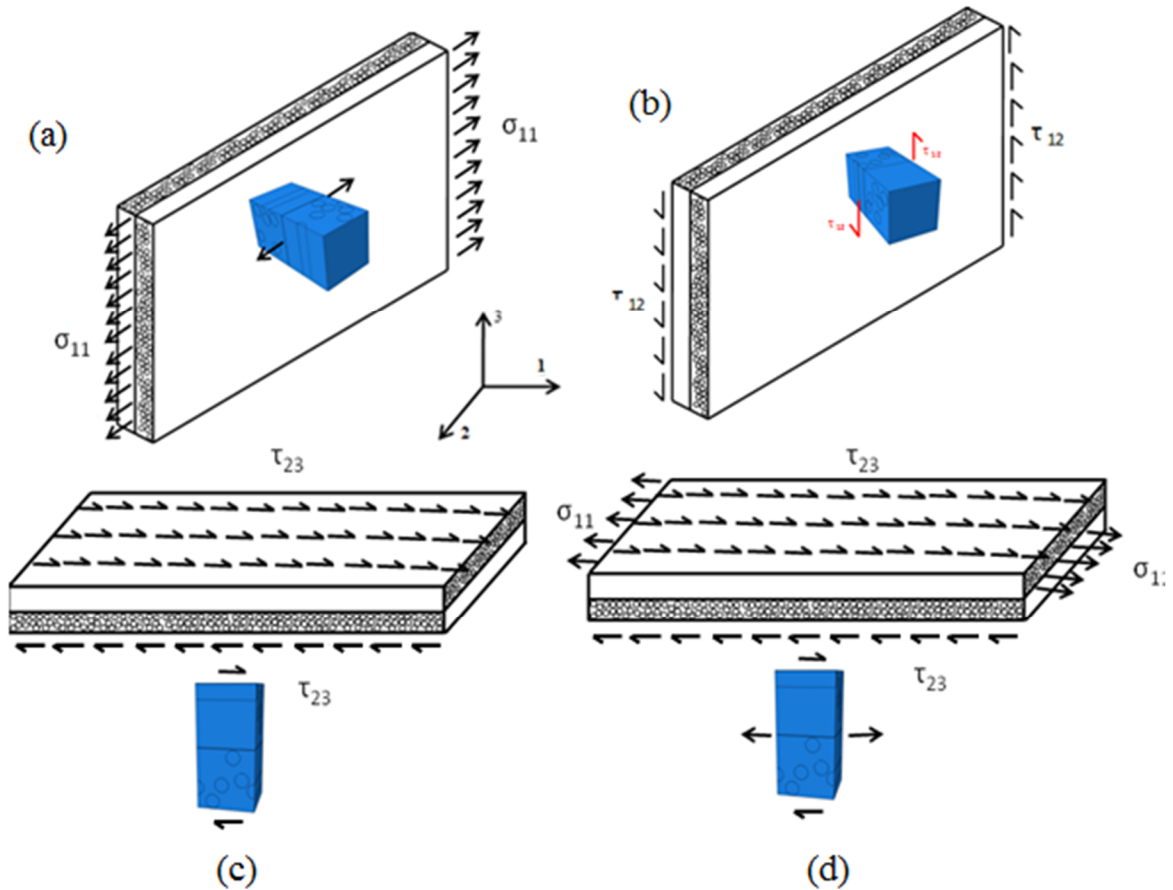


Figure 4.2 (a) In-plane tensile loading (b) In-plane shear loading (c) Out-of-plane shear loading (d) Combined in-plane tensile and out-of-plane shear loading

To capture fiber failure, in-plane tensile loading as shown in Fig. 4.2(a), has been used. To capture matrix failure and fiber-matrix debonding, in-plane shear loading has been used as shown in Fig. 4.2(b). In case of out-of-plane shear loading, interlaminar decohesion (delamination) failure dominates the failure process as shown in Fig. 4.2(c). The damage process is also affected by the matrix and fiber-matrix interface properties. To capture all the failure mechanisms simultaneously, in-plane tensile and out-of-plane shear loading are applied together

as shown in Fig. 4.2(d). A detailed analysis has been performed for each type of loading and global as well as local damage response has been reported.

4.2.4 Material Properties

M^2RVE for $[0/90]_{ns}$ laminate is modeled by using E-glass (ER-459L) fibers and epoxy matrix (EPOFINE-556 with FINEHARD-951 hardener) as linear elastic isotropic solids and their constants are provided in Table 3.1.

4.3 Failure criteria

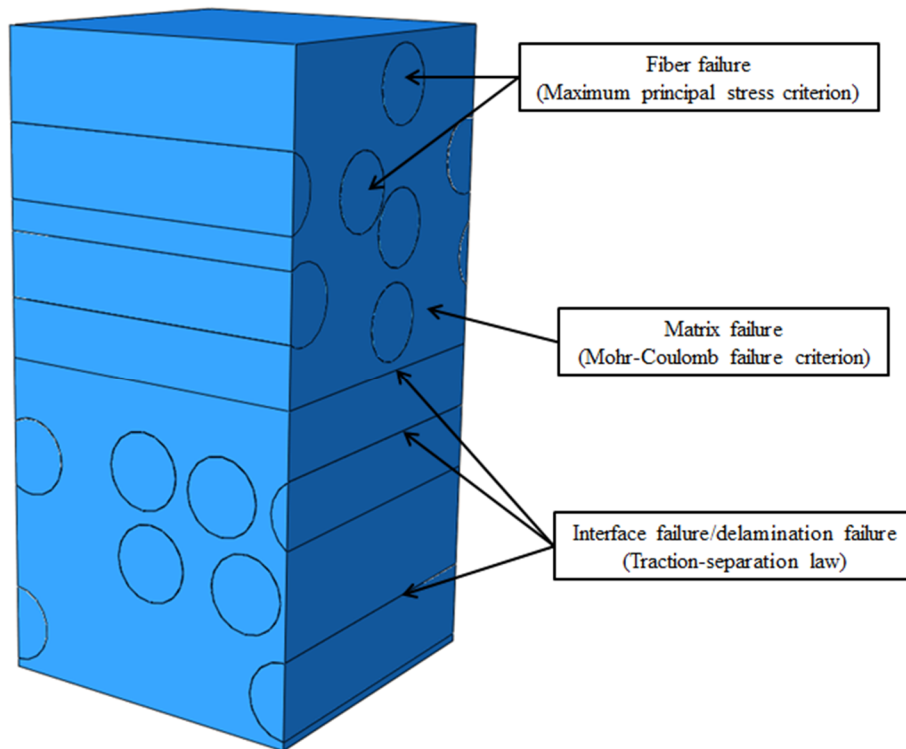


Figure 4.3 Schematic representation of the failure criterion used for matrix and fiber-matrix debonding

In the damage process of laminated composite different failure mechanisms are involved. However, only one or two of the damage mechanisms dominate the failure process for particular type of loading. Fig.4.3 shows different failure mechanism and their respective failure criterion considered during modeling of M^2RVE which are explained in the following section.

4.3.1 Fiber failure

Fibers are the main load-bearing elements of a fiber reinforced composite, which means that most of the mechanical properties of fiber-reinforced composites are primarily affected by fiber strength distribution (Shao et al., 2013). Glass fibers typically exhibit wide variability in strength, which is determined by the microstructural flaws that act as stress raisers. In order to determine fiber strength of 25 E-glass fiber (ER459L) specimens were mechanically tested using computer-controlled universal testing machine (*Favigraph, Textechno*). All tests were conducted in displacement control mode at a rate of 2 mm/min and at ambient temperature and pressure. All samples were maintained under load until mechanical failure occurred. The forces applied and the testing machine displacements were directly recorded on a chart recorder. Fig. 4.4 shows a typical load-cross head displacement curve for an E-glass fiber.

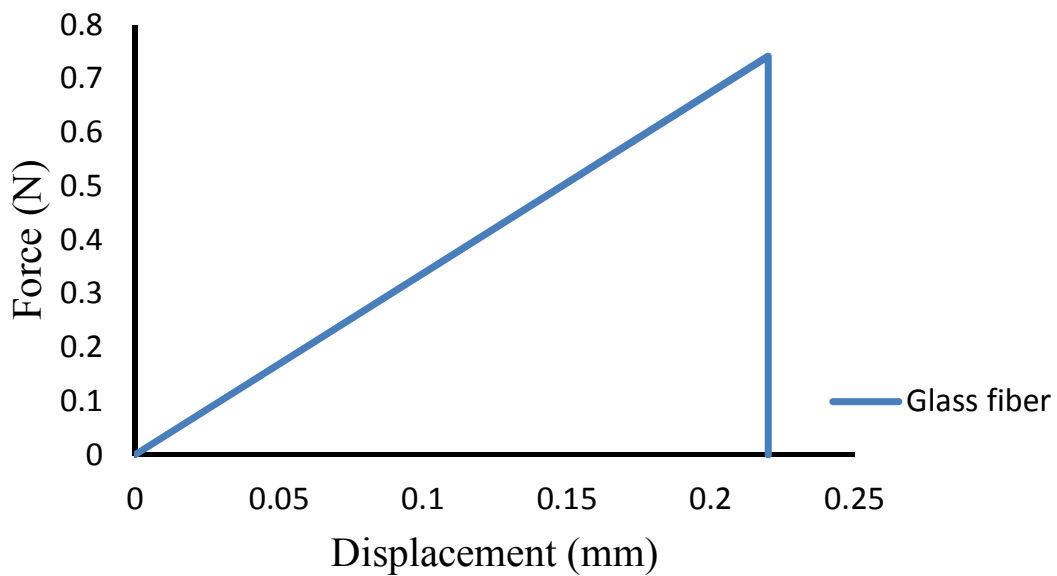


Figure 4.4 Typical experimental results of a classical load-displacement curve of glass fiber. It is explicitly mentioned in the literature that failure strength of the brittle material varies a lot and it is difficult to determine the strength value to be used for modeling of brittle materials. Weibull distributions (Weibull, 1951) are widely used to predict appropriate tensile strength of the glass fibers from experimental findings. The main purpose of the Weibull distribution function is that it makes it possible to estimate a population of infinite size from small amounts of data.

The two-parameter Weibull distribution for prediction of tensile strength of the glass fibers can be expressed as follows (Hao et al., 2012):

$$P(\sigma) = 1 - e^{\left(-\frac{\sigma}{\sigma_0}\right)^m} \quad (4.1)$$

Where $P(\sigma)$, in the range of [0, 1], is the failure probability of single fiber under an applied stress less than or equal to σ . ' σ_0 ' is a characteristic value of stress σ at which 63% of the population of specimens have failed (also known as *alpha* (α) - characteristic life) and m is the Weibull modulus (also known as *beta* (β) - shape parameter) which describes the variability of the failure strengths. The common values for ' m ' of fibers range from 2 to 20 (Mahesh et al., 1999). A high weibull modulus is desirable as it indicates better predictable failure behavior. Stress, σ , is simply obtained from the experimental results, while there are several probability estimators also known as ranking methods (ASTM Standard C1239-13, 2013) available in the literature (Bergman, 1984). The most common probability estimators for brittle failure with small sample size can all be written in the form (Bergman, 1984):

$$P = \frac{i-0.5}{n} \quad (4.2)$$

where i denotes that it is i^{th} , sample, while n represents the sample size. Taking natural log on the both sides of the Eq. (4.1), results in:

$$Y_i = \ln \left(\ln \left\{ \frac{1}{1-P(\sigma)} \right\} \right) \quad (4.3)$$

$$X_i = \ln(\sigma_i) \quad (4.4)$$

$$C = -m \ln(\sigma_0) \quad (4.5)$$

$$Y_i = mX_i + C \quad (4.6)$$

As shown in Eq. (4.6), the Weibull distribution function is transformed into a linear relationship. A linear plot between X_i and Y_i , is termed as Weibull probability plot (WPP). If the correlation coefficient of the plot is close to 1, the strength distribution can use the two parameter weibull distribution function. Fig.4.5 and Fig.4.6 show WPP and weibullplot, respectively, for glass fibers used. The correlation coefficient is 0.9, which is closed to 1 as required. Fig.4.5 is used for estimating parameters m and C .

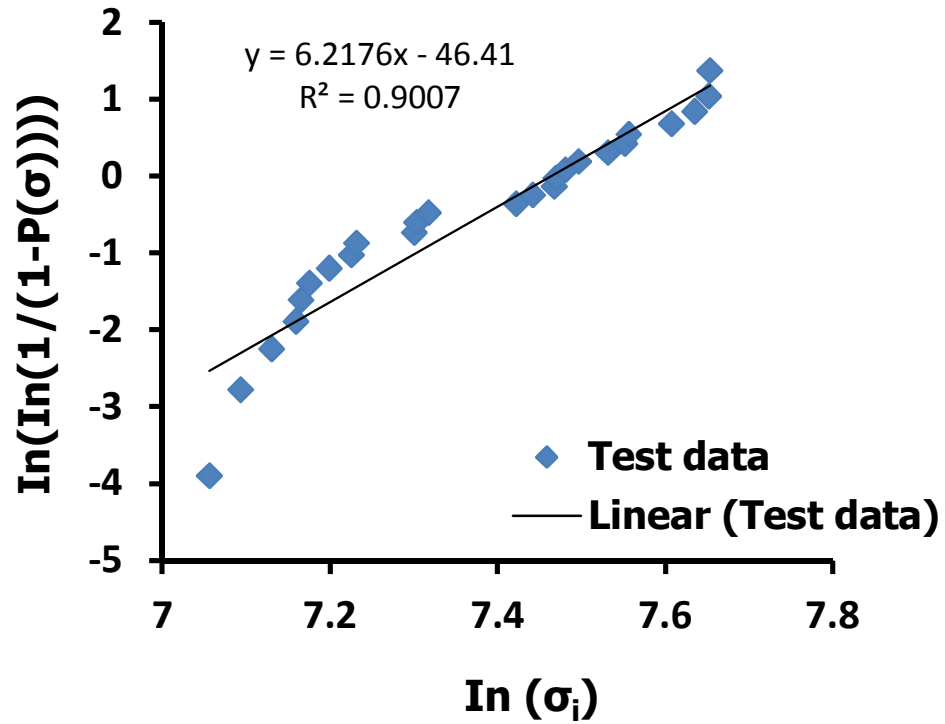


Figure 4.5 WPP for tensile strength of the glass fibers

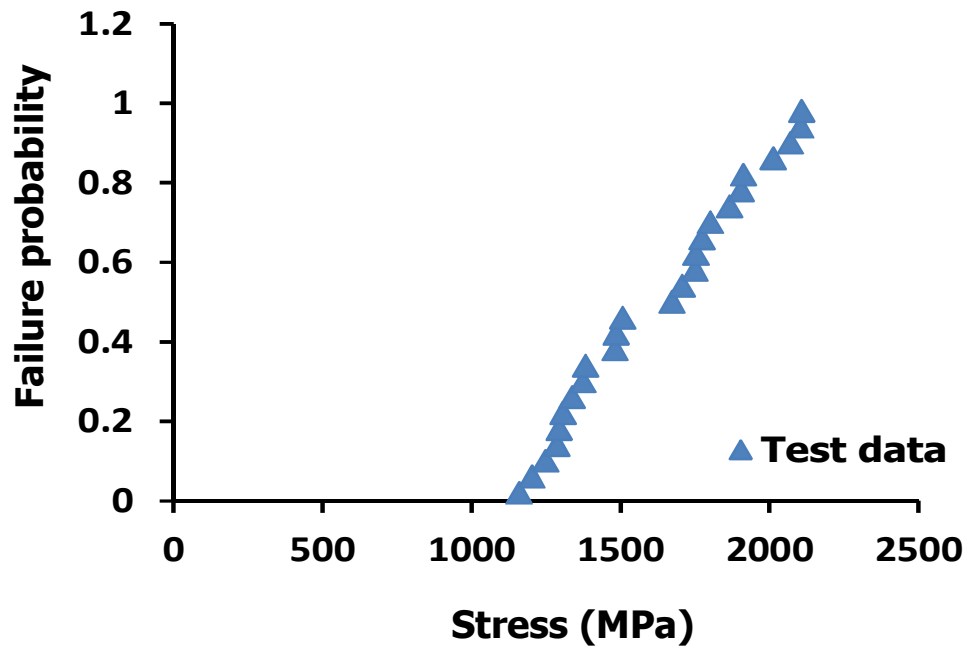


Figure 4.6 Weibull plot (Appendix-II)

From Fig.4.5, we get $m=6.217$ and $\sigma_0= 1745.85$ MPa.

The Weibull distribution has an expected value (or mean value) of tensile strength is given by(Hao et al., 2012):

$$\sigma_m = \sigma_0 \Gamma\left(1 + \frac{1}{m}\right) \quad (4.7)$$

where Γ is the gamma function. Using parameters m , σ_0 into the Eq. (4.7), mean value of the tensile strength is 1623.3 MPa. The measured average value is 1621 MPa. The deviation is only 0.14%, the precision is high from the perspective of reliability design. Therefore it is concluded that the tensile strength of the glass fibers can be expressed by the two parameter Weibull distribution. Maximum principal failure criterion is conventionally used for capturing the failure of brittle materials. Therefore, maximum principal stress criterion is used for failure of glass fibers in the modeling M^2RVE .

4.3.2 Matrix failure

The epoxy matrix (EPOFINE-556) has been assumed to behave as an isotropic, elastic-plastic solid following the Mohr-Coulomb yield criterion. Mohr-Coulomb yield criterion has been explained in section 3.2.4.

4.3.3 Fiber-matrix interface failure

The progressive fiber-matrix interfacial decohesion has been simulated using standard cohesive surface elements in ABAQUS Standard[®] as shown in Fig.3.6. The values of traction and interfacial fracture energy are 30 MPa and 100 J/m². Justification and details about implementation of failure traction-separation law for fiber-matrix debonding has been explained in section 3.2.5.

4.3.4 Delamination between plies failure

The damage behavior of the delamination layer has been simulated using traction-separation law which relates force acting on the interface to the displacement across it. The progressive delamination between plies has been simulated by using a thin layer of COH3D6 cohesive elements. In the absence of any damage, the interface behavior was assumed to be linear with an initial stiffness equal to the stiffness of the matrix material i.e., 4.7GPa. This is because it has been observed experimentally that thin layer between two layers of laminae consists of matrix material. Also, in case of cross ply laminate fiber bridging effect can be neglected (Shokrieh and Heidari-Rarani, 2011). For complete definition of damage behavior traction and fracture

toughness (i.e., critical energy release rate) is essential. To determine traction and fracture energy sophisticated experiments are required to be performed. To avoid experiments parametric study have been performed to elaborate effect of traction of the material response under delamination dominated type of loading as elaborated in the later section of the paper. For the fracture energy value of 100 J/m² has been used throughout the simulations. It is a reasonable value of mode-I fracture energy for glass fiber/epoxy material system (Crossman et al, 1980; Sela and Ishai, 1989; Cantwell and Morton, 1991; Benzeggagh and Kenane, 1996; Kenane M, Benzeggagh, 1997). To ensure the value of fracture energy is reasonable, a parametric study has been performed to see effect of fracture energy on the stress strain response keeping traction values same. It has been found that there is no or negligible effect of fracture energy on the out-of-plane stress strain response. Therefore, fracture energy of 100 J/m² has been kept constant throughout the simulations. Damage initiation has been captured using quadratic nominal stress criterion expressed as (Abaqus, 2009):

$$\left\{ \frac{t_n}{t_n^0} \right\}^2 + \left\{ \frac{t_s}{t_s^0} \right\}^2 + \left\{ \frac{t_t}{t_t^0} \right\}^2 = 1 \quad (4.8)$$

Where t_n , t_s and t_t are normal and tangential stress in one direction and tangential stress in another direction respectively. t_n is considered as positive all the time, as compressive stress doesn't cause the opening of the crack. t_n^0 , t_s^0 and t_t^0 are normal and tangential strength in one direction and tangential another direction respectively. Normal strength of the delamination layer has been assumed as equal to matrix tensile strength (i.e., 110 MPa). Adhesive strength of the delamination layer is varied above and below 30 MPa (closed to in-plane shear strength of the matrix material i.e., 40 MPa) to study its effect on overall material response. Fiber bridging effect has been assumed to neglected.

4.4 Model validation

Experimental data was not available in the literature for the epoxy/fiber combination used in the model; therefore, experiments were conducted on glass fiber-epoxy laminate specimens. The proposed M²RVE model has been validated against these experimental results.

4.4.1 Specimen manufacture for experiments

The edges of the laminate were removed and rectangular specimens (25 x 250 mm²) were cut from the [0/90] laminate according to ASTM standard D3039 (ASTM D3039/D3039M–08, 2008) as shown in Fig. 4.7. A strain gauge (gauge length of 6 mm) was mounted at the center of the specimen as shown in Fig. 4.7. A calibrated electronic strain indicator was used to note the strain developed in the strain gauge during loading of the specimen.

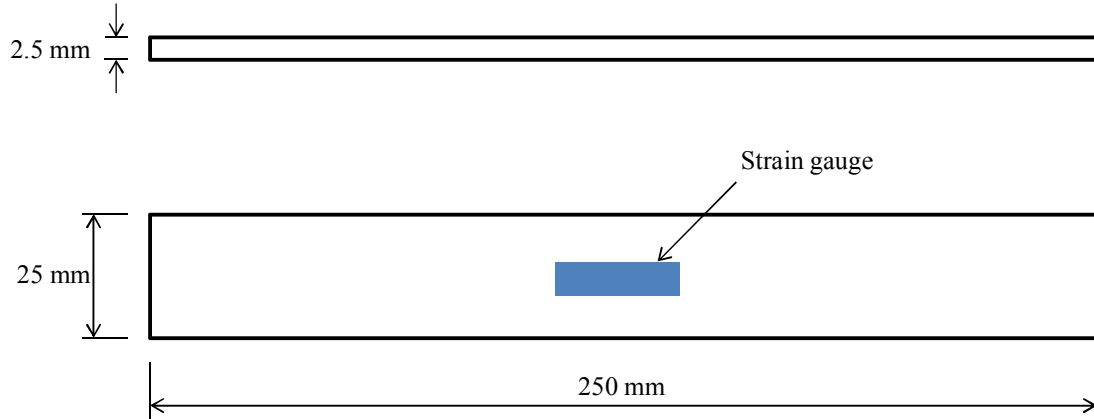


Figure 4.7 Specimen dimensions in-plane tensile loading tests

4.4.2 Experimental Results

In-plane tensile strength tests were carried out for the E-glass/epoxy [0/90] laminates as per ASTM 3039 (ASTM D3039/D3039M–08, 2008). The specimens were tested in tension using *LS 100 plus* universal testing machine by *LLOYD* instruments under stroke control and at a constant cross-head speed of 1mm/min. The applied load was measured simultaneously with a 100kN load cell. The corresponding tensile strain, ϵ_{12} , was noted, using strain gauge mounted on the specimen. The in-plane tensile stress-strain curve, up to 2.5% strain, is plotted in Fig. 4.8 for [0/90] laminates.

4.4.3 Global stress-strain response

The proposed M²RVE is subjected to in-plane tensile loading with periodic boundary conditions as explained in Section 3.2. The analysis has been performed using Rik's algorithm for non-linear analysis in ABAQUS Standard[®]. At the end of each load step in the non-linear analysis, volume average stresses and strains for [0/90]_n laminate obtained by using Eqs. (3.5) and (3.6), are plotted along with the experimental response as shown in Fig. 4.8. The initial region of the stress-strain curve is perfectly matching with experimental results up to a tensile strain of

approximately 0.6%. Beyond this point simulation results over predicts stress as compared with experimental response. The failure strength predicted by the simulation is ~14% higher than the failure strength found experimentally. This error can be attributed to the automated incremental checking of the fiber failure criterion by the finite element code. Ideally, when the maximum principal stress in the any element in the fiber material is greater than 1623 MPa then the element is considered to have failed and the stiffness of the particular element is reduced significantly (>90%). Due to automatic steps, stresses in the fibers shoots beyond 1623 MPa before the failure criterion is checked in the subsequent step. Therefore, the failure in the fibers doesn't takes place exactly at 1623 MPa, but slightly higher than 1623 MPa. Failure strain predicted by simulation is almost equal to the failure strain predicted by experiments. Fiber-matrix interface properties used for model validation as well as in the simulations (specified otherwise) are strength = 30 MPa, stiffness= 35 GPa/m and fracture energy = 100 J/m². Delamination layer material properties are strength= 30 MPa, stiffness= 4.7 GPa (same as matrix material) and fracture energy= 100 J/m². To address the sensitivity of these properties, the effect of these parameters on the material response has been characterized later in the work.

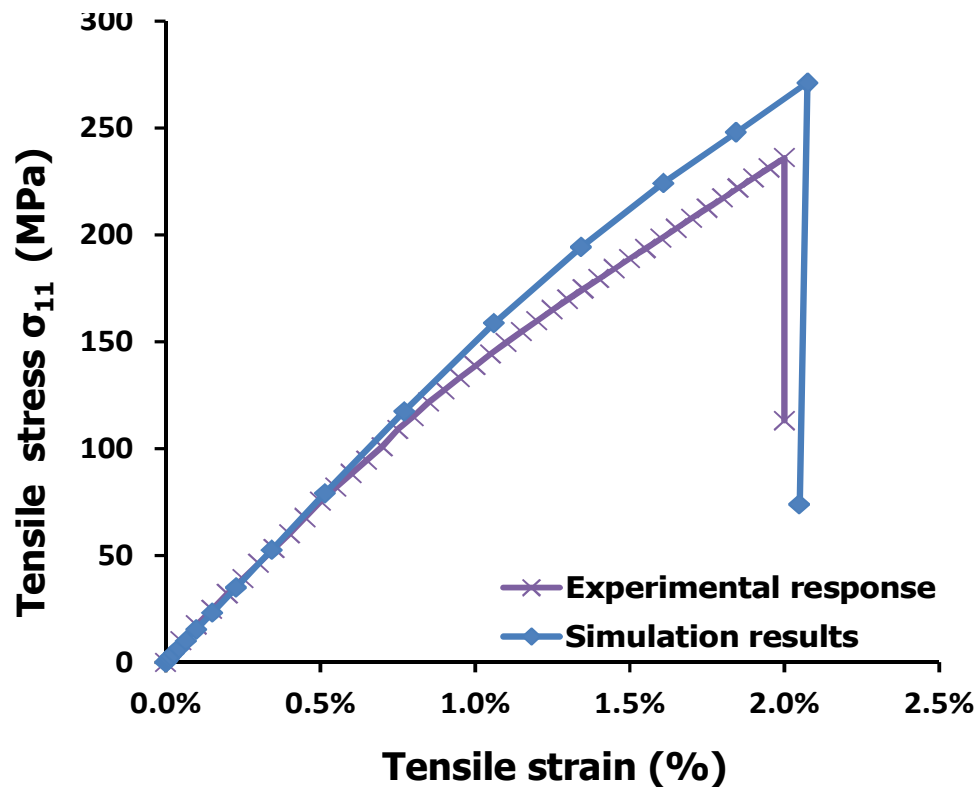


Figure 4.8 In-plane tensile stress-strain response of M²RVE for [0/90]_n laminate

4.5 Study of damage evolution mechanisms

The damage evolution study has been conducted for different scenarios, such as damage evolution with predominantly tensile failure mechanism; matrix and interface damage; interfacial and interlaminar decohesion; and damage evolution with tensile failure along with interfacial and interlaminar decohesion. .

4.5.1 Tensile failure dominated damage mechanism

It has been identified that in-plane tensile loading leads to a fiber failure, which the predominant mechanism is causing the failure of the laminate. To simulate in-plane tensile loading, M^2RVE is subjected to displacement in direction 1 as shown in Fig. 4.2(a). To capture fiber failure, Fortran[®] based user subroutine ‘USDFLD’ has been used (Appendix-I). Maximum principal stress developed in each element of the E-glass fiber material is called by using another user subroutine ‘GETVRM’. The stress developed in each element of the E-glass fiber material is then compared with the average failure stress obtained from Weibull distribution (1623 MPa). If the stress developed in any element is more than 1623 MPa, a stiffness of the particular element is degraded significantly (>90%). The top and bottom lamina are referred as 0° (along the applied displacement) and 90° (perpendicular to the applied displacement), respectively.

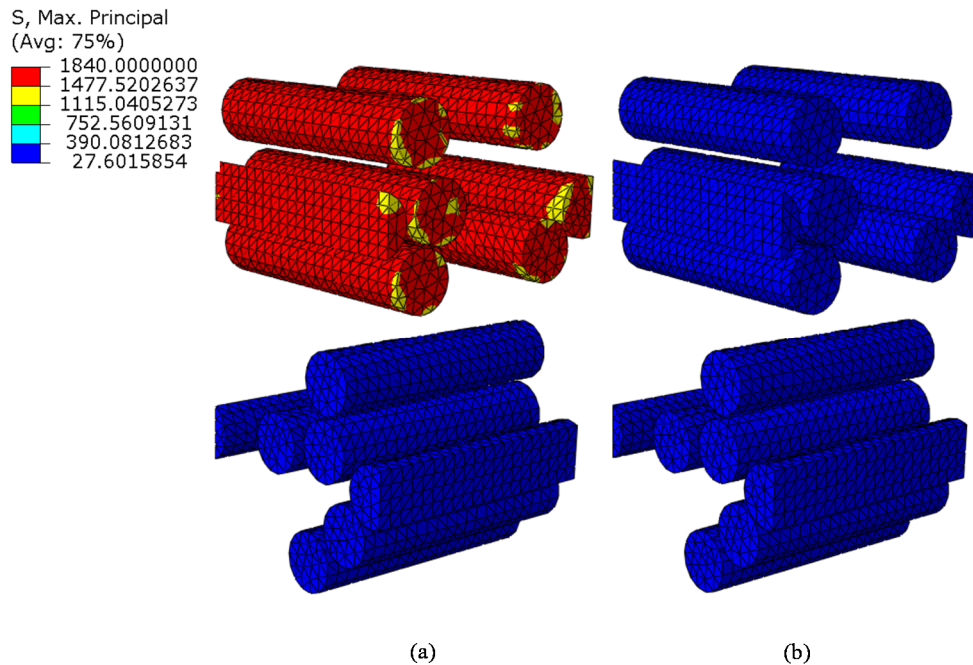


Figure 4.9 Maximum principal stress in the E-glass fibers (a) Just before fiber failure (b) After fiber failure

It can be observed in Fig. 4.9 (a) that all the fibers in 0° lamina fail where the loading is in-line with the fiber if the applied stress exceeds 1623 MPa. As shown previously in Fig. 4.8, the M^2RVE also captures the global stress-strain response with reasonable accuracy. Figs. 4.9(a) and (b) show the contours of maximum principal stresses developed in fibers prior to the onset of failure and post failure, respectively. Fig 4.9(b) shows that stresses in the fibers are an order of magnitude lower than the stresses prior to the onset of failure.

It is expected that most of the load in tension is borne by the fibers but it is important to characterize the material response of the matrix under tensile loading to estimate its contribution during tensile loading. The matrix friction angle is varied between 5° to 15° and the corresponding cohesive strength of the matrix is between 41 MPa to 48.8 MPa to see the effect of these properties on the global response. It can be observed from Fig. 4.10 that there is no effect of change in matrix properties on the global stress strain response.

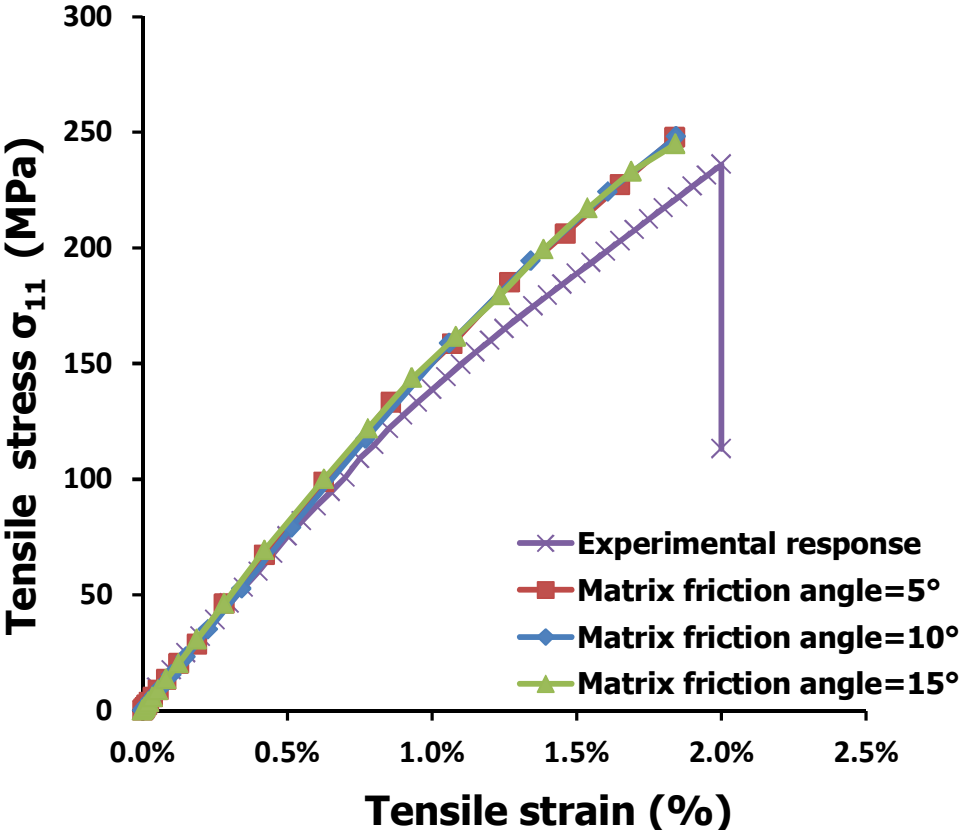


Figure 4.10 Effect of matrix friction angle on the stress-strain response of M^2RVE for $[0/90]_n$ laminate subjected to in-plane tensile loading

Similarly, in order to study the effect of fiber-matrix interfacial and interlaminar properties, a parametric study has been performed. Fig. 4.11 shows global stress-strain response of the $[0/90]_n$ laminate for in-plane tensile loading for different strengths and stiffness of the interfacial layer between fiber and matrix material against the experimental response. Cohesive strength of the interfacial material has been varied from 5 MPa to 90 MPa while the stiffness of the cohesive strength is kept as 35 GPa/m.

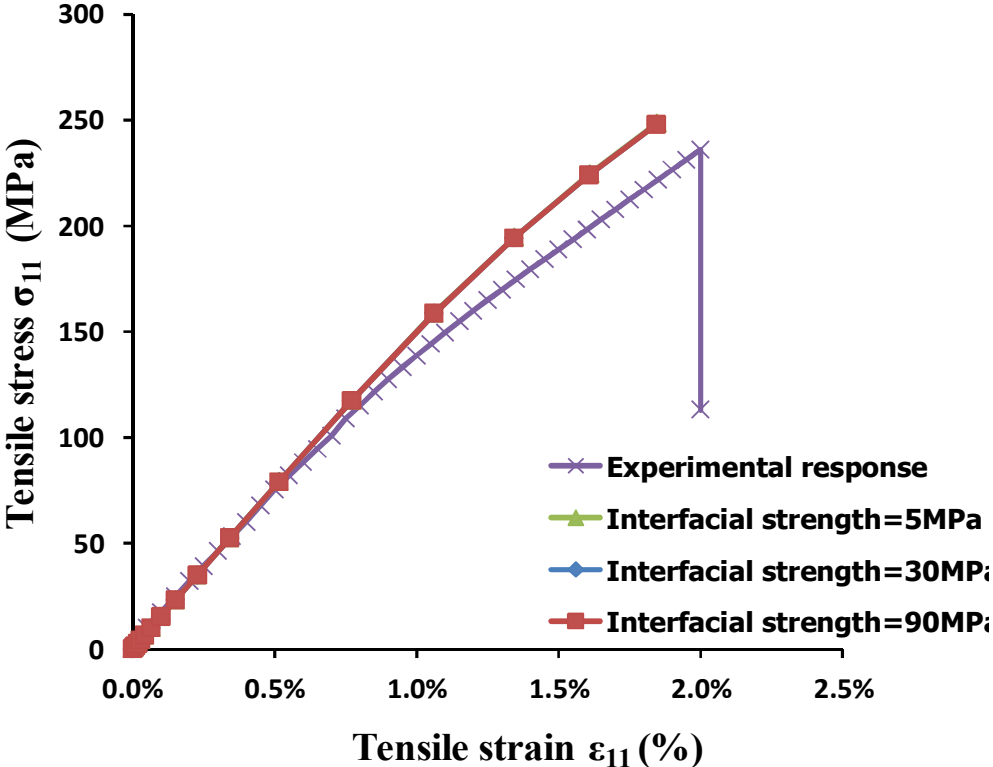


Figure 4.11 Effect of fiber-matrix interfacial properties on the stress-strain response of M^2RVE for $[0/90]_n$ laminate subjected to in-plane tensile loading

Fig. 4.12 shows global stress-strain response of the $[0/90]_n$ laminate for in-plane tensile loading for different strengths of the delamination layer between 0° lamina and 90° lamina. It is been found that there is no effect of properties of the delamination layer between two laminae on the global stress strain response for in-plane tensile loading. QUADSCRT (Quadratic nominal stress damage initiation criterion for cohesive elements) variable shows if the initiation criterion is satisfied or not. If the variable is 1.0 in an element then the initiation criterion is satisfied. It was observed that QUADSCRT variable did not exhibit initiation of decohesion even till fiber failure,

irrespective of the strength of the delamination layer. Based on these results, it can be inferred that fiber failure is the dominant mechanism and other modes of failures are inappreciable.

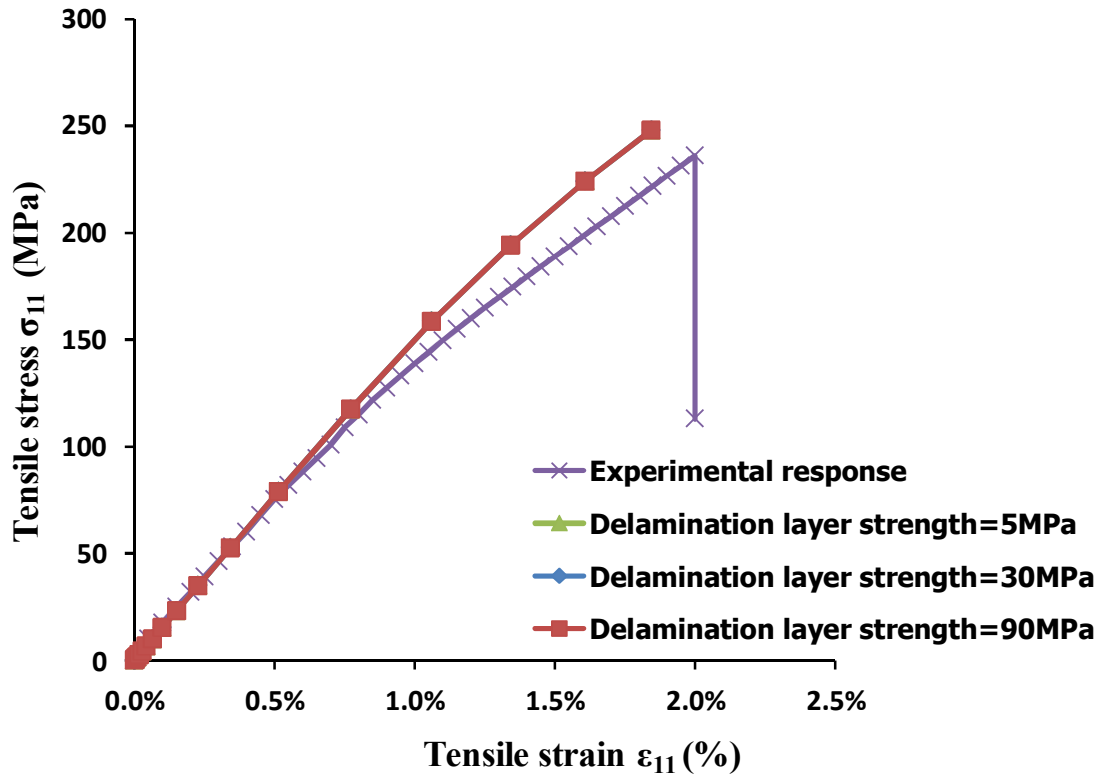


Figure 4.12 Effect of delamination layer properties on the stress-strain response of M^2RVE for $[0/90]_n$ laminate subjected to in-plane tensile loading

4.5.2 Matrix and interface dominated failure mechanism

In order to study matrix damage and fiber-matrix interfacial failure simultaneously in-plane shear loading has been identified as shown in Fig. 4.2(b). The M^2RVE has been subjected to 4% shear strain, as experimental results are available up to 4% shear strain. The maximum principal stresses developed in the E-glass fibers at 4% shear strain are much less than 1623 MPa, therefore, no element in the fiber experiences the failure. The mean of the maximum principal stresses is about ~ 300 MPa which indicates that fiber failure can be ignored in in-plane shear loading.

It has already been demonstrated in chapter 3 that matrix material properties affect the global stress strain response. Fig. 3.15 shows the volume averaged in-plane shear stress-strain response of the M^2RVE along with the experimental response. It can be observed that simulated response is in good agreement with the experimental response. The matrix friction angle is varied between 5° and 15° in increments of 5° as shown in Fig. 3.19. As expected, it can be observed that with

an increase in the friction angle and, hence the matrix cohesive strength, there is an increase of up to 17% in shear stresses if the friction angle is increased from 5° to 15°

It can be observed in Fig. 3.21 that global response gets significantly affected by the interface properties as well. The shear strength of the material for an interfacial strength of 5 MPa is $\sim 36\%$ lower than the shear strength for the material with an interfacial strength of 30 MPa. Any further increase in the interfacial strength does not affect the global shear stress-strain response. Similar to the tensile loading, the onset of interlaminar decohesion does not occur, however, the magnitude of QUADSCRT is higher for in-plane shear loading as compared to the tensile loading indicating that the interlaminar traction is higher for in-plane shear. Since, decohesion does not initiate the effect of delamination on the global stress-strain response is negligible. Therefore results are same as in section 3.5 for $[0/90]$ laminate.

4.5.3 Interfacial and interlaminar decohesion driven failure mechanism

The previous two conditions do not exhibit any sensitivity to the interlaminar decohesion (delamination). To demonstrate interfacial failure between fiber-matrix and delamination between layers can be effectively captured by M^2RVE , out-of-plane shear loading has been applied as shown in Fig. 4.2(c). Note that this loading condition is extremely difficult to implement physically, consequently, only simulation results are available. However, as described previously, M^2RVE has been found to be reasonably accurate for different loading conditions, it is expected that it can capture the response of complex loading conditions which are difficult to realize.

The interfacial strength and stiffness are kept as 30 MPa and 35 GPa/m, respectively (as used in case of in-plane tensile loading and in-plane shear loading). Delamination layer strength and stiffness are kept as 30 MPa and 4.7 GPa, respectively. The stiffness of the interlaminar layer is considered to be same as that of the matrix. The material response obtained from the above mentioned parameters is used as a baseline for comparing the parameter sensitivity. Since the fiber failure primarily occurs in tension, it is expected that the fiber failure is unlikely to occur. The maximum principal stresses are much below (<1000 MPa) the fiber failure limit of 1623 MPa. In addition, the effect of sensitivity of the matrix damage parameters has not been observed on the out-of-plane shear stress-strain response.

In order to study effect of interfacial layer between fiber and matrix, strength of the interfacial layer is varied from 5 MPa to 60 MPa, keeping the stiffness of interfacial layer as 35 GPa/m. Fig. 4.13 shows that the effect of the interfacial strength on the material response is significant and the out-of-plane shear stresses increase by 28% if the interfacial strength increases from 5 MPa to 30 MPa. As mentioned previously, any additional increase does not improve the material response.

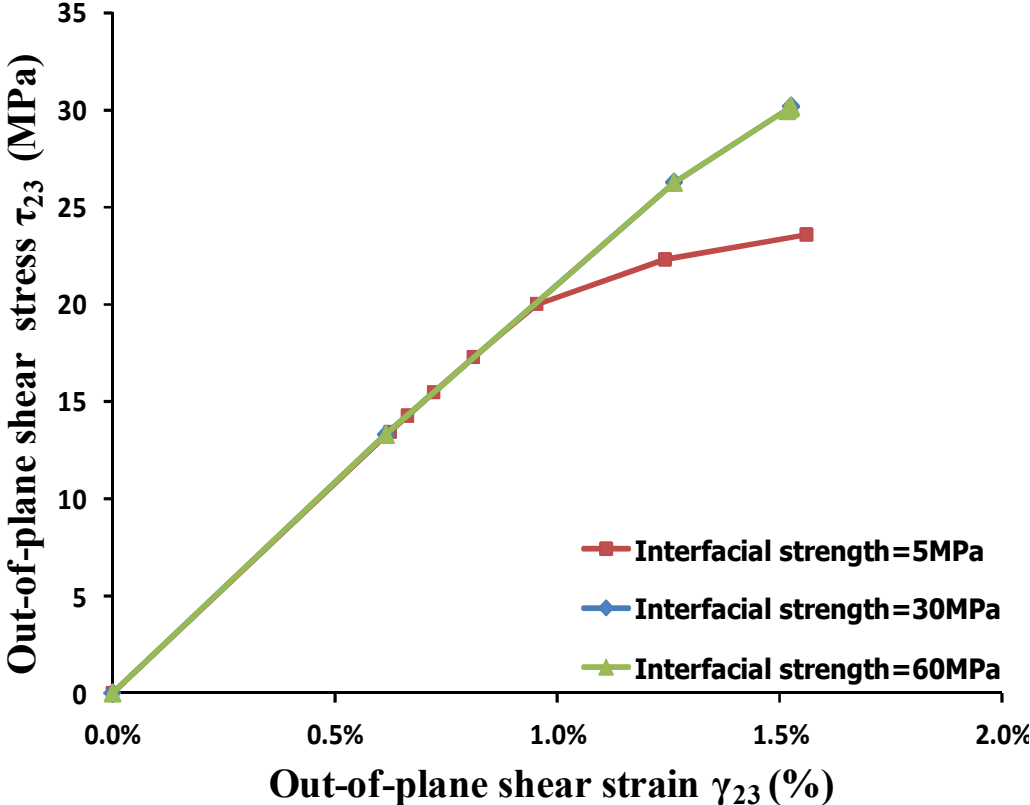


Figure 4.13 Effect of fiber-matrix interfacial properties on the stress-strain response of M^2RVE for $[0/90]_n$ laminate subjected to out-of-plane shear loading

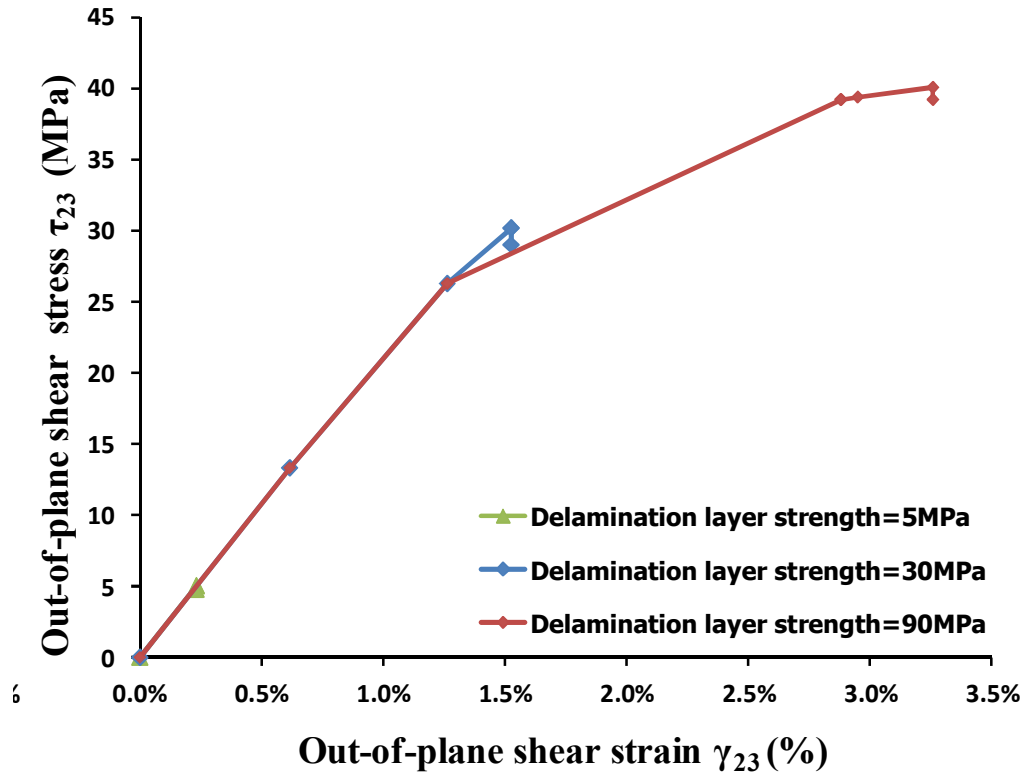


Figure 4.14 Effect of delamination layer properties on the stress-strain response of M^2RVE for $[0/90]_n$ laminate subjected to out-of-plane shear loading

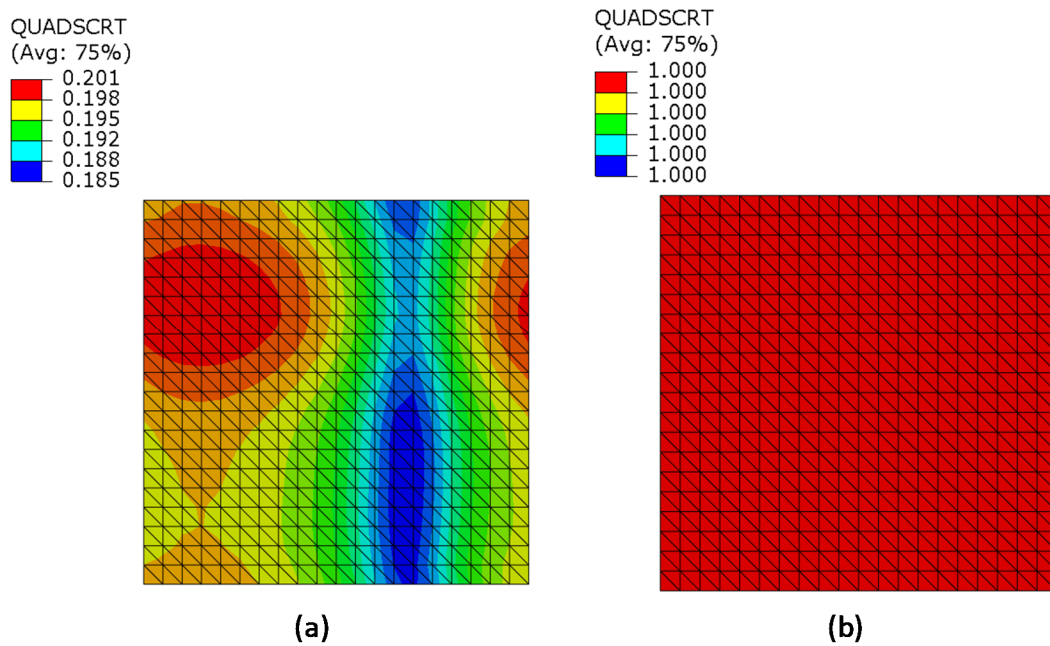


Figure 4.15 QUADSCRT for delamination layer strength (a) 90MPa (b) 5 MPa at 1.5% out-of-plane shear strain

To study delamination between 0° ply and 90° ply, strength of the delamination layer has been varied from 5 MPa to 90 MPa keeping stiffness equal to 4.7 GPa. It is observed that there is failure of the laminate at 1.5%, when delamination layer strength is less than 30 MPa. In case the strength of delamination layer is 90 MPa, laminate failure takes place at ~3.2% out-of-plane shear strain as shown in Fig. 4.14.

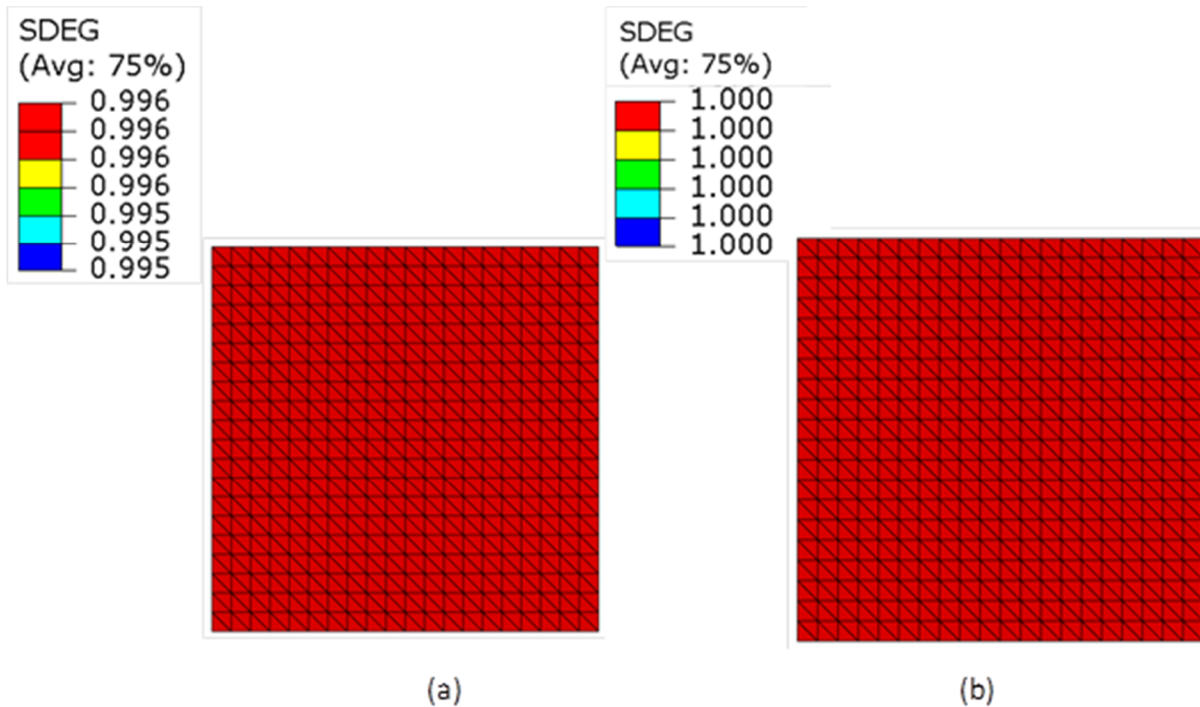


Figure 4.16 SDEG for delamination layer strength of 5 MPa at 1.5% out-of-plane shear strain
(a) just before failure (b) after failure

The contour plot of variable QUADSCRT (see Fig.4.15) shows that the complete damage in delamination layer takes place if the delamination layer strength equal to 5 MPa. However, if the delamination layer strength equal to 90 MPa, the damage is avoided and the interlaminar decohesion does not occur till 3.2% as shown in Fig. 4.15. Complete failure of the cohesive elements in the delamination layer takes place at 1.5% shear strain when delamination layer strength of 5MPa has been used as shown in Fig. 4.16.

4.5.4 Combined failure driven by fiber damage, fiber-matrix debonding and interlaminar decohesion

In order to demonstrate capability of M²RVE to capture multiple (more than two) failure mechanisms simultaneously, a multi-axial complex loading shown in Fig. 4.2(d) is applied. It is a

combination of in-plane tensile loading and out-of-plane shear loading. The applied displacement in case of in-plane tensile loading and out-of-plane shear loading is maintained at a ratio of 1:12 ($\delta t/\delta s= 1/12$) to avoid predominant tensile failure. Fig. 4.17 shows contour plot of the principal stresses developed in the E-glass fibers. In this case fibers in 0° lamina take entire load and it can be observed that the stresses in fibers reduced drastically after fiber failure criterion is reached as shown in Fig. 4.17 (b).

To study the effect of complex loading on epoxy matrix damage, matrix friction angle has been varied between 5° till 15° as shown in Fig. 4.18. It can be observed that failure of the composite takes place at 0.6% tensile strain, which is ~70% less as compared with the failure strain when pure in-plane tensile loading is been applied. The tensile stress at fiber failure is ~105MPa which is significantly low as compared with pure in-plane tensile loading. In case of out-of-plane shear loading response, failure strain is ~1.5%, which is same as in case of pure out-of-plane shear loading. The shear stress at failure is also same as compared to pure out-of-plane shear loading. Unlike pure out-of-plane shear response, there is no discernable variation in shear response when combined loading is used for different matrix friction angles as shown in Fig. 4.18.

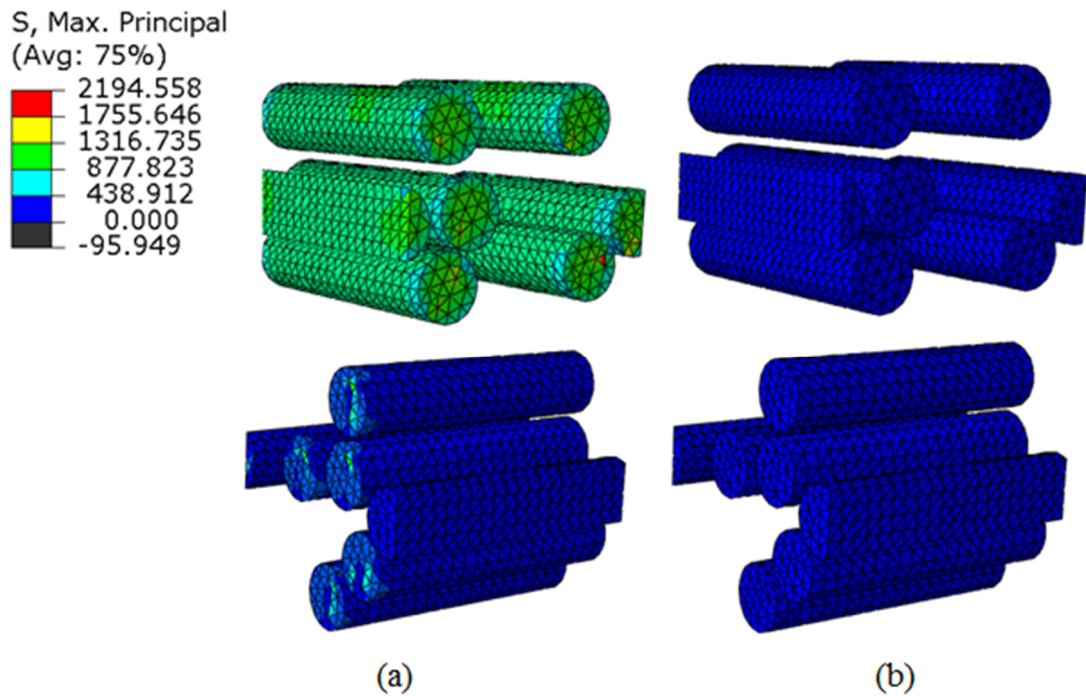


Figure 4.17 Maximum principal stress in the E-glass fibers at 0.6% of in-plane tensile strain and at 1.5% out-of-plane shear strain (a) before fiber failure (b) after fiber failure

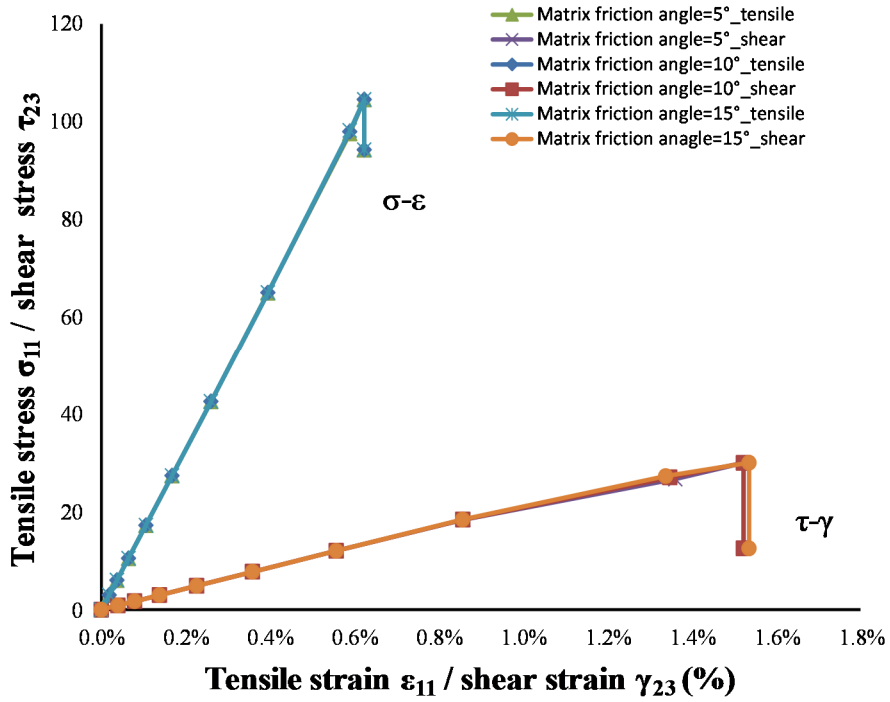


Figure 4.18 Effect of matrix friction angle on the stress-strain response of M²RVE for [0/90]_n laminate subjected to in-plane tensile loading and out-of-plane shear loading

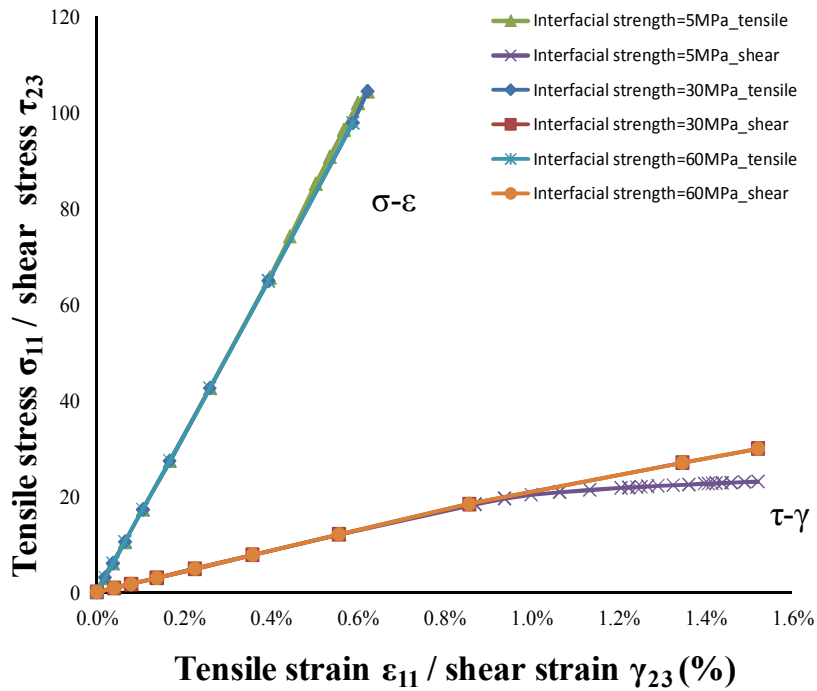


Figure 4.19 Effect of fiber-matrix interfacial properties on the stress-strain response of M²RVE for [0/90]_n laminate subjected to in-plane tensile loading and out-of-plane shear loading

Fig.4.19 shows combined loading material response for different interfacial material properties. It can be observed that there is no effect of the variation of interfacial properties on fiber failure. However, out-of-plane shear strength is lower if the interfacial strength is less than 30 MPa. There is no effect of changing interfacial strength on the material response beyond 30 MPa.

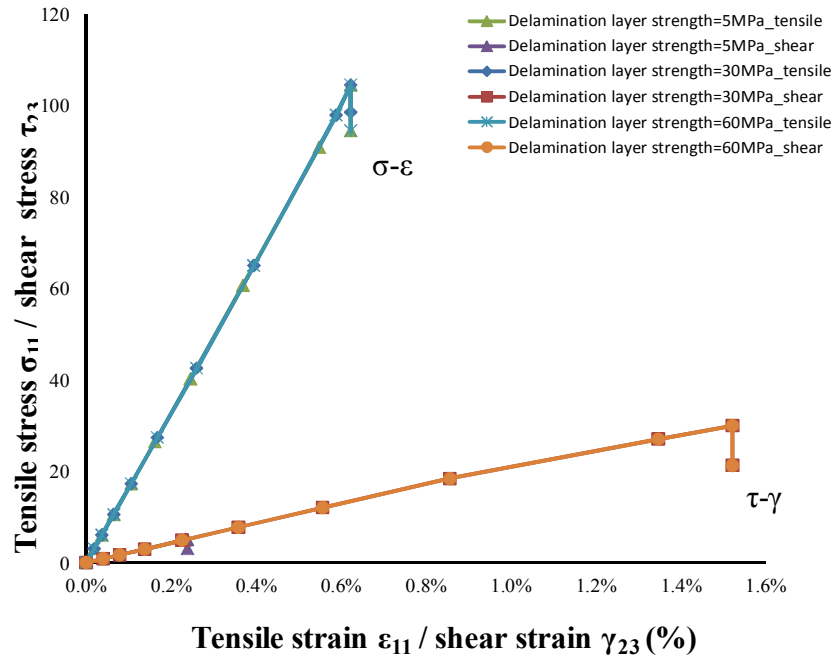


Figure 4.20 Effect of delamination layer properties on the stress-strain response of M²RVE for [0/90]_n laminate subjected to out-of-plane shear loading

To study effect of delamination layer properties on the material response, strength of the delamination layer has been varied between 5MPa to 60 MPa, keeping the stiffness at 4.7 GPa. It is observed that there is no effect of this change on the fiber failure, however, the composite failure takes place at much lower stress and strain (5 MPa and 0.2%) for the delamination layer strength of 5 MPa. It has been observed in Fig. 4.14 that failure takes place at 30 MPa and 1.5% shear strain in case of pure out-of-plane shear loading for delamination layer strength of 5MPa whereas the failure takes place at much lower out-of-plane stress and strain values in case of combined loading for a delamination layer strength of 5MPa as shown in Fig.4. 20.

It can be observed that decohesion has not started in case of delamination layer strength of 60 MPa and 1.5% shear strain as shown in Fig. 4.21 (a). However, decohesion has initiated in case of delamination layer strength of 5 MPa at 1.5% shear strain as shown in Fig.4.21 (b).

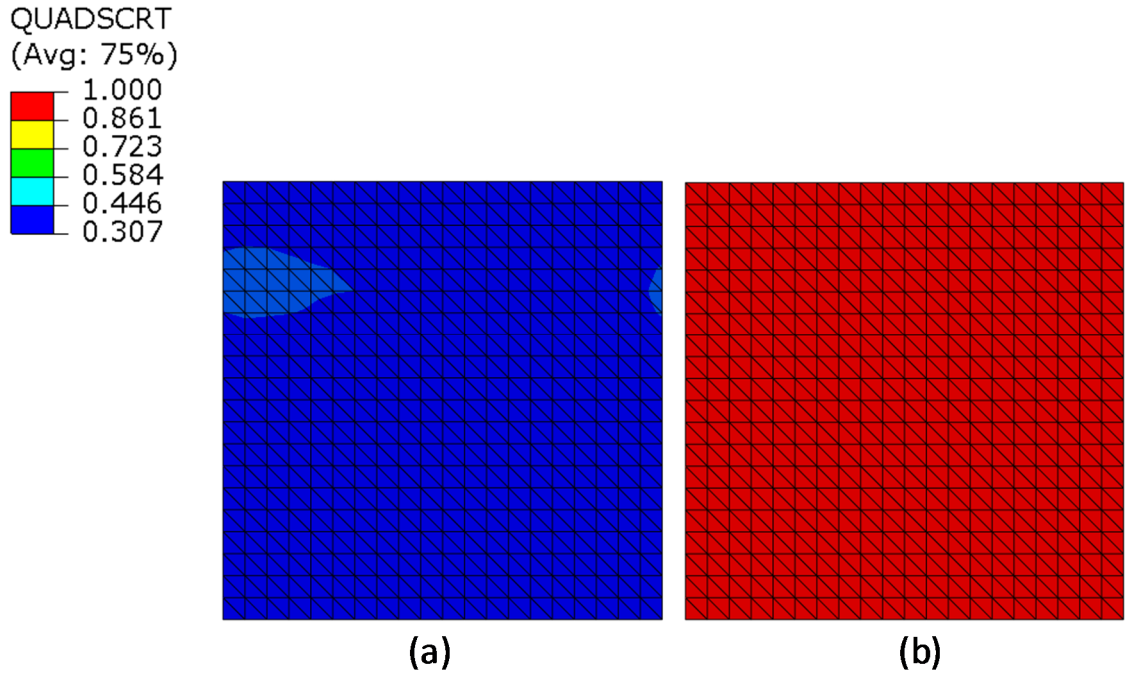


Figure 4.21 QUADSCRT for delamination layer strength (a) 60MPa (b) 5 MPa at 1.5% out-of-plane shear strain

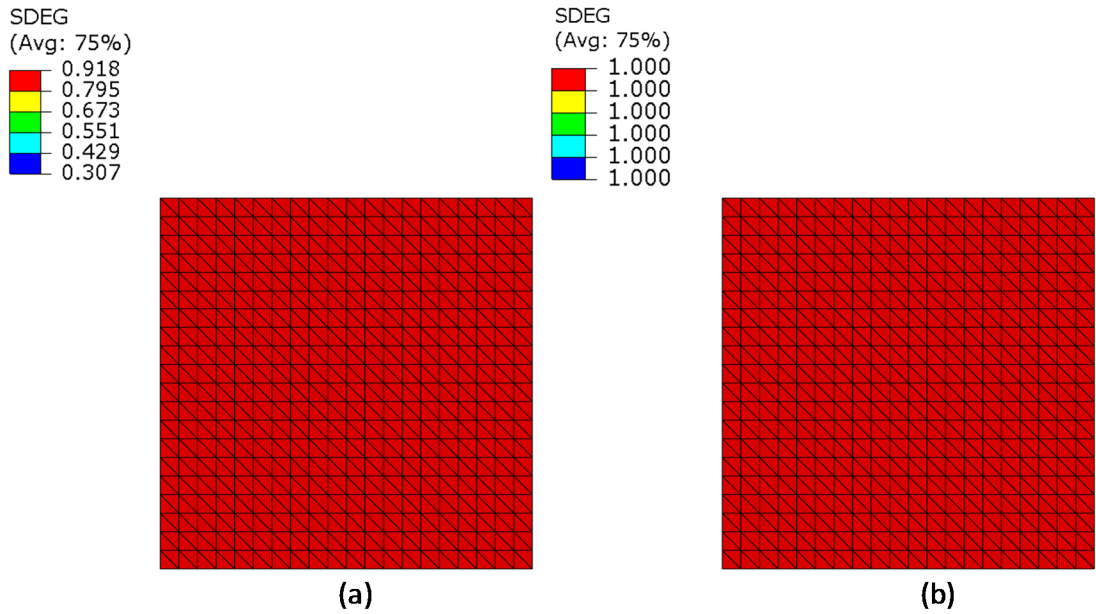


Figure 4.22 SDEG for delamination layer strength of 5 MPa at 0.2% out-of-plane shear strain (a) just before failure (b) after failure

Fig.4.22 (a) and Fig.4.22 (b) shows contour plot of variable SDEG just before failure and after failure, respectively for delamination layer strength of 5 MPa at 0.2% out-of-plane shear strain. It

can be observed that all the cohesive elements have fail leading to complete failure of the laminate.

4.6 Summary

The chapter presented an improved multi-layer multi-fiber representative volume element (M^2RVE) to predict global as well as local stress-strain material response for all possible intra/inter ply failure mechanisms under complex multi-axial loading. The results show that this strategy is able to accurately reproduce the physical fracture mechanisms experimentally observed. It was observed that in case of in-plane tensile loading, fibers along with loading direction takes maximum load, and fiber failure is the dominant failure mechanism. It was observed that in the presence of multi-axial loading, fiber failure takes place at much lower in-plane tensile load. Note that this approach can be very useful in damage prediction under complex loading which is difficult to implement experimentally. One of the important limitations of the M^2RVE method is assumption of periodicity. The next chapter presents a methodology for prediction of local stresses in the hot spots in non-periodic structures with geometric discontinuities.

Chapter 5: Micro-macro approach for damage prediction in non-periodic structures

5.1 Introduction

It is known that the material failure often occurs due to stress concentration. The M^2RVE approach discussed in Chapter 3 and Chapter 4 is not suitable to determine micro-stresses distribution in the areas involving stress concentration, e.g., free-edges, interfaces etc., as the periodic boundary conditions are no longer applicable. Modeling different regions with different approach can be used to handle this issue. To determine the severity of the stress concentration and possible failure consequences, it is important to investigate the micro-stress distribution in the area involving stress concentration. The most discernible approach of studying damage at the microscopic level is to carry out a full-scale microscopic analysis of the structure by explicitly modeling all the heterogeneities. A direct consequence of inclusion of the microstructural details in the whole structure is the inevitable complexity and massive computational cost. In order to reduce computational cost and to study the microscale behavior of composites, various multiscale/multi-level methods are used, as illustrated in Fig. 5.1.

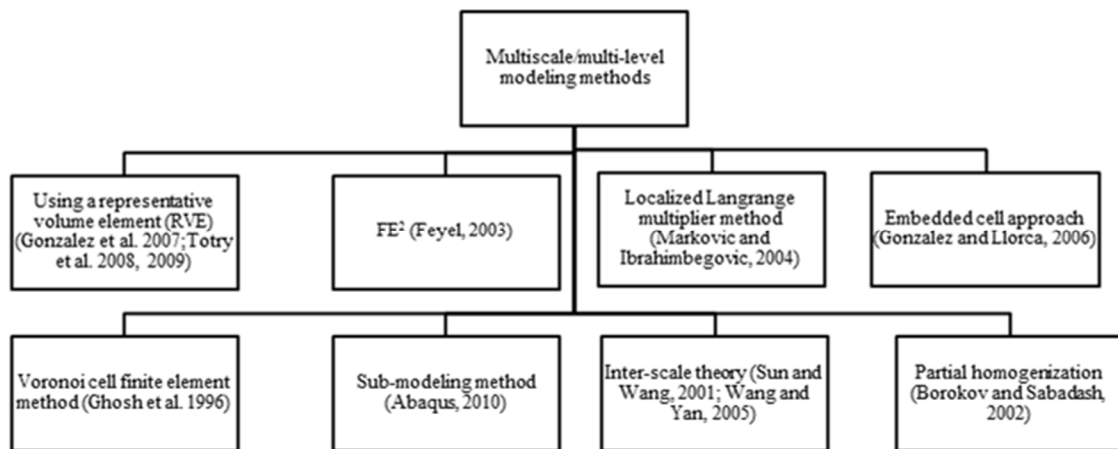


Figure 5.1 Multi-level and multiscale methods in literature

In this Chapter, an attempt has been made to formulate a multiscale modeling approach which can address the limitations of the existing modeling approaches mentioned earlier and can be utilized to predict damage mechanisms in the regions of high stress concentrations. The ideas of

homogenization and de-homogenization by Wang and Yan (2005) have been extended and combined with the idea of partial homogenization provided by Borokov and Sabadash (2002) for the formulation of the micro-macro approach. The micro-macro method however extends this idea to inelastic deformation while it was restricted to only linear deformations in the previous studies. Following Borokov and Sabadash (2002), microscale and macroscale are coupled as a single domain and analyzed simultaneously in the micro-macro approach. The microstructure is enriched with all the details like fibers, interface etc. The use of partial homogenization leads to less computations as compared to multiscale methods described in (Ghosh et al. 1995; Feyel, 2003; Markovic and Ibrahimbegovic, 2004; Gonzalez and Llorca, 2006; Totry et al. 2008). The limitations of the works in (Sun and Wang, 2001; Wang and Yan, 2005) are also addressed, since the microstructural solution remains accurate even at the boundaries of the microdomain. The details of the formulation of the scheme and its application for investigating damage mechanisms in regions near a notch root are outlined in the following sections.

5.2 Formulation of the micro-macro approach based on the locality principle

The locality principle states that the effect of homogenization of the structure does not influence the homogenized part farther than the characteristic length of the structure. Typically, the characteristic length is of the order of the unit cell containing a single fiber (Borokov and Sabadash, 2002). This principle can be used to model the microstructure in the region of interest and the remaining area could use homogenized or effective properties.

In order to confirm that the proposed micro-macro methodology based locality principle is valid; a prediction of localized damage in the composite via a micro-macro analysis is compared with a full-scale microstructural analysis. The damage in the epoxy matrix is modeled using Mohr-Coulomb plasticity and the accumulated plastic strain is taken as a measure of the damage. Fig. 5.2(a) shows a randomly distributed fiber array consisting of 25 fibers which are surrounded by the matrix material. It also shows the center fibers around which the accumulated damage in the matrix is captured. Fig. 5.2(b) shows the corresponding partially homogenized lamina as per the proposed micro-macro scheme. Fig. 5.2(c) shows the mesh geometry of the micro-macro analysis. A shear load in X-Y plane is applied on the lamina as shown in Fig. 5.2(b). Fig. 5.3 shows the damage in the epoxy matrix versus the volume averaged shear strain in the localized

region of interest for three different approaches, viz., complete microstructural modeling, sub-modeling and micro-macro. The two-step sub modeling approach has been used to predict the localized damage and compared with the proposed micro-macro method. In sub-modeling macro scale model analysis is performed using effective properties of the composite laminate. Eventually, high stress region is modeled using fiber-matrix details and subjected to the displacement field obtained in previous step. Details about sub-modeling implementation can be found in ABAQUS[®] user manual. The solution time for the sub-modeling approach is double that of the micro-macro method since it requires two separate analyses (one at macro scale and another at micro scale). It can be seen that the micro-macro scheme prediction is in good agreement with the full-scale microstructural analysis and the two-step sub-modeling.

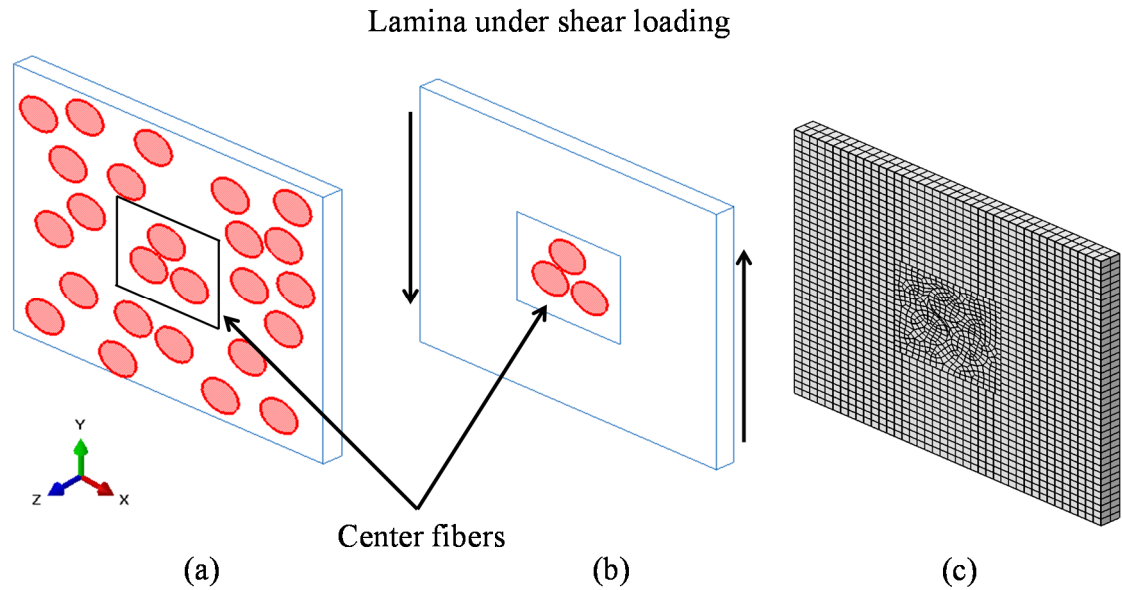


Figure 5.2 Geometry of the (a) lamina with complete microstructure (b) partially homogenized lamina with the applied shear loading (c) meshing of the partially homogenized lamina

Note that the micro-macro method evaluates the distribution of stresses in the macrostructural and the microstructural domains via a coupled concurrent analysis of both the domains. This method uses partial homogenization in which the region other than the area of interest (where the microstructure is explicitly modeled) is homogenized. The basic difference between conventional multi-level methods, i.e., inter-scale theory and the partial homogenization method is that the microstructural and macro-structural analyses are not performed simultaneously in the multi-level methods. On the other hand, in the partial homogenization method, the two length

scales are analyzed simultaneously. This leads to the required coupling of the two scales, eliminating the need for two separate analyses. In the proposed scheme, initially, a region of interest (or a local domain) is identified in the structure, which is typically the region of a stress concentration, free edges, crack tips etc. This region is modeled with the microstructure of the composite, that is, randomly distributed fibers in the matrix. The rest of the structure is modeled as a homogeneous continuum with effective properties. Strong kinematic coupling is incorporated between the local domain and the homogeneous continuum. This modified structure, that is, the original structure along with the modified local domain is then solved and the required micro-stresses in the region of interest are obtained. Fig 5.3 shows comparison of material response obtained from complete microscale analysis, sub-modeling method and proposed micro-macro method..

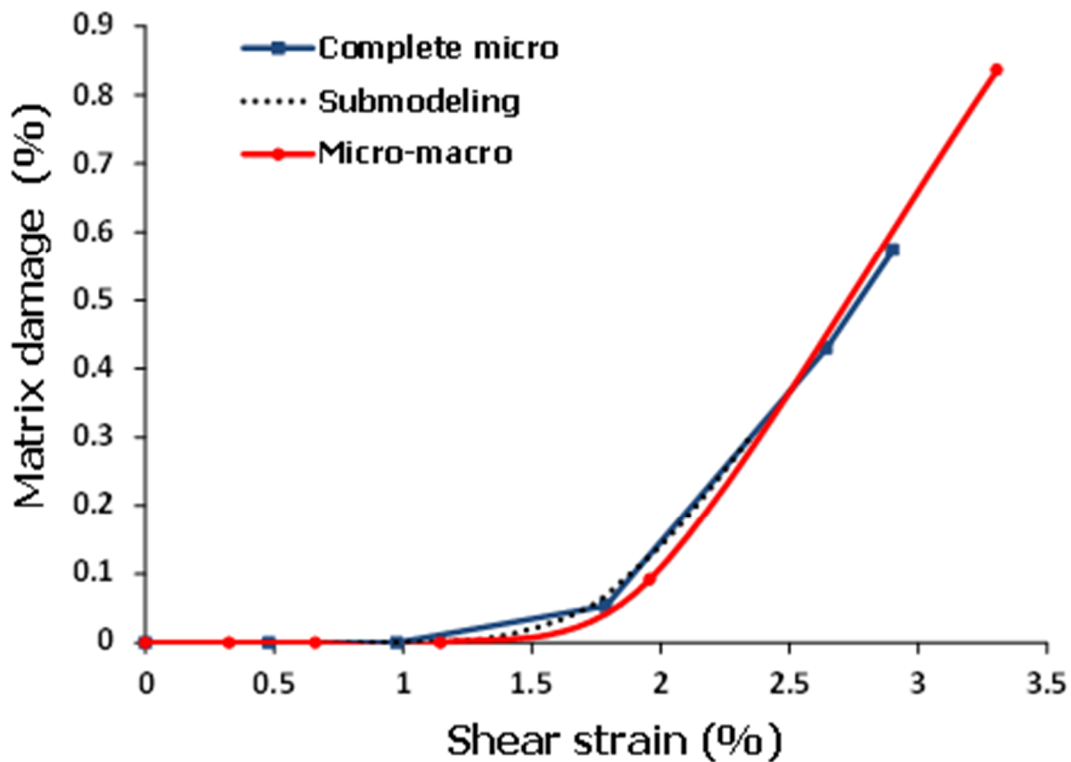


Figure 5.3 Comparison between full scale microstructural response and response predicted by micro-macro scheme and sub-modeling method

Note here that the most of the multi-level models reported in the literature assume elastic homogenized properties for the macro-domain (Sun and Wang, 2001; Wang and Yan, 2005). The global response for non-homogenous strain rate cannot be studied via this approach; ply-level

failure can be incorporated by using quadratic failure criterion, such as Hashin's and Tsai-Hill criteria. Consequently, some form of macro-level failure can be incorporated.

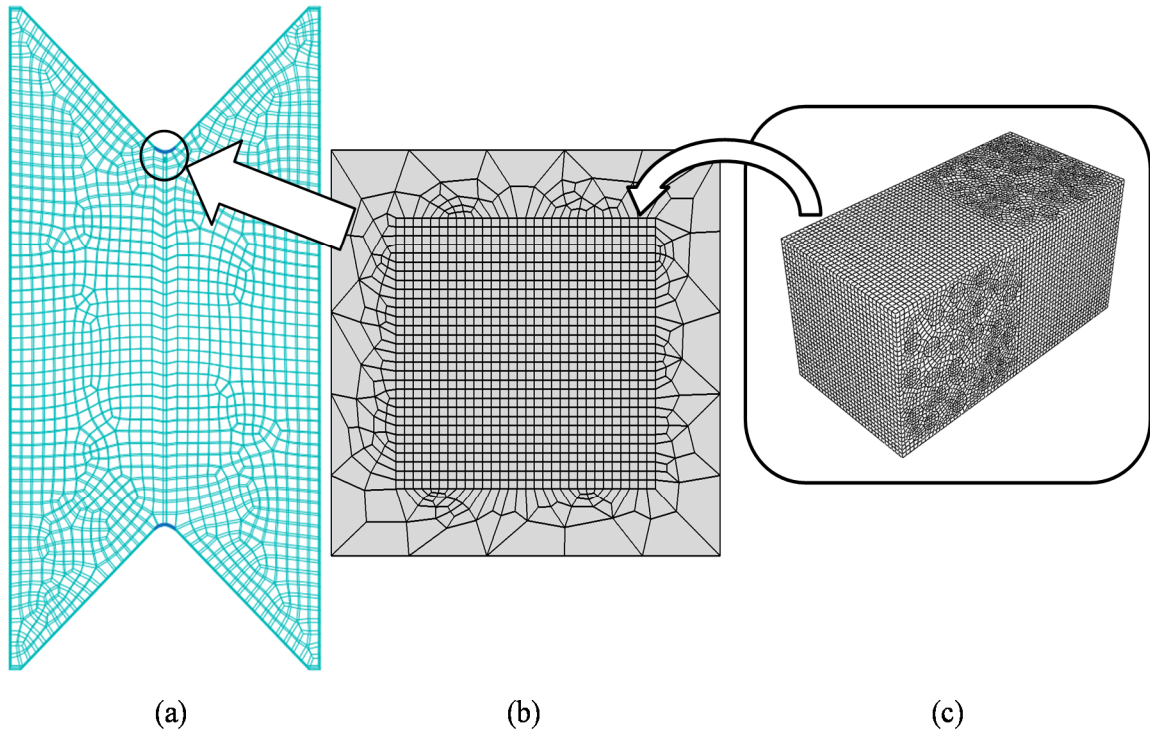


Figure 5.4 Proposed micro-macro approach

The micro-macro approach described here (Fig 5.4) will be used in the following sections for developing a model to analyze the damage behavior of the specimen used in V-notched rail shear test (ASTM D7078/D7078M-05, 2000). In-plane loading was chosen for developing the model, since the damage mechanisms are fairly complex under shear. The model utilizes the Mohr-Coulomb criterion for simulating damage in the matrix, and a traction separation law for simulating fiber-matrix interface failure. Damage mechanisms in the stress concentration area near the notch root can be investigated and compared against the damage mechanisms away from the notch root as shown in Fig 5.4.

5.3 Finite element modeling

5.3.1 Model geometry

This scheme requires the modeling of both the microstructure and the macrostructure. The geometry of the structure is same as the geometry of the specimen used in the ASTM-D7078 standard (ASTM D7078/D7078M-05, 2000), as shown in Fig. 5.5(a). The [0/90] laminate specimen contains a double V-notch and a significant portion to either sides of the V-shaped notches is clamped tightly during the experiment and does not undergo deformation. Consequently, these sections are not included in the finite element model geometry to reduce the computational load. This can be seen in Fig. 5.5(b) which provides the details of the geometry of the structure used in the FE model. The microstructure consists of two cubical cells with fibers in one cell oriented orthogonally with respect to fibers in the other cell to represent a [0/90] laminate. Each cell contains randomly distributed glass fibers in the matrix with a fiber volume fraction of 28%. The fiber volume was measured as 28% post fabrication. Hence, the model used a volume fraction of 28% to corroborate the experimental response. However, this is not a limitation of the model. The fiber diameter is $24\ \mu\text{m}$ and 24 fibers are modeled within a cube of $0.2\ \text{mm}$ edge length. The remainder of the cube is composed of matrix material. The cohesive layer between the fiber and the matrix is modeled as a layer of cohesive elements with zero initial thickness. 8-noded 3D cohesive elements were used for meshing this layer in ABAQUS Standard[®]. The mesh is created by off-setting a layer of zero thickness from the mesh containing fiber and the matrix. The size of the cube can be determined by the volume required to capture all the relevant microstructural details. The detailed geometry of the microstructure is as shown in Fig. 5.6.

Fig. 5.7 shows a magnified view of the section of the structure which is cut by the plane of symmetry PQRS and contains the line AB. The position of the slot with reference to the structure is clearly illustrated by the cross sectional view of the slot in the plane PQRS. The slot is symmetric about the line AB and the plane PQRS. The dimensions of the slot are $0.2\ \text{mm} \times 0.2\ \text{mm} \times 0.4\ \text{mm}$. The microstructure is placed in that region as shown in Fig. 5.7.

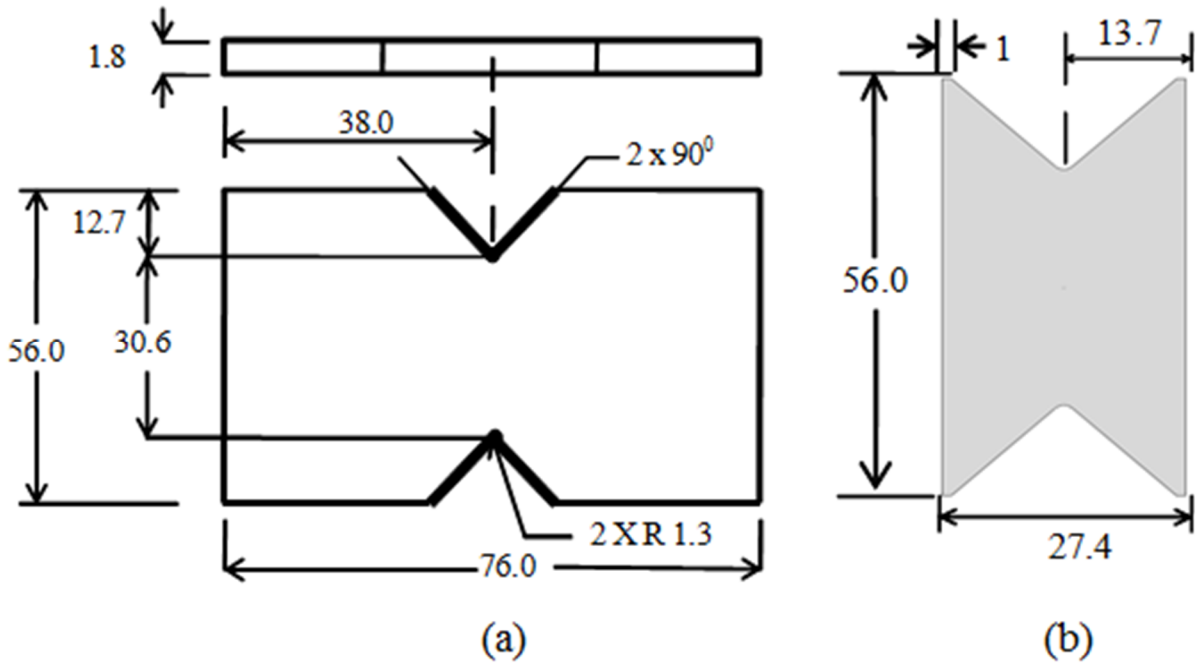


Figure 5.5 (a) Specimen geometry (b) model geometry

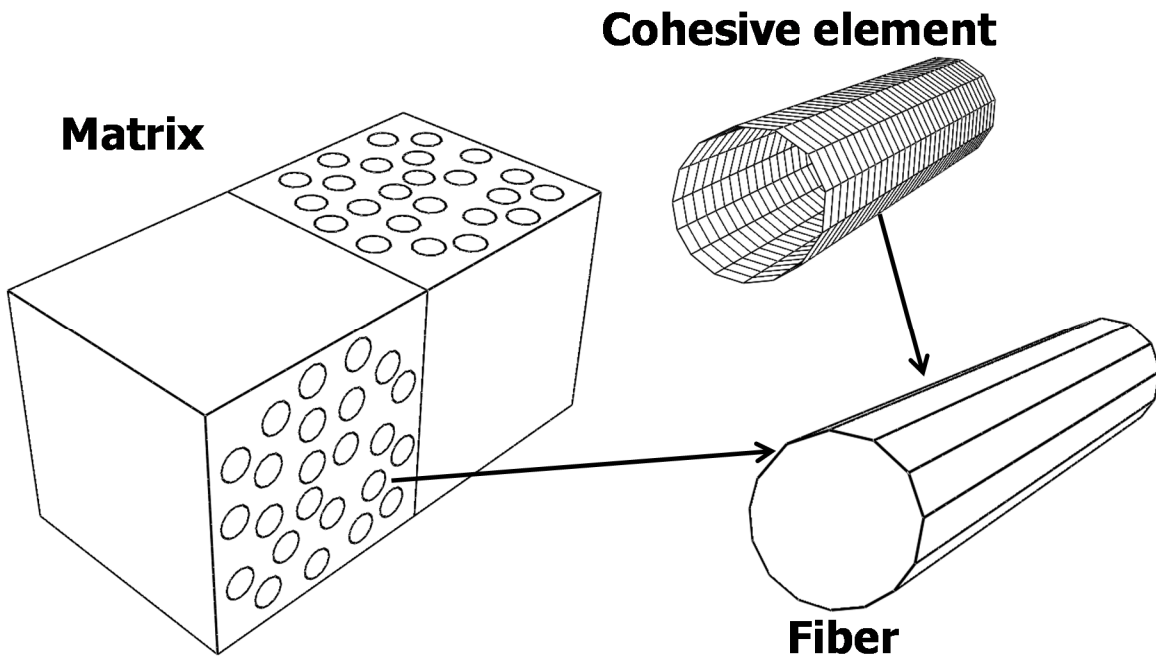


Figure 5.6 Geometry of the microstructural domain

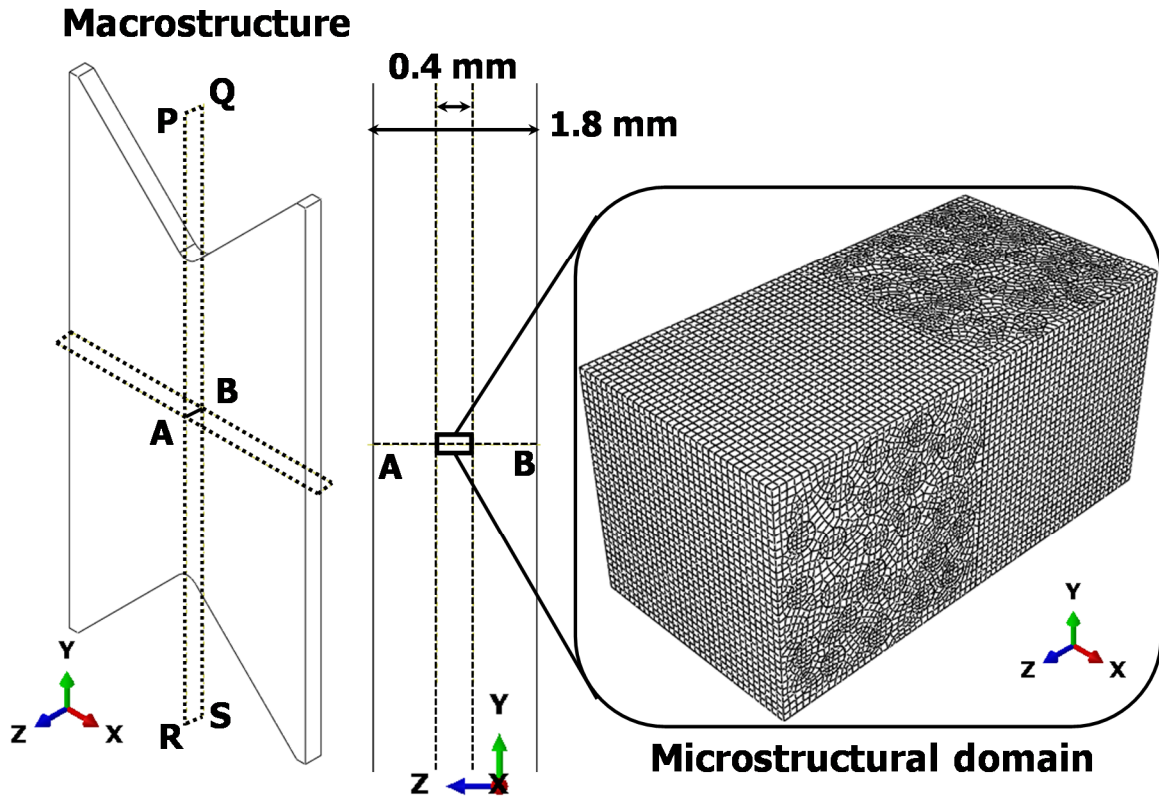


Figure 5.7 Geometry of the unified specimen and microstructure

5.3.2 Material and damage models

Each layer of the macrostructure is considered to be a homogeneous unidirectional elastic lamina under plane stress conditions and the stiffness values are provided in Table 5.1, obtained by using laminate theory. E-glass (ER-459L) fibers were modeled as linear elastic isotropic solids and their constants are given in Table 3.1.

Table 5.1 Elastic properties of the lamina

E_{11} (GPa)	E_{22} (GPa)	G_{12} (GPa)	Poisson's ratio, ν
23.8	6.368	2.2	0.2804

The plastic deformation is governed by the multi-axial Mohr-Coulomb criterion. Implementation of Mohr-Coulomb criterion is described in section 3.3.4. Standard traction separation law has been used for decohesion prediction as explained in section 3.3.4.

5.3.3 Boundary and contact conditions

The boundary conditions applied on the structure are illustrated in Fig. 5.8. Since the loading applied on the specimen is purely in-plane shear, the face ABPQ is fixed and U_x is set to zero on the opposite face DCRS. The structure is loaded by giving some arbitrary positive displacement δ_0 to face DCRS and setting U_y to δ_0 . Displacement controlled loading has been used such that the load carried by the structure decreases as the structure fails which allows for a slower rate of failure.

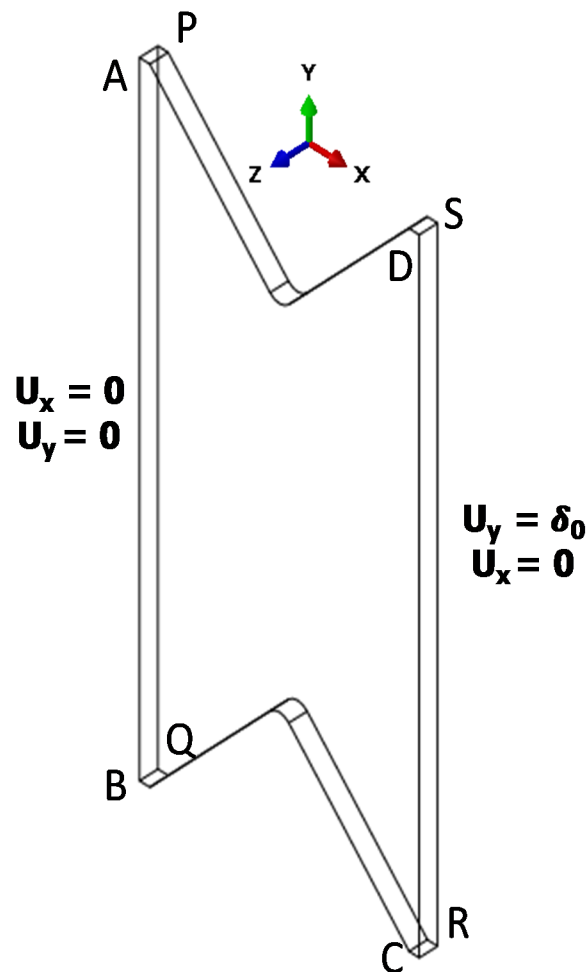


Figure 5.8 Boundary conditions on the finite element model for in-plane shear
Mesh size used for micro domain is much finer than the mesh size used for macro domain. Numbers of nodes on the surfaces of micro domain are much higher than then numbers of nodes on macro domain. Therefore, node merging was not possible. It is assumed that between micro-domain and macro domain displacements and rotations are continuous. To model continuity of

displacement (solid elements are used in present case) rigid contact between micro-domain and macro is provided. Rigid contact (TIED contact in ABAQUS[®]) ensures that displacements and rotations from one part will be transferred to the other part without alteration. Basically the rigid contact acts like a weld ensuring that the two parts acts like one unit. The constraint type used in this work is a surface-based tied constraint (ABAQUS, 2009), in which each node on the first surface (the slave surface) will have the same values for its degrees of freedom as the point on the second surface (the master surface) to which it is closest. The master surfaces are selected from the macrostructure geometry, whereas a corresponding slave surface is selected from the microstructure geometry.

5.4 Mesh sensitivity analysis

The mesh density around the microstructure affects the accuracy of the results obtained at the microstructural level. Fig.5.9 shows the mesh seeds around the microstructure which can be varied in number to achieve a finer mesh in the corresponding regions. The number of elements in the structural mesh was progressively increased to establish the convergence in the results, as shown in Fig. 5.10.

It can be clearly seen from Fig. 5.10 that the stress-strain curves converge when the mesh density around the microstructure is increased. The minimum number of mesh seeds required for the solution to converge is 30. Consequently, the simulations in this work were carried out by keeping the number of mesh seeds fixed at 30, as no appreciable improvements in the results have been observed by increasing meshdensity any further. SC8R continuum shell elements were used to discretize the macrostructure. C3D8R 3D solid elements were used for discretizing the fiber and the matrix. COH3D8 cohesive elements were used for the modeling of the fiber- matrix interface. A total number of 142526 elements and 157265 nodes have been used in the micro scale model.

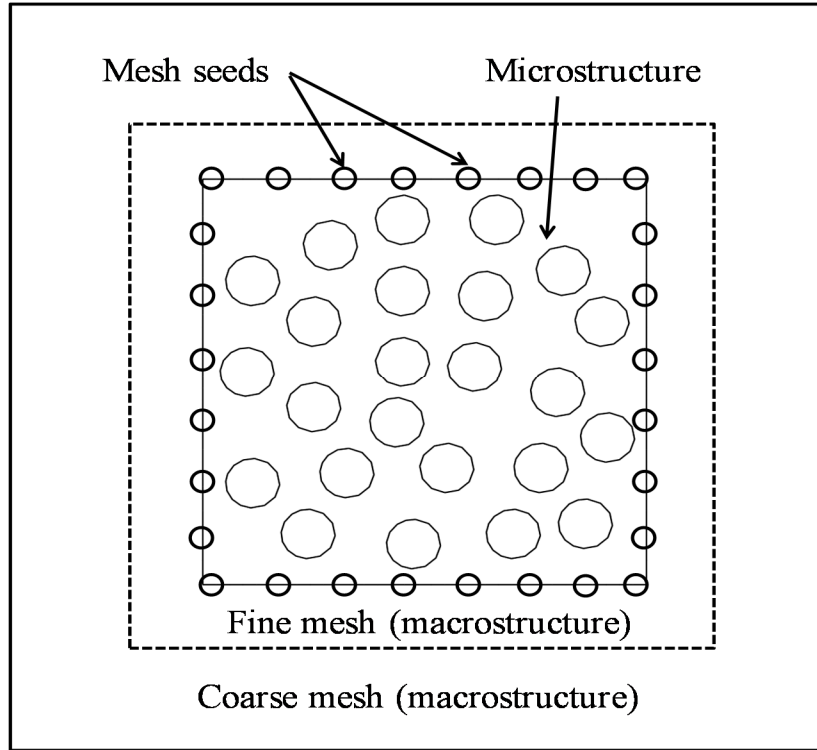


Figure 5.9 Mesh seeds in the microstructure

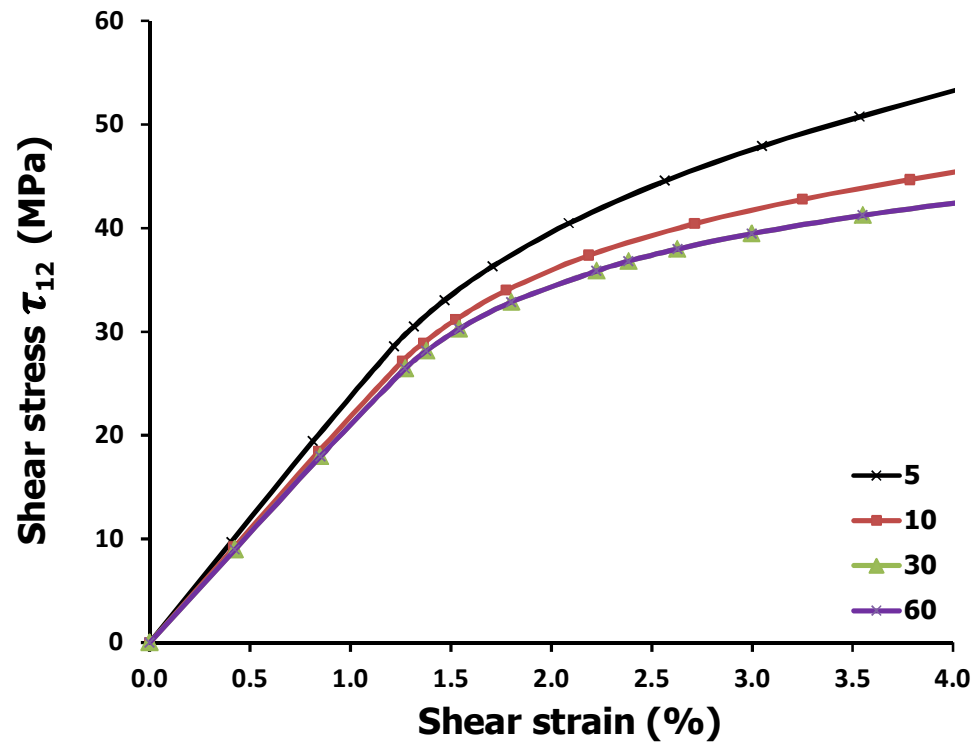


Figure 5.10 Mesh convergence achieved by varying the number of mesh seeds

5.5 Model validation

Throughout this section, τ_{12} and ϵ_{12} refer to the in-plane shear stress and in-plane shear strain averaged over the volume of the microstructure, unless mentioned otherwise. Volume averaged stresses and strains are determined by Eqs. (3.5) and (3.6). Since the strain gauges measure average strains over a relatively large area as compared with the micro-domain of micro-macro method, the experimental response depicts the average values of the strains averaged over a large area (5 mm \times 5 mm). In order to compare this experimental response with the micro-macro prediction where the size of the micro-domain is 0.2 mm³, it is assumed that strain fields are uniform over a small macroscopic region near the center. Consequently, the point based value obtained in the model should be equal to the average value obtained from the strain gauges. Fig. 5.11 shows that the shear response predicted by the micro-macro scheme plotted as τ_{12} vs ϵ_{12} is in good agreement with the experimental response as described in chapter 3. The curve showing experimental response illustrates the in-plane shear response of the rail shear specimen tested according to ASTM Standard D7078 (ASTM D7078/D7078M-05, 2000). For doing micro-macro simulations, the matrix friction angle, ϕ , and matrix cohesive strength, c , are determined as 10° and 44.7 MPa, respectively, from Eq. (5.3). The interface stiffness is chosen to be 10 GPa/mm, the interface strength as 30 MPa and the interface energy as 100 J/m². As shown in Fig. 5.11, the linear portion of both the predicted as well as experimental response extends up to 1.25% strain. The maximum prediction error is limited to about \sim 8%. The difference in the experimental response can be attributed to the assumptions in the model and errors in measurement and the variation in the properties of the constituents due to local defects and inhomogeneities. Once the matrix starts yielding, the response becomes non-linear in nature. The transition between the linear and the non-linear regimes is relatively smooth in the experimental data. However, the transition is more pronounced in the model and the non-linear response commences at a strain of 1.25%. This sudden transition could be explained by the initiation of matrix yielding. After model validation, a parametric study was performed to study the effect of various phases and interface properties on the stress-strain response of the microstructural domain.

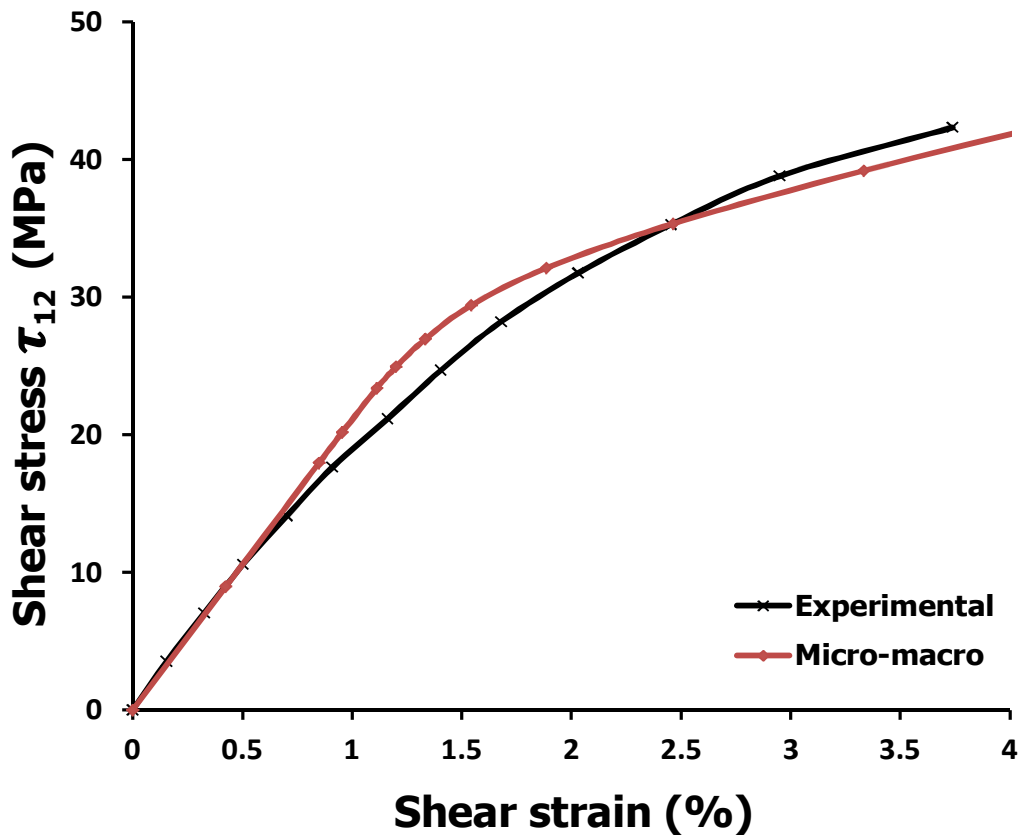


Figure 5.11 Comparison between experimental response and response predicted by micro-macro scheme

5.6 Effect of the phase and interface properties of the micro-domain

Interface and phase properties can affect the damage initiation and progression. This section is focused on quantifying the effects of interface and phase properties which can affect the damage response of the microstructural domain. It has been observed in chapter 3 that for the current material system (volume fraction and/or phase and interface properties) the effect of delamination is negligible on both local and global response. As a result, the effect of delamination was not explicitly considered in the present model. However, it can be easily implemented in the model for other loading conditions where delamination may be significant.

5.6.1 Effect of interface fracture energy

The effect of the variation of fracture energy is discussed in this section. The interface energy is a difficult quantity to measure experimentally and the values can vary within an order of

magnitude depending upon the test method. The values for the fracture energy reported in the literature lie anywhere between 1 J/m^2 and 100 J/m^2 (Griffiths, and Holloway, 1970). The proposed approach can potentially capture the effects of variations in the material properties which can be very useful for design purposes. One can estimate the variation in the local response for the lower and upper bounds of the interfacial energy and other parameters that can affect the interface damage and the matrix damage occurring in a local region. The fracture energy is determined by the relationship given in Eq. (3.11), which indicates the amount of energy released during the failure of the interface. The strength and the stiffness of the interface are kept constant with values equal to 30 MPa and 10 GPa/mm, respectively. The matrix friction angle ϕ is kept as 10° . It can be seen from Fig. 5.12 that increasing the fracture energy reduces the amount of interfacial damage at a particular strain value. At constant strength and stiffness, increasing the fracture energy increases the separation, δ , for the final fracture of the interface. Consequently, the completion of the debonding process (final separation) is delayed, which ensures high stress values at the same strain for higher fracture energy. Fig. 5.13 shows the contour plots of interface damage at 8% shear strain. The legend indicates the value of the variable, which detects the final fracture of the interface. The variable can take any value between zero and one. A value of less than one indicates that the damage has initiated, while a value of one indicates the completion of the debonding or decohesion process. It can be seen in Fig. 5.13 that the contour plot of the laminate with a fracture energy equal to 10 J/m^2 shows a significant amount of completely damaged interfaces; whereas, the laminate with fracture energy equal to 100 J/m^2 does not show complete fracture anywhere. This is an expected result (as discussed in this section) because the amount of interface damage decreases with increasing fracture energy.

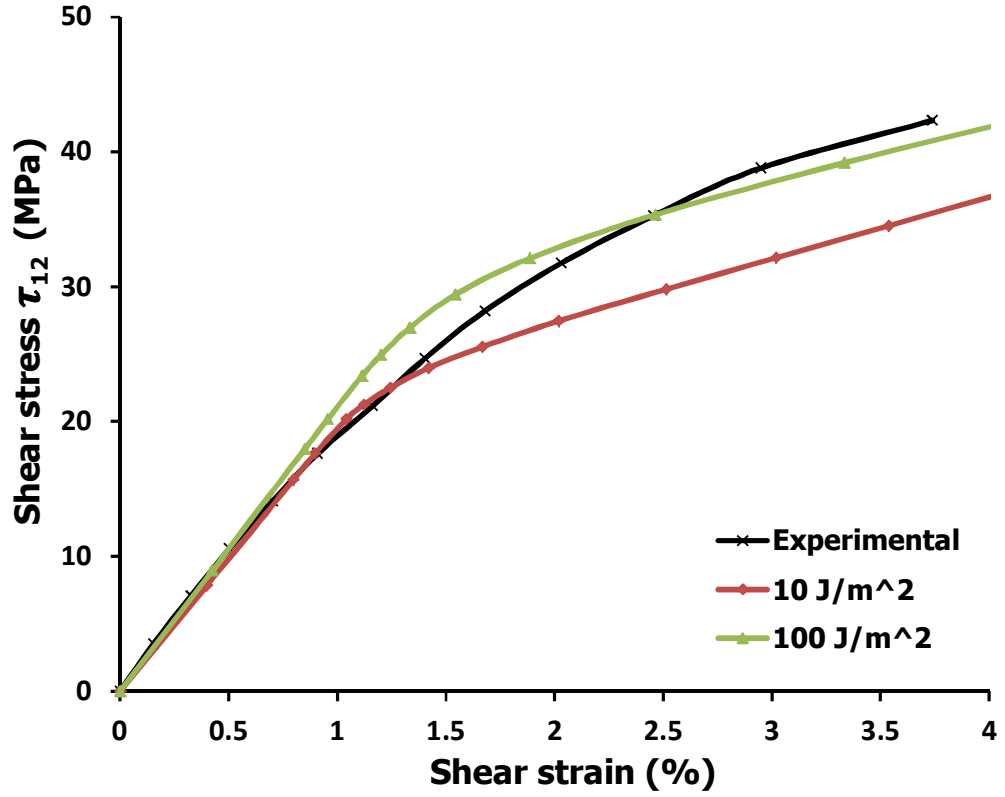


Figure 5.12 Effect of changing fracture energy of the fiber-matrix interface on shear stress-strain response

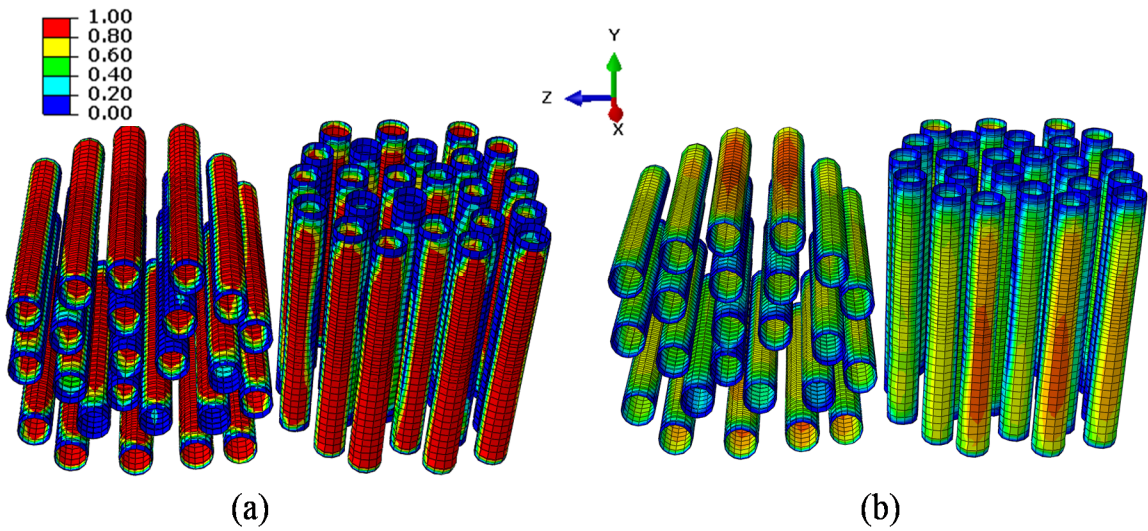


Figure 5.13 Contour plots of interfacial damage for fracture energies (a) 10 J/m² (b) 100 J/m² at 8% strain

5.6.2 Effect of matrix friction angle

Other than the interface fracture energy, it is expected that the matrix properties may also affect the response of the microdomain. The globleshear stress-strain responses of the micro-domain predicted by this micro-macro scheme are shown in Fig. 5.14. The interface properties are kept fixed interface stiffness as 10 GPa/mm, interface strength as 30 MPa and interfacial energy as 100 J/m². The matrix friction angles have been changed from 5° to 15°, which are commonly reported values of friction angle for the epoxy matrix (Gonzalez and Llorca, 2007). Since the matrix tensile strength was assumed to be constant and equal to 75 MPa, changes in the friction angles modifies the cohesive strength 'c' of the matrix as given in Eq. (3.9). The cohesive strength of the matrix increases from 37.5 MPa ($\varphi=0^\circ$) up to 48.8 MPa ($\varphi=15^\circ$). It can be seen from Fig. 5.14 that the onset of non-linear behavior is affected by changing the friction angle in composites. A lower value of the friction angle leads to an earlier onset of matrix yielding because the cohesive strength reduces when the friction angle is decreased and, therefore, the resistance to shear deformation decreases.

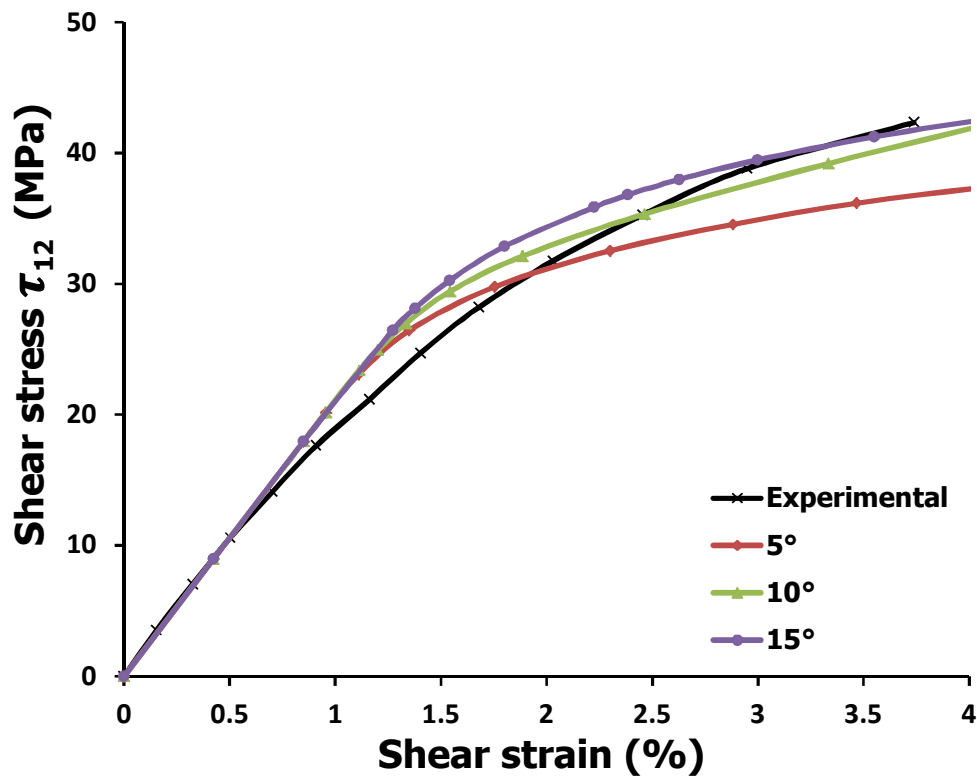


Figure 5.14 Effect of changing matrix friction angle on shear stress-strain response

5.7 Application of micro-macro analysis for characterization of stress raisers

The first step in performing the micro-macro analysis of any structure is to identify the regions of interest based on the stress distribution in a continuum model of the structure. Fig. 5.15 shows the von-Mises stress distribution in a double V-notch cross-ply laminate under shear loading. The stress concentration region can be seen near the notches. Fig. 5.15 also shows the location of the two microscale domains selected on the basis of the stress distribution. One microscale domain is placed below the notch at the top and the second one is placed away from the notch so that there is no stress concentration near the second microscale domain. The idea behind placing two microscale domains is that the results from both cases will clearly elucidate the differences in the damage initiation and propagation due to a stress raiser.

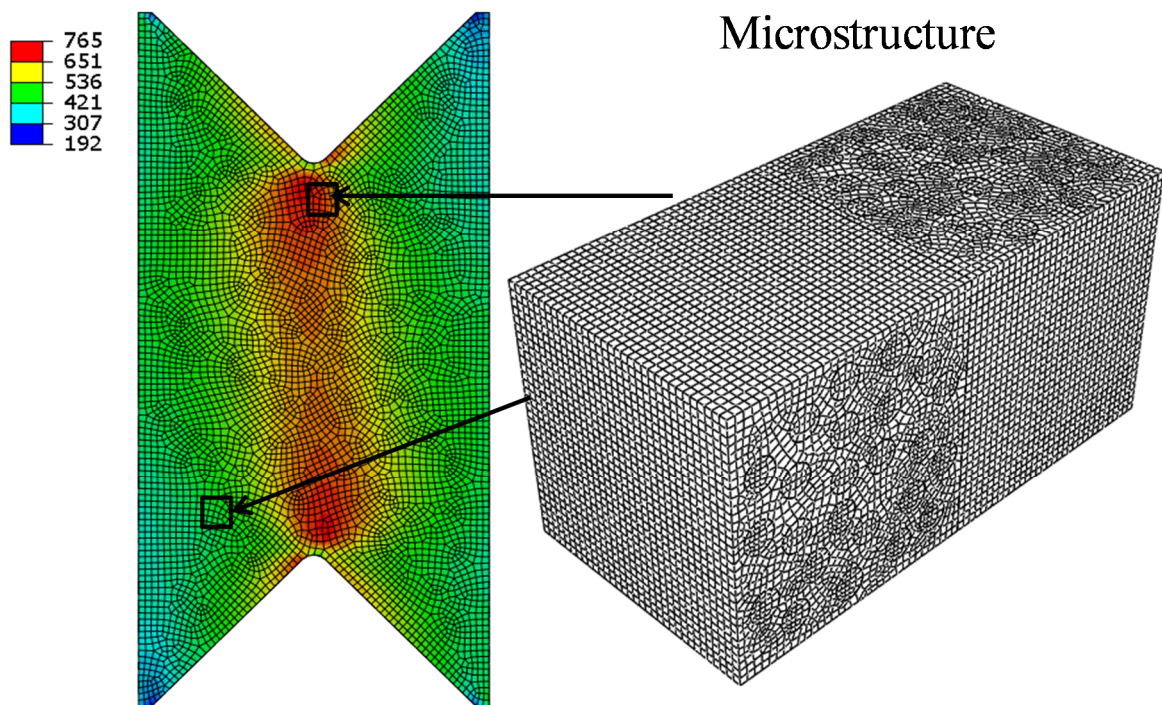


Figure 5.15 Von-Mises stress (MPa) distribution in a continuum model showing the regions of interest, i.e., regions near and away from the notch

The effect of the stress-raiser in the micro-domain is fairly pronounced if the shear stresses are plotted as a function of the applied shear load as shown in Fig. 5.16. It can be seen that if the micro-domain lies in the stress raiser (near the notch root) the volume averaged shear stress developed is 37.5% higher than the average stresses developed in the region away from the stress

raiser under a 40 N shear load. The volume averaged stresses in the stress raiser increases multifold (~1.45 times the stresses developed in the region away from the stress raiser) if the applied shear load is increased to 90 N. Hence, it can be interpreted that the micro-macro approach is useful in characterizing damage initiation and propagation in the hot zones, such as notches, holes, free edges and geometric discontinuities.

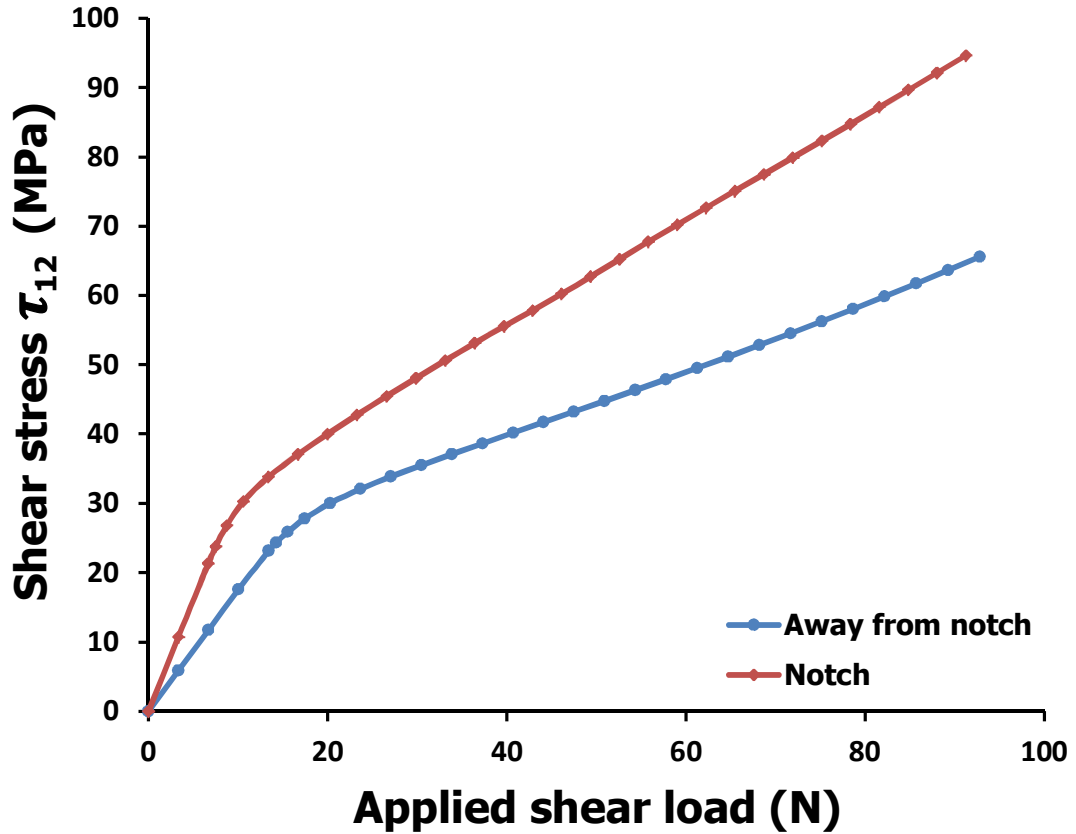


Figure 5.16 Volume averaged shear stress as a function of applied shear load

It is important to note here that the difference between stresses at two hotspots, i.e., one close to the notch and another away from the notch, can be quantified through macro model analysis. However, to quantify the damage initiation and evolution in terms of accumulated matrix damage accumulated and fiber-matrix debonding the analysis of micro-domain is essential. These microscopic damage mechanisms distinctly elucidate the differences in the behavior of regions close to stress singularities with those away from such singularities. It may be noted that this knowledge can be used for enhanced design/reinforcement at the hot spots.

5.7.1 Evolution of stresses and strains in microdomain

It may be noted that the accumulated plastic strains and stresses in the micro domains under the notch and away from it can potentially provide information about damage initiation and propagation as shown in Totry et al. (2009). As seen previously in Fig. 5.16, at a given shear load, the microdomain near the notch has higher volume averaged shear stresses as compared to the microdomain away from it. Consequently, it is expected that the stress evolution in the microdomains in the stress raiser and away from it will be different. To characterize the stresses in the two microdomains, the contour plots of von-Mises stress at a 90 N shear load are shown in Fig. 5.17. The maximum von-Mises stress in the region near the notch root is 82% higher than the maximum von-Mises stress induced in the region away from the notch root. This clearly shows that the effect of stress raisers on the micro-stresses can be characterized effectively via the micro-macro approach.

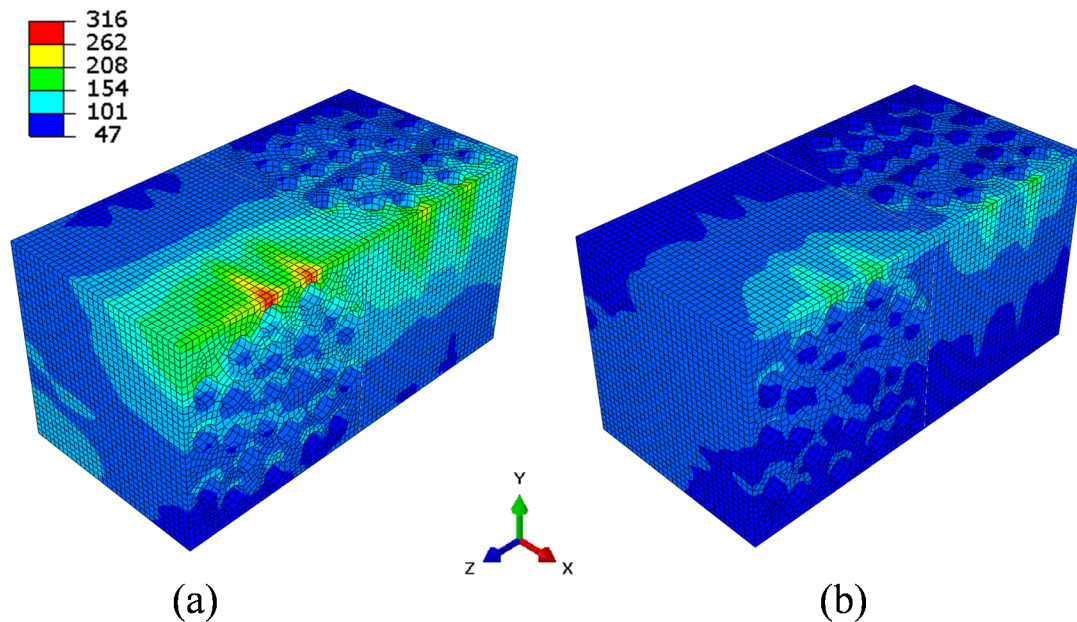


Figure 5.17 Contour plot of Von Mises stress (MPa) in the matrix of cross-ply laminate at (a) notch (b) away from the notch at a 90 N load

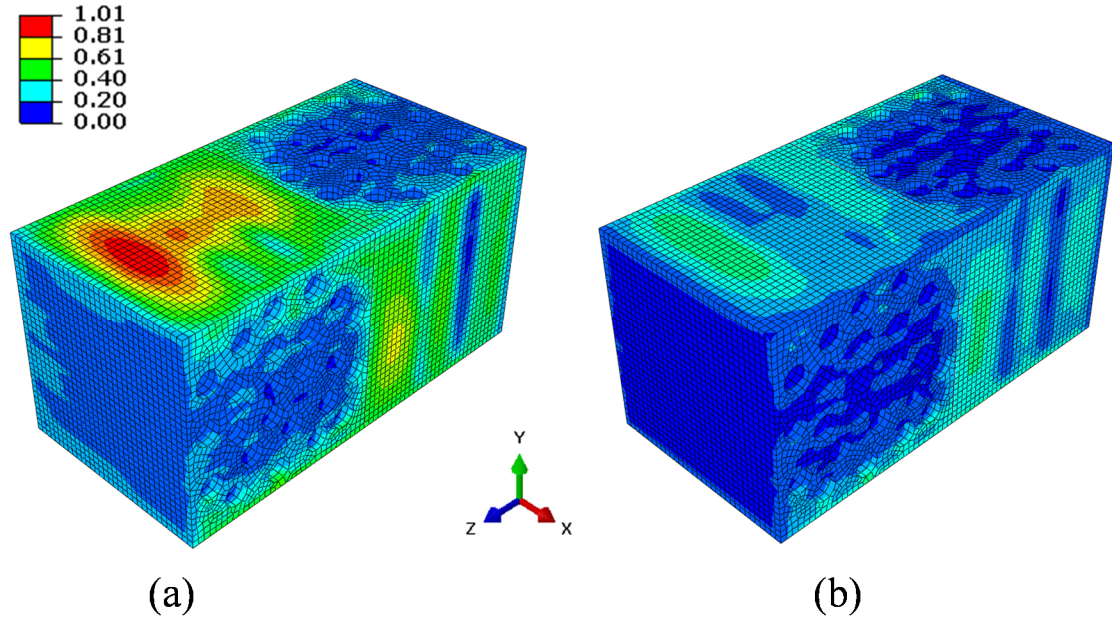


Figure 5.18 Contour plot of accumulated plastic strain in the matrix of cross-ply laminate at (a) notch (b) away from the notch at a 90 N load

Fig. 5.18 shows the accumulated plastic strain in the matrix. It can be seen that the plastic strain accumulates in the form of shear bands in the matrix and is not uniformly distributed in the matrix. These shear bands run parallel to the fibers and interact with each other, which leads to deformation in the matrix. It is seen that significantly high plastic strains are induced at the same load in the stress raiser and the maximum accumulated plastic strain in the stress raiser is 160% higher than the maximum accumulated plastic strain induced in the microdomain of the region away from the notch. Note that stresses and strains at the boundaries of the micro-domain may be problematic, however as mentioned in Section 2, that homogenization of the structure does not influence the homogenized part farther than the characteristic length of the structure. The stresses and strains predictions away from the boundary are relatively accurate.

5.7.2 Damage evolution at the microdomain

Besides evaluating the stresses and strains, the micro-macro method can also be used for characterizing the damage evolution in the matrix. Fig. 5.19 shows the evolution of the damage in the matrix as a function of the shear load for both the microdomains (in the vicinity of the notch root and away from it). It is observed that the damage in the matrix is higher at the notch as compared to away from the notch at every instance. This is expected because when the von-Mises contour plots of Fig. 5.18 show that at any location, the magnitude of stresses at the notch

are higher; this typically gives rise to larger plastic deformation of the matrix. Damage in matrix material at notch is ~10% higher as compared to damage in matrix for away from the notch at a 90N load.

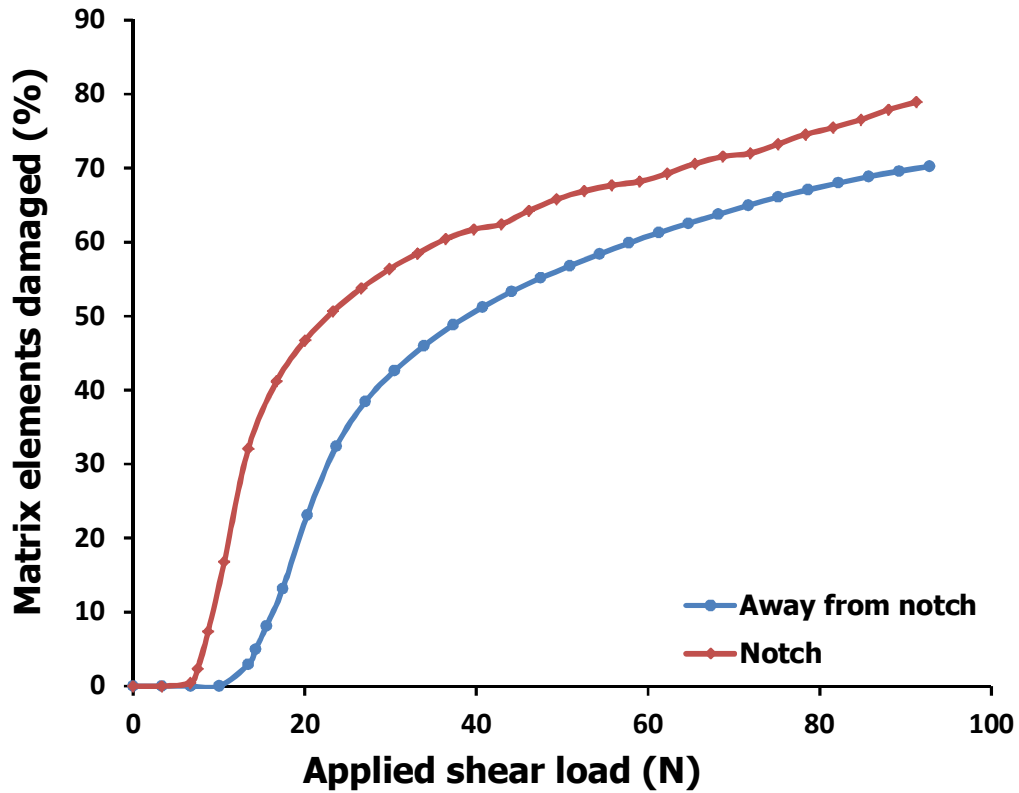


Figure 5.19 Comparison of evolution of the percentage of matrix elements damaged in the microstructure between the notch and away from it

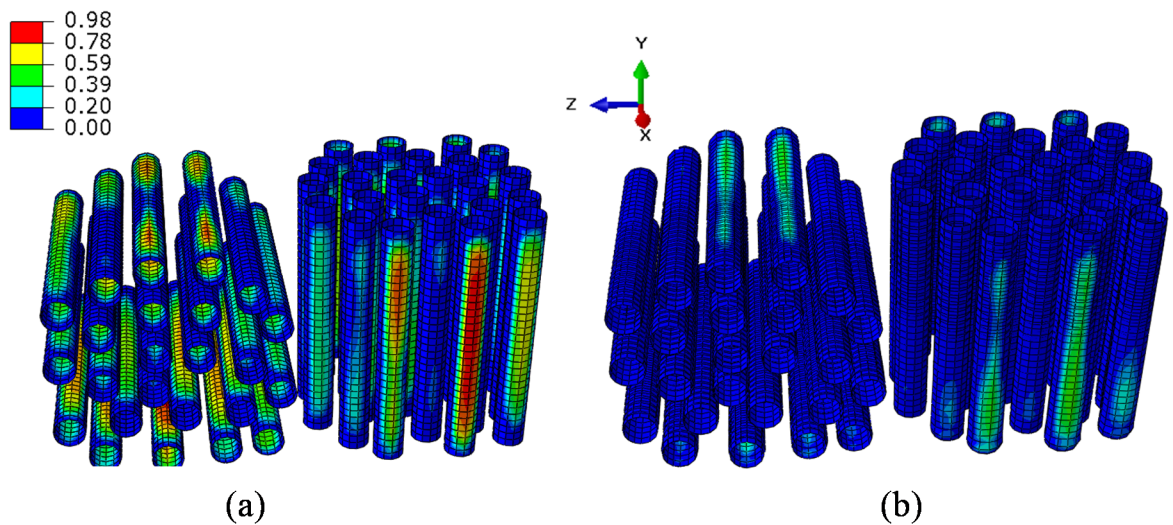


Figure 5.20 Contour plot of damage of the fiber-matrix interface (a) notch (b) away from the notch at a 90 N load (the value 1 indicates total failure of the interface).

The damage at the fiber-matrix interface is plotted in Fig. 5.20. It can be observed that the interface damage is more pronounced in the microdomain at the notch root as compared to the microdomain away from the notch. The maximum damage value increases by 75% due to the presence of a stress raiser. It can also be observed that the fiber-matrix decohesion progresses from the center to the edges of the fibers in both the cases.

5.8 Summary

A robust micro-macro multiscale scheme has been proposed in this work which can be applied to predict local response and microscale damage in laminates. This work investigated the effect of the stress-raiser and the local response in the microdomain near notch root of a rail shear specimen fabricated according to ASTM Standard D7078. The response of the microdomain in near the notch root has been compared with the local response of the microdomain away from the notch root and significant differences in stress/damage evolution have been found. The predicted material response with proposed micro-macro scheme is in good agreement with the experimental response and other established multiscale techniques, such as sub-modeling. The volume averaged stress value in the stress raiser is ~ 1.45 times the average stress developed in the region away from the stress raiser if the applied shear load is increased to 90 N. Damage in matrix material at notch is $\sim 10\%$ higher as compared to damage in matrix far away from the notch at a 90N load. It has also been observed that maximum interfacial damage is 75% higher in the region near the notch as compared to the region away from the notch. These results indicate that micro-macro method can be effectively used to characterize damage evolution in stress-raisers.

Chapter 6: Conclusions and future scope

6.1 Key conclusions

A new finite element based multi-fiber multi-layer representative volume element for the prediction of damage response of the laminate has been proposed. The material response obtained from the numerical simulations is found to be in good agreement with the experimental study performed. Parametric study has been performed using proposed M^2RVE to study effect of constituent's properties on the global material response. It may be noted that periodic boundary is not suitable assumption in the areas of stress concentration and geometric discontinuities. Therefore proposed M^2RVE model is not suitable for predicting local material response in non-periodic media. Therefore, a new approach call as micro-macro approach has been proposed. A detailed study has been performed using this approach and results are presented. Key conclusions from each chapter of this thesis are presented in the following section.

6.1.1 Damage analysis in in-plane shear via multi-fiber multi-layer representative volume element (M^2RVE)

A detailed micromechanics based multi-fiber multi-level representative volume element (M^2RVE) has been developed and implemented via FE analysis. The material response using proposed M^2RVE model has been validated against the experimental response. M^2RVE has been used for predicting matrix damage and fiber/matrix debonding. The following specific conclusions can be drawn from the study:

- There is a significant effect of matrix and fiber-matrix interfacial damage on the global as well as local material response.
- M^2RVE effectively captures the effect of intra/inter ply interactions (presence of multiple fibers and plies) on stress evolution in composite laminate.
- The evolution of interface damage is a function of stacking sequence which can be captured by M^2RVE .
- The proposed M^2RVE approach can potentially capture the effects of variations in the material properties which can be useful for design purposes.

6.1.2 Comprehensive damage analysis for complex multi-axial loading via M²RVE

A detailed micromechanics based multi-fiber multi-level representative volume element (M²RVE) has been implemented via FE analysis to study effect of all the failure mechanisms on the global as well as local damage response. M²RVE has been used for predicting fiber damage, matrix damage and fiber/matrix debonding and delamination between plies. The material response using proposed M²RVE model has been validated against the experimental response. Following points can be concluded:

- Fiber failure dominates all other failure mechanisms when fibers have been subjected to tensile stress in a particular loading.
- Whenever required depending on the type of loading, it is important to model delamination layer failure.
- When all the failure mechanisms such as fiber failure, matrix damage, interface damage and delamination layer damage are active, fiber failure takes place at almost ~60% lower stress and strain value as compared to the pure fiber failure mode. In the presence of out-of-plane shear loading, the fiber failure strength reduces significantly.
- When all the failure mechanisms are active simultaneously, failure strength as well as failure strain are different than when the single or/and two failure mechanisms are active. The proposed M²RVE can be used to accurately capture all the failure mechanisms active during complex multi-axial loading.

6.1.3 Micro-macro approach for damage prediction in non-periodic structures

A robust micro-macro multiscale scheme has been proposed in this work which can be applied to predict local response and microscale damage in laminates under multi-axial loading. This work investigated the effect of the stress-raiser and the local response in the microdomain near notch root of a rail shear specimen used in ASTM Standard D7078. The response has been compared with the local response of the microdomain away from the notch root and significant differences in stress evolution and damage behavior have been found. The key findings can be summarized as follows:

- The predicted response with proposed micro-macro scheme is in good agreement with the experimental response and other established multiscale techniques, such as sub-modeling.
- A lower value of the matrix friction angle leads to an earlier onset of matrix yielding causing significant reduction in stiffness of the material.
- There is a significant difference between stresses and accumulated plastic strains developed in the micro-domain near the notch root as compared average stress developed in the micro-domain away from the notch.
- Micro-macro approach is useful in characterizing damage initiation and propagation in the hot-zones such as notches, free edges etc.

6.2 Contributions

The major contributions of this work are as follows:

- Development and implementation of multi-fiber multi-layer representative volume element for the analysis of multi-layer symmetric laminate.
- Characterization of all the possible microscale damage mechanisms in composites.
- Implementation of different failure theories to capture failure of each constituent.
- Development and implementation of micro-macro method to predict microscale damage response in real structures.

6.3 Future scope

The following task can be investigated for the further research:

- Development and implementation of boundary conditions which can be applied to M^2RVE for modeling symmetrical as well as non-symmetrical stacking sequence of composite laminate.
- Development and implementation of damage mechanism for macroscale lamina in micro-macro method.
- Study of complex multi-axial loading in real structures via micro-macro method.

Appendix-I

In-plane shear stress-strain data for [0/90] laminate

Stress (MPa)	Strain (%)
0	0
3.527337	0.1536
7.054674	0.3265
10.58201	0.5027
14.10935	0.7029
17.63668	0.9097
21.16402	1.1622
24.69136	1.404
28.21869	1.6798
31.74603	2.0306
35.27337	2.4554
38.80071	2.9497
42.32804	3.7377

In-plane shear stress-strain data for [± 45] laminate

Stress (MPa)	Strain (%)
0	0
3.289474	0.0816
6.578947	0.1489
9.868421	0.2172
13.15789	0.2709
16.44737	0.3352
19.73684	0.4125
23.02632	0.4697
26.31579	0.5346
29.60526	0.6086
32.89474	0.6784
36.18421	0.7457
39.47368	0.8381
42.76316	0.9051
46.05263	0.9602
49.34211	1.0431
52.63158	1.1117
55.92105	1.1618
59.21053	1.2551
62.5	1.3449

65.78947	1.4004
69.07895	1.4676
72.36842	1.5383
75.65789	1.6073
78.94737	1.7116
82.23684	1.7932
85.52632	1.8824
88.81579	2.0295
92.10526	2.1718

Appendix-II

Fiber failure data with probability of fiber failure using ranking method

Sample no. (i)	Stress at fiber failure (MPa)	Probability of fiber failure $P = \frac{i-0.5}{n}$ (n is total no. of samples)
1	1157	0.02
2	1202	0.06
3	1245	0.1
4	1287	0.14
5	1289	0.18
6	1304	0.22
7	1334	0.26
8	1373	0.3
9	1379	0.34
10	1485	0.38
11	1485	0.42
12	1506	0.46
13	1669	0.5
14	1705	0.54
15	1748	0.58

16	1750	0.62
17	1768	0.66
18	1792	0.7
19	1859	0.74
20	1901	0.78
21	1906	0.82
22	2006	0.86
23	2061	0.9
24	2097	0.94
25	2093	0.98

Appendix-III

User subroutine used for fiber failure

SUBROUTINE

```
    USDFLD (FIELD, STATEV, PNEWDT, DIRECT, T, CELENT, TIME, DTIME,  
1  CMNAME, ORNAME, NFIELD, NSTATV, NOEL, NPT, LAYER, KSPT, KSTEP, KINC,  
2  NDI, nshr, coord, jmac, jmtyp, matlayo, laccflg)  
C  
INCLUDE 'ABA_PARAM.INC'  
C  
C  
CHARACTER*80 CMNAME, ORNAME  
CHARACTER*3  FLGRAY (15)  
DIMENSION FIELD (NFIELD), STATEV (NSTATV), DIRECT (3, 3), T (3, 3), TIME (2),  
*  coord (*), jmac (*), jmtyp (*)  
DIMENSION ARRAY (15), JARRAY (15)  
  
COMMON /KBLK1/ MYSTATE  
SAVE /KBLK1/  
REAL MYSTATE  
C  
    CALL GETVRM ('SP', ARRAY, JARRAY, FLGRAY, jrzd,  
$  jmac, jmtyp, matlayo, laccflg)  
C  
    S1=ABS (ARRAY (1))  
    S2=ABS (ARRAY (2))  
    S3=ABS (ARRAY (3))  
C  
IF (S1.GE.1630.0D0.OR.S2.GE.1630.0D0.OR.S3.GE.1630.0D0) THEN  
    MYSTATE= 1.0D0  
ENDIF  
FIELD (1)=MYSTATE  
RETURN  
END
```

References

1. Abaqus Inc., Pawtucket, RI. Abaqus Analysis User's manual, 2010, Version 6.9.
2. Abolfathi, N., Naik, A., Karami, G., Ulven, C., 2008. A micromechanical characterization of angular bidirectional fibrous composites. *Comput. Mater. Sci.* 43, 1193–1206.
3. Azzi, V.D., Tsai, S.W., 1965. Anisotropic strength of composites. *Exp. Mech.* 5(9), 283-288.
4. Borokov, A.I., Sabadash, V.O., 2002. Finite Element Multiscale Homogenization and Sequential Heterogenization of Composite Structures. Proc. 10th Int. 'ANSYS' Conference.
5. Asp, L., Berglund, L., Talreja, R., 1996. Effects of fiber and inter-phase on matrix-initiated transverse failure in polymer composites. *Compos. Sci. Technol.* 56(6), 657-665.
6. ASTM Standard C1239-13, 2013. Standard practice for reporting uniaxial strength data and estimating Weibull distribution parameters for advanced ceramic. ASTM, Philadelphia, PA, USA.
7. ASTM Standard D2584–11, 2000. Standard Test Method for Ignition Loss of Cured Reinforced Resins. ASTM International, West Conshohocken, PA, USA.
8. ASTM Standard D7078/D7078M–05, 2000. Standard Test Method for Shear Properties of Composite Materials by V-Notched Rail Shear Method. ASTM International, West Conshohocken, PA, USA.
9. Benzeggagh, M., Kenane, M., 1996. Measurement of mixed-mode delamination fracture toughness of unidirectional class/epoxy composites with mixed-mode bending apparatus. *Compos. Sci. Technol.* 56, 439-449.
10. Bergman, B., 1984. On the estimation of the Weibull modulus. *J Mater SciLett.* 3, 689-692.
11. Berger, H., Kari, S., Gabbert, U., Rodriguez-Ramos, R., Bravo-Castillero, J., Guinovart - Diaz, R., 2005. A comprehensive numerical homogenization technique for calculating effective coefficients of uniaxial piezoelectric fiber composites. *Mater. Sci. Eng. A* 412, 53–60.

12. Bohm, H.J., Han, W., Eckschlager, A., 2004. Multi-inclusion unit cell studies of reinforcement stresses and particle failure in discontinuously reinforced ductile matrix composites. *Comput Model Eng Sci.* 5, 5–20.
13. Borbely, A., Kenesei, P., Biermann, H., 2006. Estimation of the effective properties of particle-reinforced metal matrix composites from microtomographic reconstructions. *Acta Mater.* 54, 2735–2744.
14. Camanho, P.P., Davila, C.G., Pinho, S.T., Iannucci, L., Robinson, P., 2006. Prediction of in situ strengths and matrix cracking in composites under transverse tension and in-plane shear. *Composites Part A* 37, 165–176.
15. Canal, L., Segurado, J., LLorca, J., 2009. Failure surface of epoxy-modified fiber-reinforced composites under transverse tension and out-of-plane shear. *Int. J. Solids Struct.* 46, 2265–2274.
16. Cantwell, W., Morton, J., 1991. The impact resistance of composite materials—a review. *Composites.* 22(5), 347–362.
17. Chawla, N., Sidhu, R.S., Ganesh, V.V., 2006. Three-dimensional visualization and microstructure-based modeling of deformation in particle-reinforced composites. *Acta Mater.* 54, 1541–1548.
18. Crossman, F., Warren, W., Wang, A., Law, G., 1980. Initiation and growth of transverse cracks and edge delamination in composite laminates part 2. Experimental correlation. *J Compos Mater Suppl.* 14, 88–108.
19. Davila, C., Camanho, P.P., Rose, C.A., 2005. Failure criteria for FRP laminates. *J Compos Mater.* 39, 323–345.
20. Donadon, M.V., Falzon, B.G., Iannucci, L., Hodgkinson, J.M., 2007. A 3-D micromechanical model for predicting the elastic behaviour of woven laminates. *Compos. Sci. Technol.* 67, 2467–2477.
21. Digimat Inc., Digimat Users' manual, 2011, version 4.2.1.
22. Ellyin, F., Xia, Z., Chen, Y., 2003. Viscoelastic micromechanical modeling of free edge and time effects in glass fiber/epoxy cross-ply laminates. *Composites Part A.* 33, 399–409.

23. Feih, A., Tharaner, H., Lilholt, J., 2005. Tensile strength and fracture surface characterization of sized and unsized glass fibers. *Mater. Sci.* 40,1615-1623.
24. Feyel, F., and Chaboche, J., 2000. FE^2 multiscale approach for modelling the elasto-viscoplastic behavior of long fiber SiC/Ti composite materials. *Comput. Meth. Appl. Mech. Eng.* 183, 309–330.
25. Feyel, F., Chaboche, J., 2003. A multilevel finite element method (FE^2) to describe the response of highly non-linear structures using generalized continua. *Comput. Meth. Appl. Mech. Eng.* 192, 3233–3244.
26. Fish, J., Belsky, V., 1995. Multigrid method for periodic heterogeneous media, part II: multiscale modeling and quality control in multidimensional case, *Comp. Meth. in Appl. Mech. and Eng.* 126, 17-38.
27. Geers, M.G.D., Kouznetsova, V.G., Brekelmans, W.A.M., 2010. Multiscale computational homogenization: Trends and challenges. *J. Comput. Appl. Math.* 234, 2175–2182.
28. Ghosh, S., Lee, K., Moorthy, S., 1995. Multiple scale analysis of heterogeneous elastic structures using homogenisation theory and Voronoi cell finite element method. *Int. J. Solids Struct.* 32(1), 27–62.
29. Ghosh, S., Lee, K., and Moorthy, S., 1996. Two scale analysis of heterogeneous elasticplastic materials with asymptotic homogenisation and Voronoi cell finite element model. *Comput. Meth. Appl. Mech. Eng.* 132, 63–116.
30. Ghosh, S., Lee, K., Raghvan, P., 2001. A multi-level computational model for multiscale damage analysis in composite and porous material. *Int. j. Solids Struct.* 38, 2335–2385.
31. Gibson, R.F., 2007. Principles of composite material mechanics. CRC Press.
32. Gonzalez, C., Segurado, J., LLorca, J., 2004. Numerical simulation of elastoplastic deformation of composites: evolution of stress microfields and implications for homogenization models. *J MechPhys Solids.* 52,1573–1593.
33. González, C., Llorca, J., 2006. Multiscale modeling of fracture in fiber-reinforced composites. *Acta. Mater.* 54(16), 4171-4181.

34. González, C., LLorca, J., 2007. Mechanical behavior of unidirectional fiber-reinforced polymers under transverse compression: Microscopic mechanisms and modeling. *Compos. Sci. Technol.* 67, 2795–2806.
35. Griffiths, R., Holloway, D.G., 1970. The fracture energy of some epoxy resin materials. *J. mater. sci.* 5, 302-307.
36. Hashin, Z., 1980. Failure Criteria for Unidirectional Fiber Composites. *J. Appl. Mech.* 47, 329-334.
37. Hao, W., Melkote, S., Danyluk, S., 2012. Mechanical Strength of Silicon Wafers Cut by Loose Abrasive Slurry and Fixed Abrasive Diamond Wire Sawing. *Adv. Eng. Mater.* 14, 342-348.
38. Hill, R., 1963. Elastic properties of reinforced solids: some theoretical principles. *Journal of mech. Phys. Solids.* 11, 357– 372.
39. Ivanov, D.S., Lomov, S.V., Ivanov, S.G., Verpoest, I., 2010. Stress distribution in outer and inner plies of textile laminates and novel boundary conditions for unit cell analysis. *Composites Part A.* 41, 571–580.
40. Jia, X., Xia, Z., Gu, B., 2012. Micro/meso-scale damage analysis of three-dimensional orthogonal woven composites based on sub-repeating unit cells. *J. Strain Anal. Eng. Des.* 47(5), 313-328.
41. Jiang, H., Xie, Y., 2011. A note on the Mohr-Coulomb and Drucker- Prager strength criteria. *Mech. Res. Commun.* 38, 309–314.
42. Jones R., 1999. *Mechanics of composite materials.* Taylor and Francis.
43. Kanoute, P., Boso, D.P., Chaboche, J.L., Schrefler, B.A., 2009. Multiscale methods for composites: A review. *Arch. Comput. Meth. Eng.* 16, 31–75.
44. Kassem, G.A., 2009. Micromechanical material models for polymer composites through advanced numerical simulation techniques. Ph.D. thesis. RWTH Aachen University Germany.
45. Kenane, M., Benzeggagh, M., 1997. Mixed-mode delamination fracture toughness of unidirectional glass/epoxy composites under fatigue loading. *Compos. Sci. Technol.* 57,597-605.

46. Kerans, R.J., 1991. Theoretical analysis of the fiber pullout and pushout tests. *Journal of American Ceramic Society* 74(7), 1585–1596.
47. Kouznetsova, V., Brekelmans, W., Baaijens, F., 2001. An approach to micro-macro modeling of heterogeneous materials. *Comput. Mech.* 27, 37–48.
48. LLorca, J., Segurado, J., 2004. Three-dimensional multiparticle cell simulations of deformation and damage in sphere-reinforced composites. *Mater SciEng A.* 365, 267–274.
49. Lusti, H.R., Hine, P.J., Gusev, A.A., 2002. Direct numerical predictions for the elastic and thermoelastic properties of short fibre composites. *Compos Sci Technol.* 62,1927–34.
50. Mahesh, S., Beyerlein, I., Phoenix, S., 1999. Size and heterogeneity effects on the strength of fibrous composites. *Physica D.* 133(1–4), 371–389.
51. Mahmoodia, M.J., Aghdamb, M.M., 2011. Damage analysis of fiber reinforced Ti-alloy subjected to multi-axial loading—A micromechanical approach. *Mater. Sci. Eng. A* 528, 7983– 7990.
52. Markovic, D., Ibrahimbegovic, A., 2004. On micro-macro conditions for micro scale based FEM for inelastic behavior of heterogeneous materials. *Comput. meth. Appl. Mech. Eng.* 193, 5503-5523.
53. Matsuda, T., Okumura, D., Ohno, N., Kawai, M., 2007. Three-dimensional microscopic interlaminar analysis of cross-ply laminates based on a homogenization theory. *Int. J. Solids Struct.* 44, 8274–8284.
54. Michel, J.C., Moulinec, H., Suquet, P., 1999. Effective properties of composite materials with periodic microstructure: a computational approach. *Comput Meth ApplMech Eng.* 172,109–43.
55. Ng, W.H., Salvi, A.G., Waas, A.M., 2010. Characterization of the in-situ non-linear shear response of laminated fiber- reinforced composites. *Compos. Sci. Technol.* 70, 1126–1134.
56. Oden, J.T., Zohdi, T.I., 1997. Analysis and adaptive modeling of highly heterogeneous elastic structures. *Comput. Meth. Appl. Mech. Eng.* 148, 367-391.
57. Pagano, N.J., Rybicki, E.F., 1974. On the significance of effective modulus solutions for fibrous composites. *J. Comp. Mat.* 8, 214-228.
58. Puck, A., Schürmann, H., 1998. Failure analysis of FRP laminates by means of physically based phenomenological models. *Compos. Sci. Technol.* 58, 1045–1067.

59. Puck, A., Schurmann, H. 2002. Failure analysis of FRP laminates by means of physically based phenomenological models. *Composites Sci Technol.* 62,1633–1662.
60. Riks, E., 1979. An incremental approach to the solution of snapping and buckling problems. *Int. J. Solids Struct.* 15, 529-551.
61. Segurado, J., LLorca, J., 2002. A numerical approximation to the elastic properties of sphere-reinforced composites. *J MechPhys Solids.* 50, 2107–2121.
62. Segurado, J., Gonzalez, C., LLorca, J., 2003. A numerical investigation of the effect of particle clustering on the mechanical properties of composites. *Acta Mater.* 51,2355–2369.
63. Segurado, J., LLorca, J., 2006. Computational micromechanics of composites: the effect of particle spatial distribution. *Mech Mater.* 38,873–883.
64. Sela, N., Ishai, O., 1989. Interlaminar fracture toughness and toughening of laminated composite materials-a review. *Composites.* 20 (5), 423-435.
65. Shao, J., Wang, F., Li, L., Zhang, J., 2013. Scaling Analysis of the Tensile Strength of Bamboo Fibers Using Weibull Statistics. *Adv Mater Sci Eng.* Article ID 167823.
66. Sherwood, J.A., Quimby, H.M., 1995. Micromechanical modeling of damage growth in titanium based metal-matrix composites. *Comput. Struct.* 56, 505– 514.
67. Shokrieh, M., Heidari-Rarani M., 2011. Effect of stacking sequence on R-curve behavior of glass/epoxy DCB laminates with $0^\circ // 0^\circ$ crack interface. *Mat. Sci. Eng. A.* 529, 265-269.
68. Shoukry, S.N., Prucz, J.C., Eluripati, R., Shankaranarayana, P.G., William, G.W., 2007. Multi-Fiber Unit Cell for Prediction of Residual Stresses in Continuous Fiber Composites. *Mech. Adv. Mater. Struct.* 14, 531–540.
69. Smit, R., Brekelmans, W., Meijer, H., 1998. Prediction of the mechanical behavior of non-linear heterogeneous systems by multi-level finite element modeling. *Comput. Meth. Appl. Mech. Eng.* 155, 181–192.
70. Sun, C.T., Vaidya, R.S., 1996. Prediction of composite properties from a representative volume element. *Compos. Sci. Technol.* 56, 171–179.
71. Sun, C., Wang, Y., 2001. Determine the size of “local domain” in multiscale analysis. *Proceedings of the 13th International Conference of Composite Materials.* Paper Number: 1681.

72. Taliercio, A., Coruzzi, R., 1999. Mechanical behaviour of brittle matrix composites: a homogenization approach. *Int. J. Solids Struct.* 36, 3591–3615.
73. Teradaa, K., Horib, M., Kyoyac, T., Kikuchi, N., 2000. Simulation of the multiscale convergence in computational homogenization approaches. *Int. J. Solids Struct.* 37, 2285–2311.
74. Totry, E., González, C., LLorca, J., 2008. Prediction of the failure locus of C/PEEK composites under transverse compression and longitudinal shear through computational micromechanics. *Compos. Sci. Technol.* 68, 3128–3136.
75. Totry, E., González, C., LLorca, J., 2009. Molina-Aldareguía J. Mechanisms of shear deformation in fiber-reinforced polymers: experiments and simulations. *Int. J. Fracture* 158, 197–209.
76. Totry, E., Molina-Aldareguia, J.M., González, C., LLorca, J., 2010. Effect of fiber, matrix and interface properties on the in-plane shear deformation of carbon-fiber reinforced composites. *Compos. Sci. Technol.* 70,970–980.
77. Tyrus, J.M., Gosz, M., DeSantiago, E., 2007. A local finite element implementation for imposing periodic boundary conditions on composite micromechanical models. *Int. J. Solids Struct.* 44, 2972–2989.
78. Vogler, T.J., Kyriakides, S. 1999. Inelastic behavior of an AS4/PEEK composite under combined transverse compression and shear. Part I: Experiments. *Int J Plasticity.* 15, 783–806.
79. Wang, A.S.D., Yan, K.C., 2005. On modeling matrix failures in composites. *Composites: Part A*, 36, 1335-1346.
80. Wang, H., Qin, Q., Ji, H., Sun, Y., 2011. Comparison among different modeling techniques of 3D micromechanical modeling of damage in unidirectional composites. *Adv. Sci.lett.* 4, 400-407.
81. Weibull, W., 1951. A statistical distribution function of wide applicability. *J Appl Mech.* 293-297.

82. Xia, Z., Chen, Y., Ellyin, F., 2000. A meso/micro-mechanical model for damage progression in glass-fiber/epoxy cross-ply laminates by finite-element analysis. *Compos. Sci. Technol.* 60, 1171–1179.
83. Xia, Z., Zhang, Y., Ellyin, F., 2003. A unified periodical boundary conditions for representative volume elements of composites and applications. *Int. J. Solids Struct.* 40, 1907–1921.
84. Xia, Z., Zhou, C., Yong, Q., Wang, X., 2006. On selection of repeated unit cell model and application of unified periodic boundary conditions in micro-mechanical analysis of composites. *Int. J. Solids Struct.* 43, 266–278.
85. Youssef, S., Maire, E., Gaertner, R., 2005. Finite element modelling of the actual structure of cellular materials determined by X-ray tomography. *Acta Mater.* 53, 719–730.
86. Zhang, Y., Xia, Z., Ellyin, F., 2005. Viscoelastic and damage analysis of fibrous polymer laminates by micro/meso mechanical modeling. *J. comp. mater.* 39, 2001–2022.
87. Zohdi, T., Wriggers, P., 1999. A domain decomposition method for bodies with heterogeneous microstructure based on material regularization, *Int. J. Solids Struct.* 36, 2507-2525.
88. Zhou, X.F., Wagner, H.D., Nutt, S.R., 2001. Interfacial properties of polymer composites measured by push-out and fragmentation tests. *Composites Part A.* 32, 1543–1551.

Publications

Journal publication

1. Soni, G., Singh, R., Mitra, M., Falzon, B.G., 2014. Modeling matrix damage and fibre-matrix interfacial decohesion in composite laminates via a multi-fibre multi-layer representative volume element (M^2RVE). International Journal of Solids and Structures 51, 449-461.
2. Soni G., Gupta S., Singh R., Mitra M., Yan W., Falzon B.G., 2014. Study of localized damage in composite laminates using micro-macro approach. Composite Structures, 113, 1-11.
3. Soni G., Singh R., Mitra M., Yan W., Falzon B.G., 2014. Modeling of microscale damage mechanisms via a multi-fiber multi-layer representative volume element (M^2RVE) (Submitted to Journal of Composites Science and Technology).

Conference proceedings

1. Soni, G., Singh, R., Mitra, M., Falzon .B.G. Multilayer multifiber representative volume element for prediction of matrix and interfacial damage in composite laminates. ECCM 15, Venice Italy, June, 24-28, 2012.
2. Gupta S., Soni G., Singh R. Micro-macro approach for predicting localized stress distribution in composites”, ICCM 19, Montreal Canada, July, 28- Aug 2, 2013.
3. Choksi P., Soni G., Singh R. FE- based modeling for prediction of in-plane shear and delamination in composite laminates. Proceedings of the 3rd Asian Conference of Mechanics of Functional Materials and Structures, paper no. 60040, New Delhi, 2012.
4. Gupta S., Soni G., Singh R. Micro-macro analysis of composite laminate damage prediction and propagation. Proceedings of the 3rd Asian Conference of Mechanics of Functional Materials and Structures, paper no. 60044, New Delhi, 2012.